IMPERIAL

Reconfigurable Intelligent Surfaces:
Beamforming, Modulation, and Channel Shaping

Yang Zhao

Supervisor: Prof. Bruno Clerckx

Department of Electrical and Electronic Engineering
Imperial College London

This dissertation is submitted for the degree of
Doctor of Philosophy

Declaration

I hereby declare that the contents presented in this dissertation are original and have been carried out by myself under the guidance of my supervisor Prof. Bruno Clerckx. Any work from other researchers, scholars, or sources have been properly cited and acknowledged. The contents have not been submitted in whole or in part for consideration of any other degree or qualification in any academic institution. I am aware of the ethical standards and academic integrity policies of Imperial College London, and I have adhered to these principles throughout the course of my study. In signing this declaration, I affirm my commitment to academic honesty, intellectual integrity, and the pursuit of knowledge in the service of truth and understanding.

The source code of all simulation results in this dissertation are publicly available at https://github.com/snowztail/.

Yang Zhao
March 2024

Abstract

This is where you write your abstract ...

Table of contents

List of figures

List of tables

Abbreviations

bpcu	bits per channel use
bps/Hz	bits per second per Hertz
AF	Amplify-and-Forward
AM	Arithmetic Mean
AmBC	Ambient Backscatter Communication
AO	Alternating Optimization
AP	Access Point
AWGN	Additive White Gaussian Noise
BackCom	Backscatter Communication
BBC	Bistatic Backscatter Communication
BCD	Block Coordinate Descent
BD	Beyond-Diagonal
BER	Bit Error Rate
BIBO	Binary-Input Binary-Output
BLS	Backtracking Line Search
CLT	Central Limit Theorem
CP	Canonical Polyadic
CR	Cognitive Radio
CSCG	Circularly Symmetric Complex Gaussian
CSI	Channel State Information
CSIT	Channel State Information at the Transmitter
CW	Continuous Waveform
DC	Direct Current
DCMC	Discrete-input Continuous-output Memoryless Channel

DF	Decode-and-Forward
DMC	Discrete Memoryless Channel
DMMAC	Discrete Memoryless Multiple Access Channel
DMTC	Discrete Memoryless Thresholding Channel
DoF	Degree of Freedom
DP	Dynamic Programming
EIRP	Effective Isotropic Radiated Power
FDMA	Frequency-Division Multiple Access
FPGA	Field-Programmable Gate Array
GM	Geomtric Mean
GP	Geometric Programming
i.i.d.	independent and identically distributed
IC	Interference Channel
IM	Index Modulation
IoE	Internet of Everything
IoT	Internet of Things
KKT	Karush-Kuhn-Tucker
LC	Low-Complexity
LoS	Line-of-Sight
M2M	Machine-to-Machine
MAC	Multiple Access Channel
MBC	Monostatic Backscatter Communication
MC	Multiplication Coding
MIMO	Multiple-Input Multiple-Output
MISO	Multiple-Input Single-Output
ML	Maximum-Likelihood
MMSE	Minimum Mean-Square-Error
MRC	Maximal Ratio Combining
MRT	Maximum Ratio Transmission

MSE	Mean-Square Error
NLoS	Non-Line-of-Sight
NOMA	Non-Orthogonal Multiple Access
OFDM	Orthogonal Frequency-Division Multiplexing
PC	Point-to-point Channel
PDF	Probability Density Function
PGA	Projected Gradient Ascent
PIN	Positive Intrinsic Negative
PS	Power Splitting
PSK	Phase Shift Keying
QAM	Quadrature Amplitude Modulation
QoS	Quality of Service
R-E	Rate-Energy
RCG	Riemannian Conjugate Gradient
RF	Radio-Frequency
RFID	Radio-Frequency Identification
RIS	Reconfigurable Intelligent Surface
SC	Superposition Coding
SCA	Successive Convex Approximation
SDMA	Space-Division Multiple Access
SDP	Semi-Definite Programming
SDR	Semi-Definite Relaxation
SIC	Successive Interference Cancellation
SIMO	Single-Input Multiple-Output
SINR	Signal-to-Interference-plus-Noise Ratio
SISO	Single-Input Single-Output
SMAWK	Shor-Moran-Aggarwal-Wilber-Klawe
SMF	Scaled Matched Filter
SNR	Signal-to-Noise Ratio
SR	Symbiotic Radio

| SVD | Singular Value Decomposition |
| SWIPT | Simultaneous Wireless Information and Power Transfer |

| TDMA | Time-Division Multiple Access |
| TS | Time Switching |

| UE | User Equipment |

WF	Water-Filling
WIT	Wireless Information Transfer
WPCN	Wireless Powered Communication Network
WPT	Wireless Power Transfer

| ZF | Zero-Forcing |

Notation

Constants

e	Euler's number $\simeq 2.71828\ldots$
$\jmath$	The imaginary unit $= \sqrt{-1}$
π	Archimedes' constant $\simeq 3.14159\ldots$

Objects

a, A	Scalar
$\mathbf{a}$	Column vector
$\mathbf{A}$	Matrix
$\mathcal{A}$	Finite set
$\mathbf{0}$	Zero matrix
$\mathbf{1}$	One matrix
$\mathbf{I}$	Identity matrix

Sets

$\mathbb{R}$	Real numbers
$\mathbb{R}_+$	Real nonnegative numbers
$\mathbb{C}$	Complex numbers
$\mathbb{I}$	Probability domain $[0, 1]$
$\mathbb{H}_+^{n \times n}$	Positive semi-definite matrices of dimension $n \times n$
$\mathbb{U}^{n \times n}$	Unitary matrices of dimension $n \times n$

Operations

$(\cdot)^*$	Complex conjugate
$(\cdot)^\mathsf{T}$	Transpose
$(\cdot)^\mathsf{H}$	Hermitian (conjugate transpose)
$(\cdot)^\dagger$	Moore-Penrose inverse

$(\cdot)^+$	Ramp function $\max(0, \cdot)$
$|\cdot|$	Absolute value of a complex number
$\|\cdot\|$	Euclidean norm of a vector
$\|\cdot\|_F$	Frobenius norm of a matrix
$\arg(\cdot)$	Argument of a complex number
$\text{card}(\cdot)$	Cardinality of a finite set
$\log(\cdot)$	Natural logarithm of a real number
$\exp(\cdot)$	Exponential of a scalar or square matrix
$\text{tr}(\cdot)$	Trace of a square matrix
$\det(\cdot)$	Determinant of a square matrix
$\text{sv}(\cdot)$	Singular values sorted from largest to smallest
$\text{diag}(\cdot)$	Constructs a square matrix with inputs on the main diagonal
$\text{diag}^{-1}(\cdot)$	Retrieves the main diagonal of a square matrix
$\Re(\cdot)$	Retrieves the real part of a complex number
$\Im(\cdot)$	Retrieves the imaginary part of a complex number
$\mathbb{E}(\cdot)$	Expectation operator
$\mathbb{A}(\cdot)$	Extracts the Direct Current component of a signal
$\odot$	Hadamard product
$\otimes$	Kronecker product
$(\cdot)_{[x:y]}$	Shortcut for $(\cdot)_x, (\cdot)_{x+1}, \ldots, (\cdot)_y$

Distributions

$\sim$	Follows a distribution
$\mathcal{CN}(\mathbf{0}, \boldsymbol{\Sigma})$	Multivariate Circularly Symmetric Complex Gaussian with covariance $\boldsymbol{\Sigma}$

Subscripts

$(\cdot)_B$	Backward
$(\cdot)_D$	Direct
$(\cdot)_F$	Forward
$(\cdot)_I$	Information
$(\cdot)_P$	Power

Superscripts

$(\cdot)^{(r)}$	r-th iterated value
$(\cdot)^\star$	Stationary point

Chapter 1

Introduction

1.1 Motivation

The quest for reliable, high-speed, and ubiquitous wireless connectivity has been long-standing since Marconi's illuminating radio in 1895. Great successes have been made at the transmitter and receiver sides over the past century, and the communications society is unprecedentedly close to the Shannon limit [2]. Today we are witnessing a paradigm shift from *connectivity* to *intelligence*, where the wireless environment is no longer a chaotic medium but a conscious agent that can serve on demand. This is made possible by the latest advances in machine learning and programmable metamaterials — the former enables the network to learn from the environment while the latter allows the environment to adapt to the network. Together, they form a symbiotic relationship that can revolutionize the way we communicate, sense, and interact with the world. One promising candidate to fulfill this vision is Reconfigurable Intelligent Surface (RIS), a programmable metasurface that recycles and redistributes the electromagnetic waves in the air for improved wireless performance. This disruptive technology can be integrated into the next-generation wireless systems for signal enhancement, interference suppression, scattering enrichment, blockage bypassing, coverage extension, and security control. Compared with traditional multi-antenna techniques, RIS has the potential to achieve a similar performance using fewer active components, lower power consumption, and lower hardware complexity. RIS is also different from conventional relays as it features no Radio-Frequency (RF) chains, no symbol dependency, minimum signal processing, and negligible additional noise. Moreover, it can be easily deployed in various forms (e.g., walls, windows, ceilings, tables) to provide seamless coverage and powerful customization for indoor and outdoor environments. These unique characteristics make RIS a ubiquitous and cost-effective solution for future communication, sensing, and power transfer systems.

Despite the great possibilities, the prototyping of RIS is still in its infancy and no commercial product has been released by the first quarter of 2024. The transition from theory to practice is hindered by many challenges, such as channel acquisition, response resolution, out-of-band response mitigation, placement optimization, and integration with existing systems. Most importantly, a comprehensive understanding of its potential is still missing and the precise role it shall play in 6G remains ambiguous. For example, RIS could be incorporated into the transmitter and receiver for *beamforming*, employed as a free-rider information source for *modulation*, or placed in space as a standalone device for *channel shaping*. These applications have distinctive requirements and trade-offs, but they are not mutually exclusive and may be evolved into a versatile tool, which blurs the boundary between the network and environment. Imagine a future where everything can be "smartened" by coating with a metamaterial layer and attaching a microcontroller tag. Only a few electromagnetic sources are needed, while most objects can exploit the surrounding waves to energize themselves, sense the environment, communicate with others, and help those in need when idle. To realize this vision, we need to:

- investigate the impact of RIS on various wireless applications and propose effective configurations for enhanced performance trade-off;

- compare the principles of RIS with other scatter-based technologies and develop a novel protocol for beamforming-modulation integration;

- rethink the architecture and modeling of RIS and explore its ultimate performance limits for further design evolution;

which are the motivations for Chapters 3–5 of this thesis, respectively.

1.2 Objectives

1.3 Outline and Contributions

1.4 Publications

Chapter 2

Background and Literature Review

2.1 Reconfigurable Intelligent Surface (RIS)

2.1.1 Hardware Implementation

Programmable Metamaterials

Physical Architecture

2.1.2 Wave Scattering Model

Active and Passive Elements

Independent Scattering: Diagonal Model

Cooperative Scattering: Beyond-Diagonal (BD) Model

Impact of Radiation Pattern and Circuit Topology

2.1.3 Comparison with Reflectarrays and Relays

Functionality

Reconfigurability

Complexity

Power Consumption

Dimension and Cost

Applications

2.2 Wireless Power Transfer (WPT)

2.2.1 Near- and Far-Field Techniques

2.2.2 Modules and Coupling Effect

Chapter 3

RIS-Aided SWIPT: Joint Waveform and Beamforming Design

3.1 Introduction

3.1.1 Simultaneous Wireless Information and Power Transfer

With the great advance in communication performance, a bottleneck of wireless networks has come to energy supply. Simultaneous Wireless Information and Power Transfer (SWIPT) is a promising solution to connect and power mobile devices via RF waves. It provides low power at μW level but broad coverage up to hundreds of meters in a sustainable and controllable manner, bringing more opportunities to the Internet of Things (IoT) and Machine-to-Machine (M2M) networks. The upsurge in wireless devices, together with the decrease of electronics power consumption, calls for a re-thinking of future wireless networks based on Wireless Power Transfer (WPT) and SWIPT [3].

The concept of SWIPT was first cast in [4], where the authors investigated the Rate-Energy (R-E) tradeoff for a flat Gaussian channel and typical discrete channels. [5] proposed two practical co-located information and power receivers, i.e., Time Switching (TS) and Power Splitting (PS). Dedicated information and energy beamforming were then investigated in [6, 7] to characterize the R-E region for multi-antenna broadcast and interference channels. On the other hand, [8] pointed out that the RF-to-Direct Current (DC) conversion efficiency of rectifiers depends on the input power and waveform shape. It implies that the modeling of the energy harvester, particularly its nonlinearity, has a crucial impact on the waveform preference, resource allocation, and system design of any wireless-powered systems [8, 9, 3]. Motivated by this, [10] derived a tractable nonlinear harvester model based on the Taylor expansion of diode I-V characteristics, and performed joint waveform and beamforming design for WPT.

Simulation and experiments showed the benefit of modeling energy harvester nonlinearity in real system design [11, 12] and demonstrated the joint waveform and beamforming strategy as a key technique to expand the operation range [13]. A low-complexity adaptive waveform design by Scaled Matched Filter (SMF) was proposed in [14] to exploit the rectifier nonlinearity, whose advantage was then demonstrated in a prototype with channel acquisition [15]. Beyond WPT, [16] uniquely showed that the rectifier nonlinearity brings radical changes to SWIPT design, namely (i) modulated and unmodulated waveforms are not equally suitable for wireless power delivery; (ii) a multi-carrier unmodulated waveform superposed to a multi-carrier modulated waveform can enlarge the R-E region; (iii) a combination of PS and TS is generally the best strategy; (iv) the optimal input distribution is not the conventional Circularly Symmetric Complex Gaussian (CSCG); (v) modeling rectifier nonlinearity is beneficial to system performance and essential to efficient SWIPT design. Those observations, validated experimentally in [11], led to the question: *What is the optimal input distribution for SWIPT under nonlinearity?* This question was answered in [17] for single-carrier SWIPT, and some attempts were further made in [18] for multi-carrier SWIPT. The answers shed new light to the fundamental limits of SWIPT and practical signaling (e.g., modulation and waveform) strategies. It is now well understood from [16–18] that, due to harvester nonlinearity, a combination of CSCG and on-off keying in single-carrier setting and non-zero mean asymmetric inputs in multi-carrier setting lead to significantly larger R-E region compared to conventional CSCG. Recently, [19] used machine learning techniques to design SWIPT signaling under nonlinearity to complement the information-theoretic results of [17], and new modulation schemes were subsequently invented.

3.1.2   Reconfigurable Intelligent Surface

RIS has recently emerged as a promising technique that adapts the propagation environment to enhance the spectrum and energy efficiency. In practice, a RIS consists of multiple individual sub-wavelength reflecting elements to adjust the amplitude and phase of the incoming signal (i.e., passive beamforming). Different from the relay, backscatter and frequency-selective surface [20], the RIS assists the primary transmission using passive components with negligible thermal noise but is limited to frequency-dependent reflection.

Inspired by the development of real-time reconfigurable metamaterials [21], the authors of [22] introduced a programmable metasurface that steers or polarizes the electromagnetic wave at a specific frequency to mitigate signal attenuation. [23] proposed a RIS-assisted Multiple-Input Single-Output (MISO) system and jointly optimized the precoder at the Access Point (AP) and the phase shifts at the RIS to minimize the transmit power. The active and passive beamforming problem was then extended to the discrete phase shift case [24] and the

multi-user case [25]. In [26], the authors investigated the impact of non-zero resistance on the reflection pattern and emphasized the coupling between reflection amplitude and phase shift in practice. To estimate the cascaded AP-RIS-User Equipment (UE) link without RF-chains at the RIS, practical protocols were developed based on element-wise on/off switching [27], training sequence and reflection pattern design [28, 29], and compressed sensing [30]. The hardware architecture, design challenges, and application opportunities of practical RIS were covered in [31]. In [32], a prototype RIS with 256 2-bit elements based on Positive Intrinsic Negative (PIN) diodes was developed to support real-time video transmission at GHz and mmWave frequency.

3.1.3 RIS-Aided SWIPT

By integrating RIS with SWIPT, the constructive reflection can boost the end-to-end power efficiency and improve the R-E tradeoff. In multi-user cases, dedicated energy beams were proved unnecessary for the weighted sum-power maximization [33] but essential when fairness issue is considered [34]. It was also claimed that Line-of-Sight (LoS) links could boost the power efficiency since rank-deficient channels require fewer energy beams [35]. However, [33–35] were based on a linear energy harvester model that is known in both the RF and the communication literature to be inefficient and inaccurate [3, 8–19]. Based on practical RIS and harvester models, [36] introduced a scalable resource allocation framework for a large-scale tile-based RIS-assisted SWIPT system, where the optimization consists of a reflection design stage and a joint reflection selection and precoder design stage. The proposed framework provides a flexible tradeoff between performance and complexity. To the best of our knowledge, all existing papers considered resource allocation and beamforming design for dedicated information and energy users in a single-carrier network. In this paper, we instead build our design based on a proper nonlinear harvester model that captures the dependency of the output DC power on both the power and shape of the input waveform, and marry the benefits of joint multi-carrier waveform and active beamforming optimization for SWIPT with the passive beamforming capability of RIS, to investigate the R-E tradeoff for one SWIPT user with co-located information decoder and energy harvester. We ask ourselves the important question: *How to jointly exploit the spatial domain and the frequency domain efficiently through joint waveform and beamforming design to enlarge the R-E region of RIS-aided SWIPT?* The contributions of this paper are summarized as follows.

First, we propose a novel RIS-aided SWIPT architecture based on joint waveform, active and passive beamforming design under the diode nonlinear model [10]. Although this tractable harvester model accurately reveals how the input power level and waveform shape influence the output DC power, it also introduces design challenges such as frequency coupling

(i.e., components of different frequencies compensate and produce DC), waveform coupling (i.e., different waveforms jointly contribute to DC), and high-order objective function. To make an efficient use of the rectifier nonlinearity, we superpose a multi-carrier unmodulated power waveform (deterministic multisine) to a multi-carrier modulated information waveform and evaluate the performance under the TS and PS receiving modes. The proposed joint waveform, active and passive beamforming architecture exploits the rectifier nonlinearity, the channel selectivity, and a beamforming gain across frequency and spatial domains to enlarge the achievable R-E region. This is the first paper to propose a joint waveform, active and passive beamforming architecture for RIS-aided SWIPT.

Second, we characterize each R-E boundary point by energy maximization under a rate constraint. The problem is solved by a Block Coordinate Descent (BCD) algorithm based on the Channel State Information at the Transmitter (CSIT). For active beamforming, we prove that the global optimal active information and power precoders coincide at Maximum Ratio Transmission (MRT) even with rectifier nonlinearity. For passive beamforming, we propose a Successive Convex Approximation (SCA) algorithm and retrieve the RIS phase shift by eigen decomposition with optimality proof. Finally, the superposed waveform and the splitting ratio are optimized by the Geometric Programming (GP) technique. The RIS phase shift, active precoder, and waveform amplitude are updated iteratively until convergence. This is the first paper to jointly optimize waveform and active/passive beamforming in RIS-aided SWIPT.

Third, we introduce two closed-form adaptive waveform schemes to avoid the exponential complexity of the GP algorithm. To facilitate practical SWIPT implementation, the Water-Filling (WF) strategy for modulated waveform and the SMF strategy for multisine waveform are combined in time and power domains, respectively. The passive beamforming design is also adapted to accommodate the low-complexity waveform schemes. The proposed low-complexity BCD algorithm achieves a good balance between performance and complexity.

Fourth, we provide numerical results to evaluate the proposed algorithms. It is concluded that (i) RIS enables constructive reflection and flexible subchannel design in the frequency domain that is essential for SWIPT systems; (ii) RIS mainly affects the effective channel instead of the waveform design; (iii) multisine waveform is beneficial to energy transfer especially when the number of subbands is large; (iv) TS is preferred at low Signal-to-Noise Ratio (SNR) while PS is preferred at high SNR; (v) there exist two optimal RIS development locations, one close to the AP and one close to the UE; (vi) the output SNR scales linearly with the number of transmit antennas and quadratically with the number of RIS elements; (vii) due to the rectifier nonlinearity, the output DC scales quadratically with the number of transmit antennas and quartically with the number of RIS elements; (viii) for narrowband SWIPT, the optimal active and passive beamforming for any R-E point are also optimal for the
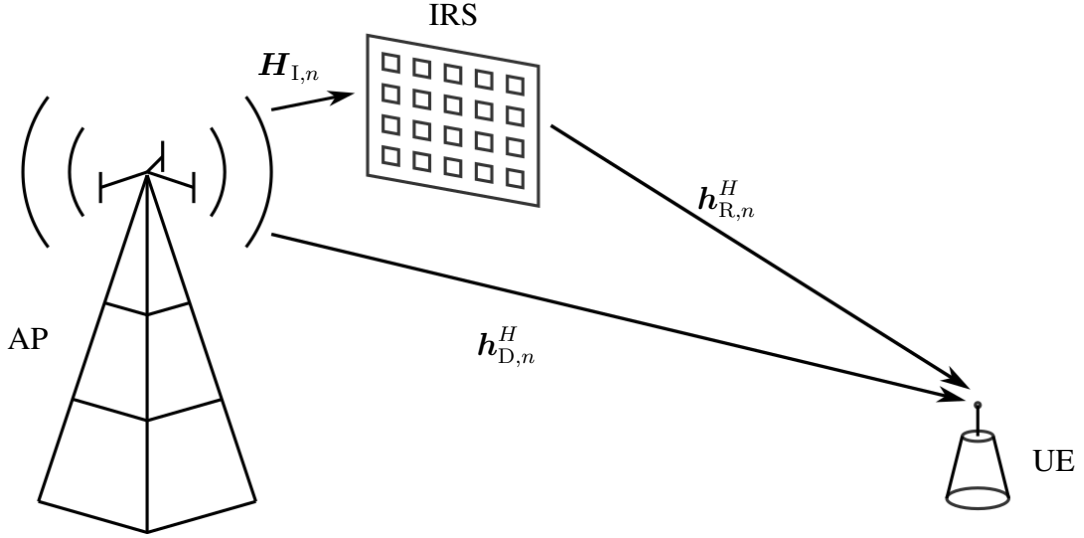
Fig. 3.1 An RIS-aided multi-carrier MISO SWIPT system.

whole R-E region; (ix) for broadband SWIPT, the optimal active and passive beamforming depend on specific R-E point and require adaptive designs; (x) the proposed algorithms are robust to practical impairments such as inaccurate cascaded CSIT and finite RIS reflection states.

3.2 System Model

As shown in Fig. 3.1, we propose a RIS-aided SWIPT system where an M-antenna AP delivers information and power simultaneously, through an L-element RIS, to a single-antenna UE over N orthogonal evenly-spaced subbands. We consider a quasi-static block fading model and assume the CSIT of direct and cascaded channels is known. The signals reflected by two or more times are omitted, and the noise power is assumed too small to be harvested.

3.2.1 Transmitted Signal

Following [16], we superpose a multi-carrier modulated information-bearing waveform to a multi-carrier unmodulated power-dedicated deterministic multisine to boost the spectrum and energy efficiency. The information signal transmitted over subband $n \in \{1, \dots, N\}$ at time t is

$$\boldsymbol{x}_{\mathrm{I},n}(t) = \Re \left\{ \boldsymbol{w}_{\mathrm{I},n} \tilde{x}_{\mathrm{I},n}(t) e^{j2\pi f_n t} \right\}, \tag{3.1}$$

where $\boldsymbol{w}_{\mathrm{I},n} \in \mathbb{C}^{M \times 1}$ is the information precoder at subband n, $\tilde{x}_{\mathrm{I},n} \sim \mathcal{CN}(0,1)$ is the information symbol at subband n, and f_n is the frequency of subband n. On the other hand,

the power signal transmitted over subband n at time t is

$$\boldsymbol{x}_{\mathrm{P},n}(t) = \Re\left\{\boldsymbol{w}_{\mathrm{P},n}e^{j2\pi f_n t}\right\}, \tag{3.2}$$

where $\boldsymbol{w}_{\mathrm{P},n} \in \mathbb{C}^{M\times 1}$ is the power precoder at subband n. Therefore, the superposed signal transmitted over all subbands at time t is

$$\boldsymbol{x}(t) = \Re\left\{\sum_{n=1}^{N}(\boldsymbol{w}_{\mathrm{I},n}\tilde{x}_{\mathrm{I},n}(t) + \boldsymbol{w}_{\mathrm{P},n})e^{j2\pi f_n t}\right\}. \tag{3.3}$$

We also define $\boldsymbol{w}_{\mathrm{I/P}} \triangleq [\boldsymbol{w}_{\mathrm{I/P},1}^T, \ldots, \boldsymbol{w}_{\mathrm{I/P},N}^T]^T \in \mathbb{C}^{MN\times 1}$.

3.2.2 Reflection Pattern and Composite Channel

According to Green's decomposition [37], the backscattered signal of an antenna can be decomposed into the *structural mode* component and the *antenna mode* component. The former is fixed and can be regarded as part of the environment multipath, while the latter is adjustable and depends on the mismatch of the antenna and load impedance. RIS element $l \in \{1, \ldots, L\}$ varies its impedance $Z_l = R_l + jX_l$ to reflect the incoming signal, and the reflection coefficient is defined as

$$\phi_l = \frac{Z_l - Z_0}{Z_l + Z_0} \triangleq \eta_l e^{j\theta_l}, \tag{3.4}$$

where Z_0 is the real-valued characteristic impedance, $\eta_l \in [0, 1]$ is the reflection amplitude,[1] and $\theta_l \in [0, 2\pi)$ is the phase shift. We also define $\boldsymbol{\phi} \triangleq [\phi_1, \ldots, \phi_L]^H \in \mathbb{C}^{L\times 1}$ and $\boldsymbol{\Theta} \triangleq \mathrm{diag}(\phi_1, \ldots, \phi_L) = \mathrm{diag}(\boldsymbol{\Phi}^*) \in \mathbb{C}^{L\times L}$ as the RIS vector and matrix, respectively.

Remark 1. *The element impedance Z_l maps to the reflection coefficient ϕ_l uniquely. Since the reactance X_l depends on the frequency, the reflection coefficient ϕ_l is also a function of frequency and cannot be designed independently at different subbands. In this paper, we assume the bandwidth is small compared to the operating frequency such that the reflection coefficient of each RIS element is the same at all subbands.*

At subband n, we denote the AP-UE direct channel as $\boldsymbol{h}_{\mathrm{D},n}^H \in \mathbb{C}^{1\times M}$, the AP-RIS incident channel as $\boldsymbol{H}_{\mathrm{I},n} \in \mathbb{C}^{L\times M}$, and the RIS-UE reflected channel as $\boldsymbol{h}_{\mathrm{R},n}^H \in \mathbb{C}^{1\times L}$. The auxiliary AP-RIS-UE link can be modeled as a concatenation of the incident channel, the RIS reflection,

---

[1]Due to the non-zero power consumption at the RIS, $R_l > 0$ in practice such that $\eta_l < 1$ and is a function of θ_l. This paper sticks to the most common RIS model where the reflection amplitude equals 1 so as to reduce the design complexity and provide a primary benchmark for practical RIS-aided SWIPT.

and the reflected channel. Hence, the composite equivalent channel reduces to

$$\boldsymbol{h}_n^H = \boldsymbol{h}_{\mathrm{D},n}^H + \boldsymbol{h}_{\mathrm{R},n}^H \boldsymbol{\Theta} \boldsymbol{H}_{\mathrm{I},n} = \boldsymbol{h}_{\mathrm{D},n}^H + \boldsymbol{\phi}^H \boldsymbol{V}_n, \tag{3.5}$$

where we define the cascaded incident-reflected channel at subband n as $\boldsymbol{V}_n \triangleq \mathrm{diag}(\boldsymbol{h}_{\mathrm{R},n}^H)\boldsymbol{H}_{\mathrm{I},n} \in \mathbb{C}^{L \times M}$. We also define $\boldsymbol{h} \triangleq [\boldsymbol{h}_1^T, \ldots, \boldsymbol{h}_N^T]^T \in \mathbb{C}^{MN \times 1}$.

Remark 2. *The cascaded channel varies at different subbands, but the reflection cannot be designed independently at different frequencies. Therefore, there exists a tradeoff for the passive beamforming design in the frequency domain, and the composite subchannels should be tuned adaptively to meet the specific requirement of multi-carrier SWIPT. For example, one can design the reflection pattern to either enhance the strongest subband (e.g., $\max_{\phi,n}\|\boldsymbol{h}_n\|$), or improve the fairness among subbands (e.g., $\max_{\phi} \min_n \|\boldsymbol{h}_n\|$). That is to say, RIS essentially enables a flexible subchannel design. In the MISO case, a similar effect also exists in the spatial domain. Therefore, each reflection coefficient is indeed shared by M antennas over N subbands.*

3.2.3   Received Signal

The received superposed signal at the single-antenna UE is[2]

$$y(t) = \Re \left\{ \sum_{n=1}^{N} \left(\boldsymbol{h}_n^H (\boldsymbol{w}_{\mathrm{I},n} \tilde{x}_{\mathrm{I},n}(t) + \boldsymbol{w}_{\mathrm{P},n}) + \tilde{n}_n(t) \right) e^{j2\pi f_n t} \right\}, \tag{3.6}$$

where $\tilde{n}_n(t)$ is the noise at RF band n. Note that the modulated component can be used for energy harvesting if necessary, but the multisine component carries no information and cannot be used for information decoding.

3.2.4   Receiving Modes

As illustrated in Fig. 3.2, there are two practical receiving modes for the co-located information decoder and energy harvester [5]. The TS receiver divides each transmission block into orthogonal data and energy sessions with duration $1 - \eta$ and η, respectively. During each session, the transmitter optimizes the waveform for either Wireless Information Transfer (WIT) or WPT, while the receiver activates the information decoder or the energy harvester correspondingly. The duration ratio η controls the R-E tradeoff and is independent from the

---

[2]We assume that the time difference of signal arrival via direct and auxiliary link is negligible compared to the symbol period.

(a) TS receiver
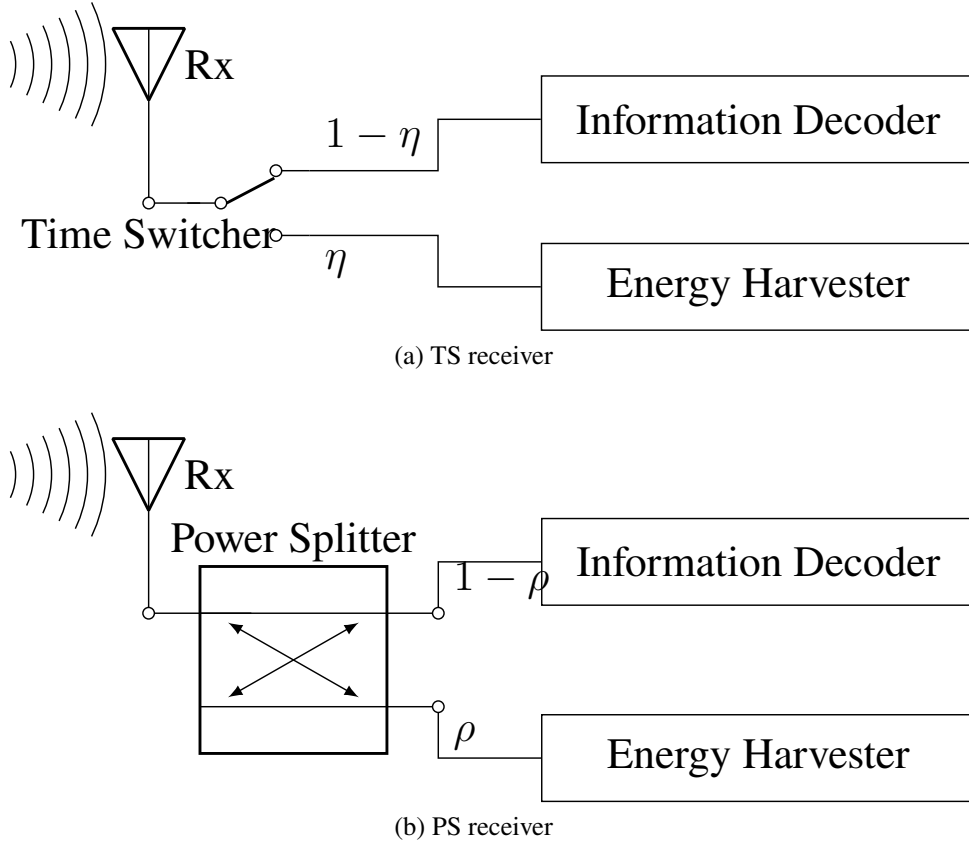
(b) PS receiver

Fig. 3.2 Diagrams of practical co-located receivers.

waveform and beamforming design. On the other hand, the PS receiver splits the incoming signal into individual data and energy streams with power ratio $1 - \rho$ and ρ, respectively. The data stream is fed into the information decoder while the energy stream is fed into the energy harvester. During each transmission block, the superposed waveform and splitting ratio are jointly designed to achieve different R-E tradeoffs. In the following context, we consider the optimization with the PS receiver, as the TS receiver can be regarded as a special case (i.e., a time sharing between $\rho = 0$ and $\rho = 1$).

3.2.5 Information Decoder

A major benefit of the superposed waveform is that the multisine is deterministic and creates no interference to the modulated waveform [16]. Therefore, the achievable rate is[3]

$$R(\boldsymbol{\phi}, \boldsymbol{w}_{\mathrm{I}}, \rho) = \sum_{n=1}^{N} \log_2 \left(1 + \frac{(1-\rho)|\boldsymbol{h}_n^H \boldsymbol{w}_{\mathrm{I},n}|^2}{\sigma_n^2} \right), \tag{3.7}$$

---

[3]It requires waveform cancellation or translated demodulation [16].

(a) Antenna equivalent circuit   (b) A single diode rectifier
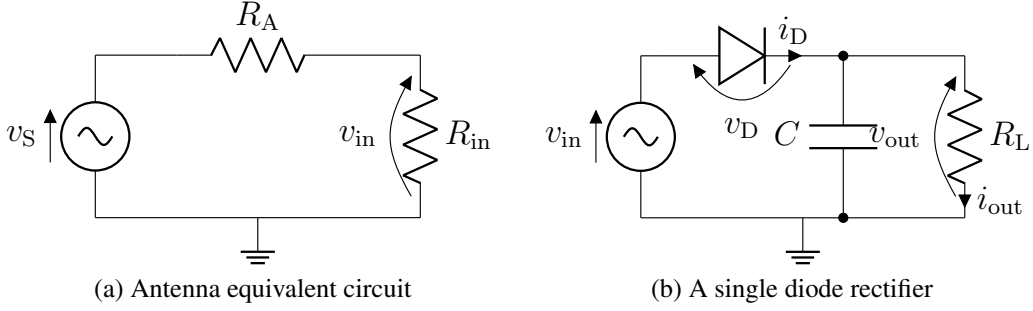
Fig. 3.3 Equivalent circuits of receive antenna and energy harvester.

where σ_n^2 is the noise variance at the RF-band and during the RF-to-baseband conversion on tone n.

3.2.6 Energy Harvester

Taken from [10], the rectenna model used in this section captures the dependency of the output DC on both the power and shape of the received signal. Fig. 3.3(a) illustrates the equivalent circuit of an ideal antenna, where the antenna has a resistance R_A and the incoming signal creates a voltage source $v_S(t)$. Let R_{in} be the total input resistance of the rectifier and matching network, and we assume the voltage across the matching network is negligible. When perfectly matched (i.e., $R_{in} = R_A$), the rectifier input voltage is $v_{in}(t) = y(t)\sqrt{\rho R_A}$. Consider a simplified rectifier model in Fig. 3.3(b) where a single series diode is followed by a low-pass filter with a parallel load. As detailed in [16], a truncated Taylor expansion of the diode I-V characteristic equation suggests that maximizing the average output DC is equivalent to maximizing a monotonic function[4]

$$z(\boldsymbol{\phi}, \boldsymbol{w}_I, \boldsymbol{w}_P, \rho) = \sum_{i\,\mathrm{even},i\geq 2}^{n_0} k_i \rho^{i/2} R_A^{i/2} \mathbb{E}\left\{\mathbb{A}\left\{y(t)^i\right\}\right\}, \tag{3.8}$$

where n_0 is the truncation order and $k_i \triangleq i_S/i!(n'v_T)^i$ is the diode coefficient (i_S is the reverse bias saturation current, n' is the diode ideality factor, v_T is the thermal voltage). With a slight abuse of notation, we refer to z as the average output DC in this paper. It can be observed that the conventional linear harvester model, where the output DC power equals the sum of the power harvested on each frequency, is a special case of (3.8) with $n_0 = 2$. However, due to the coupling effect among different frequencies, some high-order frequency components

---

[4]This small-signal expansion model is only valid for the nonlinear operation region of the diode, and the I-V relationship would be linear if the diode behavior is dominated by the load [10].

Fig. 3.4 $\boldsymbol{W}_{\mathrm{I/P}}$ consists of $N \times N$ blocks of size $M \times M$. $\boldsymbol{W}_{\mathrm{I/P},k}$ keeps the k-th block diagonal of $\boldsymbol{W}_{\mathrm{I/P}}$ and nulls all remaining blocks. Solid, dashed and dotted blocks correspond to $k > 0$, $k = 0$ and $k < 0$, respectively. For $\boldsymbol{w}_{\mathrm{I/P},n_1} \boldsymbol{w}_{\mathrm{I/P},n_2}^H$, the k-th block diagonal satisfies $k = n_2 - n_1$.

compensate each other in frequency and further contribute to the output DC power. In other words, even-order terms with $i \geq 4$ account for the nonlinear diode behavior. For simplicity, we choose $n_0 = 4$ to investigate the fundamental rectifier nonlinearity, and define $\beta_2 \triangleq k_2 R_{\mathrm{A}}$, $\beta_4 \triangleq k_4 R_{\mathrm{A}}^2$ to rewrite z by (3.9). Note that $\mathbb{E}\{|\tilde{x}_{\mathrm{I},n}|^2\} = 1$ but $\mathbb{E}\{|\tilde{x}_{\mathrm{I},n}|^4\} = 2$ applies a modulation gain on the fourth-order DC terms. Let $\boldsymbol{W}_{\mathrm{I/P}} \triangleq \boldsymbol{w}_{\mathrm{I/P}} \boldsymbol{w}_{\mathrm{I/P}}^H \in \mathbb{C}^{MN \times MN}$. As illustrated by Fig. 3.4, $\boldsymbol{W}_{\mathrm{I/P}}$ can be divided into $N \times N$ blocks of size $M \times M$, and we let $\boldsymbol{W}_{\mathrm{I/P},k}$ keep its block diagonal $k \in \{-N+1, \ldots, N-1\}$ and set all other blocks to $\boldsymbol{0}$. Hence, the components of z reduce to (3.10)–(3.13) [38].

3.2.7 Rate-Energy Region

The achievable R-E region is defined as

$$\mathcal{C}_{\mathrm{R-E}} \triangleq \left\{ (R_{\mathrm{ID}}, z_{\mathrm{EH}}) \in \mathbb{R}_+^2 \mid R_{\mathrm{ID}} \leq R, z_{\mathrm{EH}} \leq z, \right.$$
$$\left. \frac{1}{2} \left(\|\boldsymbol{w}_{\mathrm{I}}\|^2 + \|\boldsymbol{w}_{\mathrm{P}}\|^2 \right) \leq P \right\}, \tag{3.14}$$

where P is the average transmit power budget and 1/2 converts the peak value of the sine waves to the average value.

3.3   Problem Formulation

We characterize each R-E boundary point through a current maximization problem subject to sum rate, transmit power, and reflection amplitude constraints as

$$\max_{\boldsymbol{\phi}, \boldsymbol{w}_{\mathrm{I}}, \boldsymbol{w}_{\mathrm{P}}, \rho} \quad z(\boldsymbol{\phi}, \boldsymbol{w}_{\mathrm{I}}, \boldsymbol{w}_{\mathrm{P}}, \rho) \tag{3.15a}$$

$$\text{s.t.} \quad R(\boldsymbol{\phi}, \boldsymbol{w}_{\mathrm{I}}, \rho) \geq \bar{R}, \tag{3.15b}$$

$$\frac{1}{2}\left(\|\boldsymbol{w}_{\mathrm{I}}\|^2 + \|\boldsymbol{w}_{\mathrm{P}}\|^2\right) \leq P, \tag{3.15c}$$

$$|\boldsymbol{\phi}| = \mathbf{1}, \tag{3.15d}$$

$$0 \leq \rho \leq 1. \tag{3.15e}$$

Problem (3.15) is intricate because of the coupled variables in (3.15a), (3.15b) and the non-convex constraint (3.15d). To obtain a feasible solution, we propose a BCD algorithm that iteratively updates (i) the RIS phase shift; (ii) the active precoder; (iii) the waveform amplitude and splitting ratio, until convergence.

$$z(\boldsymbol{\phi}, \boldsymbol{w}_{\mathrm{I}}, \boldsymbol{w}_{\mathrm{P}}, \rho) = \beta_2 \rho \Big(\mathbb{E}\left\{ \mathbb{A}\left\{ y_{\mathrm{I}}^2(t) \right\} \right\} + \mathbb{A}\left\{ y_{\mathrm{P}}^2(t) \right\} \Big) + \beta_4 \rho^2 \Big(\mathbb{E}\left\{ \mathbb{A}\left\{ y_{\mathrm{I}}^4(t) \right\} \right\} + \mathbb{A}\left\{ y_{\mathrm{P}}^4(t) \right\} + 6\mathbb{E}\left\{ \mathbb{A}\left\{ y_{\mathrm{I}}^2($$

$$\tag{3.9}$$

$$\mathbb{E}\left\{ \mathbb{A}\left\{ y_{\mathrm{I}}^2(t) \right\} \right\} = \frac{1}{2} \sum_{n=1}^{N} (\boldsymbol{h}_n^H \boldsymbol{w}_{\mathrm{I},n})(\boldsymbol{h}_n^H \boldsymbol{w}_{\mathrm{I},n})^* = \frac{1}{2} \boldsymbol{h}^H \boldsymbol{W}_{\mathrm{I},0} \boldsymbol{h}, \tag{3.10}$$

$$\mathbb{E}\left\{ \mathbb{A}\left\{ y_{\mathrm{I}}^4(t) \right\} \right\} = \frac{3}{4} \left(\sum_{n=1}^{N} (\boldsymbol{h}_n^H \boldsymbol{w}_{\mathrm{I},n})(\boldsymbol{h}_n^H \boldsymbol{w}_{\mathrm{I},n})^* \right)^2 = \frac{3}{4} (\boldsymbol{h}^H \boldsymbol{W}_{\mathrm{I},0} \boldsymbol{h})^2, \tag{3.11}$$

$$\mathbb{A}\left\{ y_{\mathrm{P}}^2(t) \right\} = \frac{1}{2} \sum_{n=1}^{N} (\boldsymbol{h}_n^H \boldsymbol{w}_{\mathrm{P},n})(\boldsymbol{h}_n^H \boldsymbol{w}_{\mathrm{P},n})^* = \frac{1}{2} \boldsymbol{h}^H \boldsymbol{W}_{\mathrm{P},0} \boldsymbol{h}, \tag{3.12}$$

$$\mathbb{A}\left\{ y_{\mathrm{P}}^4(t) \right\} = \frac{3}{8} \sum_{\substack{n_1,n_2,n_3,n_4 \\ n_1+n_2=n_3+n_4}} (\boldsymbol{h}_{n_1}^H \boldsymbol{w}_{\mathrm{P},n_1})(\boldsymbol{h}_{n_2}^H \boldsymbol{w}_{\mathrm{P},n_2})(\boldsymbol{h}_{n_3}^H \boldsymbol{w}_{\mathrm{P},n_3})^*(\boldsymbol{h}_{n_4}^H \boldsymbol{w}_{\mathrm{P},n_4})^* = \frac{3}{8} \sum_{k=-N+1}^{N-1} (\boldsymbol{h}^H \boldsymbol{W}_{\mathrm{P},k} \boldsymbol{h})(\boldsymbol{h}^H$$

$$\tag{3.13}$$

3.3.1   Passive Beamforming

In this section, we optimize the RIS phase shift ϕ for any given waveform $w_{\mathrm{I/P}}$ and splitting ratio ρ. Note that

$$
\begin{aligned}
|h_n^H w_{\mathrm{I},n}|^2 &= w_{\mathrm{I},n}^H h_n h_n^H w_{\mathrm{I},n} \\
&= w_{\mathrm{I},n}^H (h_{\mathrm{D},n} + V_n^H \phi)(h_{\mathrm{D},n}^H + \phi^H V_n) w_{\mathrm{I},n} \\
&= w_{\mathrm{I},n}^H M_n^H \Phi M_n w_{\mathrm{I},n} \\
&= \mathrm{tr}(M_n w_{\mathrm{I},n} w_{\mathrm{I},n}^H M_n^H \Phi) \\
&= \mathrm{tr}(C_n \Phi),
\end{aligned}
\tag{3.16}
$$

where $M_n \triangleq [V_n^H, h_{\mathrm{D},n}]^H \in \mathbb{C}^{(L+1) \times M}$, t' is an auxiliary variable with unit modulus, $\bar{\phi} \triangleq [\phi^H, t']^H \in \mathbb{C}^{(L+1) \times 1}$, $\Phi \triangleq \bar{\phi} \bar{\phi}^H \in \mathbb{C}^{(L+1) \times (L+1)}$, $C_n \triangleq M_n w_{\mathrm{I},n} w_{\mathrm{I},n}^H M_n^H \in \mathbb{C}^{(L+1) \times (L+1)}$. On the other hand, we define $t_{\mathrm{I/P},k}$ as

$$
\begin{aligned}
t_{\mathrm{I/P},k} &\triangleq h^H W_{\mathrm{I/P},k} h \\
&= \mathrm{tr}(h h^H W_{\mathrm{I/P},k}) \\
&= \mathrm{tr}\left((h_D + V^H \phi)(h_D^H + \phi^H V) W_{\mathrm{I/P},k}\right) \\
&= \mathrm{tr}(M^H \Phi M W_{\mathrm{I/P},k}) \\
&= \mathrm{tr}(M W_{\mathrm{I/P},k} M^H \Phi) \\
&= \mathrm{tr}(C_{\mathrm{I/P},k} \Phi),
\end{aligned}
\tag{3.17}
$$

where $V \triangleq [V_1, \ldots, V_N] \in \mathbb{C}^{L \times MN}$, $M \triangleq [V^H, h_D]^H \in \mathbb{C}^{(L+1) \times MN}$, $C_{\mathrm{I/P},k} \triangleq M W_{\mathrm{I/P},k} M^H \in \mathbb{C}^{(L+1) \times (L+1)}$. On top of this, (3.7) and (3.9) reduce respectively to

$$
R(\Phi) = \sum_{n=1}^{N} \log_2 \left(1 + \frac{(1-\rho)\mathrm{tr}(C_n \Phi)}{\sigma_n^2}\right),
\tag{3.18}
$$

$$
\begin{aligned}
z(\Phi) = \frac{1}{2}\beta_2 \rho (t_{\mathrm{I},0} + t_{\mathrm{P},0}) + \frac{3}{8}\beta_4 \rho^2 \left(2t_{\mathrm{I},0}^2 + \sum_{k=-N+1}^{N-1} t_{\mathrm{P},k} t_{\mathrm{P},k}^*\right) \\
+ \frac{3}{2}\beta_4 \rho^2 t_{\mathrm{I},0} t_{\mathrm{P},0}.
\end{aligned}
\tag{3.19}
$$

To maximize the non-concave expression (3.19), we successively lower bound the second-order terms by their first-order Taylor expansions [39]. Based on the solution at iteration

$i - 1$, the approximations at iteration i are

$$(t_{\text{I},0}^{(i)})^2 \geq 2t_{\text{I},0}^{(i)}t_{\text{I},0}^{(i-1)} - (t_{\text{I},0}^{(i-1)})^2, \tag{3.20}$$

$$t_{\text{P},k}^{(i)}(t_{\text{P},k}^{(i)})^* \geq 2\Re\left\{t_{\text{P},k}^{(i)}(t_{\text{P},k}^{(i-1)})^*\right\} - t_{\text{P},k}^{(i-1)}(t_{\text{P},k}^{(i-1)})^*, \tag{3.21}$$

$$t_{\text{I},0}^{(i)}t_{\text{P},0}^{(i)} \geq t_{\text{I},0}^{(i)}t_{\text{P},0}^{(i-1)} + t_{\text{P},0}^{(i)}t_{\text{I},0}^{(i-1)} - t_{\text{I},0}^{(i-1)}t_{\text{P},0}^{(i-1)}. \tag{3.22}$$

Note that $t_{\text{I/P},0} = \text{tr}(\mathbf{C}_{\text{I/P},0}\mathbf{\Phi})$ is real-valued because $\mathbf{C}_{\text{I/P},0}$ and $\mathbf{\Phi}$ are Hermitian matrices. Due to symmetry [38], we have

$$\sum_{k=-N+1}^{N-1} \Re\left\{t_{\text{P},k}^{(i)}(t_{\text{P},k}^{(i-1)})^*\right\} = \sum_{k=-N+1}^{N-1} t_{\text{P},k}^{(i)}(t_{\text{P},k}^{(i-1)})^*. \tag{3.23}$$

Plugging (3.20)–(3.23) into (3.19), we obtain the DC approximation $\tilde{z}$ as (3.24) and transform problem (3.15) to

$$\max_{\mathbf{\Phi}} \quad \tilde{z}(\mathbf{\Phi}) \tag{3.25a}$$

$$\text{s.t.} \quad R(\mathbf{\Phi}) \geq \bar{R}, \tag{3.25b}$$

$$\text{diag}^{-1}(\mathbf{\Phi}) = \mathbf{1}, \tag{3.25c}$$

$$\mathbf{\Phi} \succeq \mathbf{0}, \tag{3.25d}$$

$$\text{rank}(\mathbf{\Phi}) = 1. \tag{3.25e}$$

We then apply Semi-Definite Relaxation (SDR) to the unit-rank constraint (3.25e) and formulate a Semi-Definite Programming (SDP) with approximation accuracy no greater than $\pi/4$ [40]. In this specific case, we found the solution provided by `CVX toolbox` [41] to (3.25a)-(3.25d) is always rank-1. This conclusion is summarized below.

Proposition 1. *Any optimal solution $\mathbf{\Phi}^\star$ to the relaxed passive beamforming problem* (3.25a)–(3.25d) *is rank-1 such that* (3.25e) *is tight and no loss is introduced by SDR.*

Proof. Please refer to Appendix 6.1.1. □

$$\tilde{z}(\mathbf{\Phi}^{(i)}) = \frac{1}{2}\beta_2\rho(t_{\text{I},0}^{(i)} + t_{\text{P},0}^{(i)}) + \frac{3}{8}\beta_4\rho^2\left(4t_{\text{I},0}^{(i)}t_{\text{I},0}^{(i-1)} - 2(t_{\text{I},0}^{(i-1)})^2 + \sum_{k=-N+1}^{N-1} 2t_{\text{P},k}^{(i)}(t_{\text{P},k}^{(i-1)})^* - t_{\text{P},k}^{(i-1)}(t_{\text{P},k}^{(i-1)})^*\right)$$

$$+ \frac{3}{2}\beta_4\rho^2\left(t_{\text{I},0}^{(i)}t_{\text{P},0}^{(i-1)} + t_{\text{P},0}^{(i)}t_{\text{I},0}^{(i-1)} - t_{\text{I},0}^{(i-1)}t_{\text{P},0}^{(i-1)}\right). \tag{3.24}$$

Algorithm 1 SCA: RIS Phase Shift.

1: **Input** β_2, β_4, $\boldsymbol{h}_{\mathrm{D},n}$, $\boldsymbol{V}_n$, σ_n, $\boldsymbol{w}_{\mathrm{I/P},n}$, ρ, $\bar{R}$, ϵ, $\forall n$
2: Construct $\boldsymbol{V}$, $\boldsymbol{M}$, $\boldsymbol{M}_n$, $\boldsymbol{C}_n$, $\boldsymbol{C}_{\mathrm{I/P},k}$, $\forall n, k$
3: **Initialize** $i \leftarrow 0$, $\boldsymbol{\Phi}^{(0)}$
4: Set $t_{\mathrm{I/P},k}^{(0)}$, $\forall k$ by (3.17)
5: Compute $z^{(0)}$ by (3.19)
6: **Repeat**
7:     $i \leftarrow i + 1$
8:     Get $\boldsymbol{\Phi}^{(i)}$ by solving (3.25a)–(3.25d)
9:     Update $t_{\mathrm{I/P},k}^{(i)}$, $\forall k$ by (3.17)
10:     Compute $z^{(i)}$ by (3.19)
11: **Until** $|z^{(i)} - z^{(i-1)}| \leq \epsilon$
12: Set $\boldsymbol{\Phi}^{\star} \leftarrow \boldsymbol{\Phi}^{(i)}$
13: Get $\hat{\boldsymbol{\phi}}^{\star}$ by eigen decomposition, $\boldsymbol{\Phi}^{\star} = \hat{\boldsymbol{\phi}}^{\star}(\hat{\boldsymbol{\phi}}^{\star})^H$
14: Set $\boldsymbol{\phi}^{\star} \leftarrow e^{j \arg\left([\hat{\boldsymbol{\phi}}^{\star}]_{(1:L)}/[\hat{\boldsymbol{\phi}}^{\star}]_{(L+1)}\right)}$
15: **Output** $\boldsymbol{\phi}^{\star}$

In summary, we update $\boldsymbol{\Phi}^{(i)}$ until convergence, extract $\hat{\boldsymbol{\phi}}^{\star}$ by eigen decomposition, and retrieve the RIS vector by $\boldsymbol{\phi}^{\star} = e^{j \arg\left([\hat{\boldsymbol{\phi}}^{\star}]_{(1:L)}/[\hat{\boldsymbol{\phi}}^{\star}]_{(L+1)}\right)}$. The passive beamforming design is summarized in the SCA Algorithm 1, where the relaxed problem (3.25a)–(3.25d) involves a $(L+1)$-order positive semi-definite matrix variable and $(L+2)$ linear constraints. Given a solution accuracy ϵ_{IPM} for the interior-point method, the computational complexity of Algorithm 1 is $\mathcal{O}\left(I_{\mathrm{SCA}}(L+2)^4(L+1)^{0.5}\log(\epsilon_{\mathrm{IPM}}^{-1})\right)$, where I_{SCA} denotes the number of SCA iterations [40].

Proposition 2. *For any feasible initial point with given waveform and splitting ratio, the SCA Algorithm 1 is guaranteed to converge to local optimal points of the original problem* (3.15).

Proof. Please refer to Appendix 6.1.2.   □

3.3.2   Active Beamforming

The original waveform and active beamforming problem (3.15) is over complex vectors $\boldsymbol{w}_{\mathrm{I/P}}$ of size $MN \times 1$. Next, we decouple the design in spatial and frequency domains, enable independent optimizations correspondingly, and reduce the size of variables from $2MN$ to $2(M+N)$. The weight on subband n is essentially

$$\boldsymbol{w}_{\mathrm{I/P},n} = s_{\mathrm{I/P},n}\boldsymbol{b}_{\mathrm{I/P},n}, \tag{3.26}$$

where $s_{\mathrm{I/P},n}$ denotes the amplitude of the modulated/multisine waveform at tone n, and $\boldsymbol{b}_{\mathrm{I/P},n}$ denotes the corresponding information/power precoder. Define $\boldsymbol{s}_{\mathrm{I/P}} \triangleq [s_{\mathrm{I/P},1}, \ldots, s_{\mathrm{I/P},N}]^T \in \mathbb{R}_+^{N \times 1}$. The MRT precoder at subband n is given by

$$\boldsymbol{b}_{\mathrm{I/P},n}^{\star} = \frac{\boldsymbol{h}_n}{\|\boldsymbol{h}_n\|}. \tag{3.27}$$

Proposition 3. *For single-user SWIPT, the global optimal information and power precoders coincide at the MRT.*

Proof. Please refer to Appendix 6.1.3.   □

3.3.3   Waveform and Splitting Ratio

Next, we jointly optimize the waveform amplitude $\boldsymbol{s}_{\mathrm{I/P}}$ and the splitting ratio ρ for any given RIS phase shift $\boldsymbol{\phi}$ and active precoder $\boldsymbol{b}_{\mathrm{I/P},n}$, $\forall n$. On top of (3.27), the equivalent channel strength at subband n is $\|\boldsymbol{h}_n\|$. Hence, the rate (3.7) reduces to

$$R(\boldsymbol{s}_{\mathrm{I}}, \rho) = \log_2 \prod_{n=1}^{N} \left(1 + \frac{(1-\rho)\|\boldsymbol{h}_n\|^2 s_{\mathrm{I},n}^2}{\sigma_n^2} \right), \tag{3.28}$$

and the DC (3.9) rewrites as (3.29), so that problem (3.15) boils down to

$$\max_{\boldsymbol{s}_{\mathrm{I}}, \boldsymbol{s}_{\mathrm{P}}, \rho} \quad z(\boldsymbol{s}_{\mathrm{I}}, \boldsymbol{s}_{\mathrm{P}}, \rho) \tag{3.30a}$$

$$\text{s.t.} \quad R(\boldsymbol{s}_{\mathrm{I}}, \rho) \geq \bar{R}, \tag{3.30b}$$

$$\frac{1}{2}\left(\|\boldsymbol{s}_{\mathrm{I}}\|^2 + \|\boldsymbol{s}_{\mathrm{P}}\|^2\right) \leq P. \tag{3.30c}$$

$$z(\boldsymbol{s}_{\mathrm{I}}, \boldsymbol{s}_{\mathrm{P}}, \rho) = \frac{1}{2}\beta_2\rho \sum_{n=1}^{N}\|\boldsymbol{h}_n\|^2(s_{\mathrm{I},n}^2 + s_{\mathrm{P},n}^2) + \frac{3}{8}\beta_4\rho^2 \left(2\sum_{n_1,n_2}\prod_{j=1}^{2}\|\boldsymbol{h}_{n_j}\|^2 s_{\mathrm{I},n_j}^2 + \sum_{\substack{n_1,n_2,n_3,n_4 \\ n_1+n_2=n_3+n_4}}\prod_{j=1}^{4}\|\boldsymbol{h}_{n_j}\| s_{\mathrm{P},n_j} \right)$$

$$+ \frac{3}{2}\beta_4\rho^2 \left(\sum_{n_1,n_2}\|\boldsymbol{h}_{n_1}\|^2\|\boldsymbol{h}_{n_2}\|^2 s_{\mathrm{I},n_1}^2 s_{\mathrm{P},n_2}^2 \right). \tag{3.29}$$

Following [16], we introduce auxiliary variables t'', $\bar{\rho}$ and transform problem (3.30) into a reversed GP

$$\min_{\boldsymbol{s}_{\mathrm{I}},\boldsymbol{s}_{\mathrm{P}},\rho,\bar{\rho},t''} \quad \frac{1}{t''} \tag{3.31a}$$

$$\text{s.t.} \quad \frac{t''}{z(\boldsymbol{s}_{\mathrm{I}},\boldsymbol{s}_{\mathrm{P}},\rho)} \leq 1, \tag{3.31b}$$

$$\frac{2^{\bar{R}}}{\prod_{n=1}^{N}\left(1+\bar{\rho}\|\boldsymbol{h}_n\|^2 s_{\mathrm{I},n}^2/\sigma_n^2\right)} \leq 1, \tag{3.31c}$$

$$\frac{1}{2}\left(\|\boldsymbol{s}_{\mathrm{I}}\|^2 + \|\boldsymbol{s}_{\mathrm{P}}\|^2\right) \leq P, \tag{3.31d}$$

$$\rho + \bar{\rho} \leq 1. \tag{3.31e}$$

It can be concluded that $\bar{\rho}^{\star} = 1 - \rho^{\star}$ as no power is wasted at the receiver. The denominators of (3.31c) and (3.31b) consist of posynomials [42] that can be decomposed as sums of monomials

$$1 + \frac{\bar{\rho}\|\boldsymbol{h}_n\|^2 s_{\mathrm{I},n}^2}{\sigma_n^2} \triangleq \sum_{m_{\mathrm{I},n}} g_{m_{\mathrm{I},n}}(s_{\mathrm{I},n},\bar{\rho}), \tag{3.32}$$

$$z(\boldsymbol{s}_{\mathrm{I}},\boldsymbol{s}_{\mathrm{P}},\rho) \triangleq \sum_{m_{\mathrm{P}}} g_{m_{\mathrm{P}}}(\boldsymbol{s}_{\mathrm{I}},\boldsymbol{s}_{\mathrm{P}},\rho). \tag{3.33}$$

We upper bound (3.32) and (3.33) by the Geomtric Mean (GM)-Arithmetic Mean (AM) inequality [43] and transform problem (3.31) to

$$\min_{\boldsymbol{s}_{\mathrm{I}},\boldsymbol{s}_{\mathrm{P}},\rho,\bar{\rho},t''} \quad \frac{1}{t''} \tag{3.34a}$$

$$\text{s.t.} \quad t'' \prod_{m_{\mathrm{P}}} \left(\frac{g_{m_{\mathrm{P}}}(\boldsymbol{s}_{\mathrm{I}},\boldsymbol{s}_{\mathrm{P}},\rho)}{\gamma_{m_{\mathrm{P}}}}\right)^{-\gamma_{m_{\mathrm{P}}}} \leq 1, \tag{3.34b}$$

$$2^{\bar{R}} \prod_{n} \prod_{m_{\mathrm{I},n}} \left(\frac{g_{m_{\mathrm{I},n}}(s_{\mathrm{I},n},\bar{\rho})}{\gamma_{m_{\mathrm{I},n}}}\right)^{-\gamma_{m_{\mathrm{I},n}}} \leq 1, \tag{3.34c}$$

$$\frac{1}{2}\left(\|\boldsymbol{s}_{\mathrm{I}}\|^2 + \|\boldsymbol{s}_{\mathrm{P}}\|^2\right) \leq P, \tag{3.34d}$$

$$\rho + \bar{\rho} \leq 1, \tag{3.34e}$$

Algorithm 2 GP: Waveform Amplitude and Splitting Ratio.

1: **Input** β_2, β_4, $\boldsymbol{h}_n$, P, σ_n, $\bar{R}$, ϵ, $\forall n$
2: **Initialize** $i \leftarrow 0$, $\boldsymbol{s}_{\mathrm{I/P}}^{(0)}$, $\rho^{(0)}$
3: Compute $R^{(0)}$, $z^{(0)}$ by (3.28), (3.29)
4: Set $g_{m_{\mathrm{I},n}}^{(0)}$, $g_{m_\mathrm{P}}^{(0)}$, $\forall n$ by (3.32), (3.33)
5: **Repeat**
6:     $i \leftarrow i + 1$
7:     Update $\gamma_{m_{\mathrm{I},n}}^{(i)}$, $\gamma_{m_\mathrm{P}}^{(i)}$, $\forall n$ by (3.35), (3.36)
8:     Get $\boldsymbol{s}_{\mathrm{I/P}}^{(i)}$, $\rho^{(i)}$ by solving problem (3.34)
9:     Compute $R^{(i)}$, $z^{(i)}$ by (3.28), (3.29)
10:     Update $g_{m_{\mathrm{I},n}}^{(i)}$, $g_{m_\mathrm{P}}^{(i)}$, $\forall n$ by (3.32), (3.33)
11: **Until** $|z^{(i)} - z^{(i-1)}| \leq \epsilon$
12: Set $\boldsymbol{s}_{\mathrm{I/P}}^\star \leftarrow \boldsymbol{s}_{\mathrm{I/P}}^{(i)}$, $\rho^\star \leftarrow \rho^{(i)}$
13: **Output** $\boldsymbol{s}_{\mathrm{I}}^\star$, $\boldsymbol{s}_{\mathrm{P}}^\star$, $\rho^\star$

---

where $\gamma_{m_{\mathrm{I},n}}, \gamma_{m_\mathrm{P}} \geq 0$ and $\sum_{m_{\mathrm{I},n}} \gamma_{m_{\mathrm{I},n}} = \sum_{m_\mathrm{P}} \gamma_{m_\mathrm{P}} = 1$. The tightness of the AM-GM inequality depends on $\{\gamma_{m_{\mathrm{I},n}}, \gamma_{m_\mathrm{P}}\}$, and a feasible choice at iteration i is

$$\gamma_{m_{\mathrm{I},n}}^{(i)} = \frac{g_{m_{\mathrm{I},n}}\big(s_{\mathrm{I},n}^{(i-1)}, \bar{\rho}^{(i-1)}\big)}{1 + \bar{\rho}^{(i-1)}\|\boldsymbol{h}_n\|^2 (s_{\mathrm{I},n}^{(i-1)})^2 / \sigma_n^2}, \tag{3.35}$$

$$\gamma_{m_\mathrm{P}}^{(i)} = \frac{g_{m_\mathrm{P}}\big(\boldsymbol{s}_{\mathrm{I}}^{(i-1)}, \boldsymbol{s}_{\mathrm{P}}^{(i-1)}, \rho^{(i-1)}\big)}{z\big(\boldsymbol{s}_{\mathrm{I}}^{(i-1)}, \boldsymbol{s}_{\mathrm{P}}^{(i-1)}, \rho^{(i-1)}\big)}. \tag{3.36}$$

With (3.35) and (3.36), problem (3.34) can be solved by existing optimization tools such as `CVX toolbox` [41]. We update $\boldsymbol{s}_{\mathrm{I}}^{(i)}, \boldsymbol{s}_{\mathrm{P}}^{(i)}, \rho^{(i)}$ iteratively until convergence. The joint waveform amplitude and splitting ratio design is summarized in the GP Algorithm 2, which achieves local optimality at the cost of exponential computational complexity [43].

Proposition 4. *For any feasible initial point, the GP Algorithm 2 is guaranteed to converge to local optimal points of the waveform amplitude and splitting ratio design problem* (3.30)*.*

Proof. Please refer to [10, 16]. □

3.3.4   Low-Complexity Adaptive Design

To facilitate practical SWIPT implementation, we propose two closed-form adaptive waveform amplitude schemes by combining WF and SMF in time and power domains, respectively. For

WIT, the optimal WF strategy assigns the amplitude of modulated tone n by

$$s_{\mathrm{I},n} = \sqrt{2\left(\lambda - \frac{\sigma_n^2}{P\|\boldsymbol{h}_n\|^2}\right)^+}, \tag{3.37}$$

where λ is chosen to satisfy the power constraint $\|\boldsymbol{s}_I\|^2/2 \leq P$. The closed-form solution can be obtained by iterative power allocation [44], and the details are omitted here. On the other hand, SMF was proposed in [14] as a suboptimal WPT resource allocation scheme that assigns the amplitude of sinewave n by

$$s_{\mathrm{P},n} = \sqrt{\frac{2P}{\sum_{n=1}^N \|\boldsymbol{h}_n\|^{2\alpha}}} \|\boldsymbol{h}_n\|^\alpha, \tag{3.38}$$

where the scaling ratio $\alpha \geq 1$ is predetermined to exploit the rectifier nonlinearity and frequency selectivity. When the receiver works in TS mode, there is no superposition in the suboptimal waveform design (modulated waveform with amplitude (3.37) is used in the data session while multisine waveform with amplitude (3.38) is used in the energy session). When the receiver works in PS mode, we jointly design the combining ratio δ with the splitting ratio ρ, and assign the superposed waveform amplitudes as

$$s_{\mathrm{I},n} = \sqrt{2(1-\delta)\left(\lambda - \frac{\sigma_n^2}{P\|\boldsymbol{h}_n\|^2}\right)^+}, \tag{3.39}$$

$$s_{\mathrm{P},n} = \sqrt{\frac{2\delta P}{\sum_{n=1}^N \|\boldsymbol{h}_n\|^{2\alpha}}} \|\boldsymbol{h}_n\|^\alpha, \tag{3.40}$$

where the δ determines the power ratio of multisine waveform at the transmitter, and ρ determines the power ratio of the energy harvester at the receiver.[5]

Besides, minor modifications are required for passive beamforming to accommodate the low-complexity waveform schemes. Specifically, the rate constraint (3.25b) should be dropped as the achievable rate is controlled by η or $\{\delta, \rho\}$. To achieve the WIT point ($\rho = 0$), the rate (3.18) should be maximized, the current expression (3.24) is not needed and no SCA is involved. The Modified-SCA (M-SCA) Algorithm 3 summarizes the modified passive beamforming design when the receiver works in PS mode. Similarly, no loss is introduced by SDR and local optimality is guaranteed. The proofs are omitted here. Since each SDP involves $(L+1)$ linear constraints, the computational complexity of Algorithm 3

---

[5]We notice that $\delta^\star = \rho^\star = 0$ at the WIT point and $\delta^\star = \rho^\star = 1$ at the WPT point when N is relatively large. Intuitively, $\delta^\star$ and $\rho^\star$ should be positively correlated for efficient SWIPT design.

Algorithm 3 M-SCA: RIS Phase Shift.

1: **Input** β_2, β_4, $\boldsymbol{h}_{\mathrm{D},n}$, $\boldsymbol{V}_n$, σ_n, $\boldsymbol{w}_{\mathrm{I/P},n}$, ρ, ϵ, $\forall n$
2: Construct $\boldsymbol{V}$, $\boldsymbol{M}$, $\boldsymbol{M}_n$, $\boldsymbol{C}_n$, $\boldsymbol{C}_{\mathrm{I/P},k}$, $\forall n, k$
3: **Initialize** $i \leftarrow 0$, $\boldsymbol{\Phi}^{(0)}$
4: **If** $\rho = 0$
5:     Get $\boldsymbol{\Phi}^{\star}$ by maximizing (3.18) s.t. (3.25c), (3.25d)
6: **Else**
7:     Set $t_{\mathrm{I/P},k}^{(0)}$, $\forall k$ by (3.17)
8:     Compute $z^{(0)}$ by (3.19)
9:     **Repeat**
10:         $i \leftarrow i + 1$
11:         Get $\boldsymbol{\Phi}^{(i)}$ by maximizing (3.24) s.t. (3.25c), (3.25d)
12:         Update $t_{\mathrm{I/P},k}^{(i)}$, $\forall k$ by (3.17)
13:         Compute $z^{(i)}$ by (3.19)
14:     **Until** $|z^{(i)} - z^{(i-1)}| \leq \epsilon$
15:     Set $\boldsymbol{\Phi}^{\star} \leftarrow \boldsymbol{\Phi}^{(i)}$
16: **End If**
17: Get $\hat{\boldsymbol{\phi}}^{\star}$ by eigen decomposition, $\boldsymbol{\Phi}^{\star} = \hat{\boldsymbol{\phi}}^{\star}(\hat{\boldsymbol{\phi}}^{\star})^H$
18: Set $\boldsymbol{\phi}^{\star} \leftarrow e^{j \arg\left([\hat{\boldsymbol{\phi}}^{\star}]_{(1:L)} / [\hat{\boldsymbol{\phi}}^{\star}]_{(L+1)}\right)}$
19: **Output** $\boldsymbol{\phi}^{\star}$

---

is $\mathcal{O}\left(I_{\mathrm{M-SCA}}(L+1)^{4.5} \log(\epsilon_{\mathrm{IPM}}^{-1})\right)$, where $I_{\mathrm{M-SCA}}$ denotes the number of M-SCA iterations [40]. Note that no SCA is involved at the WIT point where $I_{\mathrm{M-SCA}} = 1$.

3.3.5 Block Coordinate Descent

Based on the direct and cascaded CSIT, we iteratively update the passive beamforming $\boldsymbol{\phi}$ by Algorithm 1, the active precoder $\boldsymbol{b}_{\mathrm{I/P},n}$, $\forall n$ by equation (3.27), and the waveform amplitude $\boldsymbol{s}_{\mathrm{I/P}}$ and splitting ratio ρ by Algorithm 2, until convergence. The steps are summarized in the BCD Algorithm 4, whose computational complexity is exponential as inherited from Algorithm 2. It is guaranteed to converge, but may end up with a suboptimal solution because variables are coupled in constraint (3.15b) [45].

For the low-complexity design under PS mode, we obtain the phase shift by Algorithm 3, the active precoder $\boldsymbol{b}_{\mathrm{I/P},n}$, $\forall n$ by equation (3.27), and the waveform amplitude by (3.39) and (3.40). To achieve the WIT point ($\rho = 0$), the rate (3.18) should be maximized to obtain the maximum capacity $C_{\max}$.[6] Note that the BCD algorithm obtains the R-E region by varying the rate constraint from 0 to $C_{\max}$, while the achievable R-E region of the Low-Complexity (LC)-BCD algorithm can be obtained by performing a two-dimensional search over (δ, ρ) from

---

[6]Recall in Remark 2 that different subchannel designs lead to different capacities.

Algorithm 4 BCD: Waveform, Beamforming and Splitting Ratio.

1: **Input** β_2, β_4, $\boldsymbol{h}_{\mathrm{D},n}$, $\boldsymbol{V}_n$, P, σ_n, $\bar{R}$, ϵ, $\forall n$
2: **Initialize** $i \leftarrow 0$, $\boldsymbol{\phi}^{(0)}$, $\boldsymbol{b}_{\mathrm{I/P},n}^{(0)}$, $\boldsymbol{s}_{\mathrm{I/P}}^{(0)}$, $\rho^{(0)}$, $\forall n$
3: Set $\boldsymbol{w}_{\mathrm{I/P},n}^{(0)}$, $\forall n$ by (3.26)
4: Compute $z^{(0)}$ by (3.29)
5: **Repeat**
6:      $i \leftarrow i + 1$
7:      Get $\boldsymbol{\phi}^{(i)}$ based on $\boldsymbol{w}_{\mathrm{I/P}}^{(i-1)}$, $\rho^{(i-1)}$ by Algorithm 1
8:      Update $\boldsymbol{h}_n^{(i)}$, $\boldsymbol{b}_n^{(i)}$, $\forall n$ by (3.5), (3.27)
9:      Get $\boldsymbol{s}_{\mathrm{I/P}}^{(i)}$, $\rho^{(i)}$ by Algorithm 2
10:     Update $\boldsymbol{w}_{\mathrm{I/P},n}^{(i)}$, $\forall n$ by (3.26)
11:     Compute $z^{(i)}$ by (3.29)
12: **Until** $\left| z^{(i)} - z^{(i-1)} \right| \leq \epsilon$
13: Set $\boldsymbol{\phi}^{\star} \leftarrow \boldsymbol{\phi}^{(i)}$, $\boldsymbol{w}_{\mathrm{I/P}}^{\star} \leftarrow \boldsymbol{w}_{\mathrm{I/P}}^{(i)}$, $\rho^{\star} \leftarrow \rho^{(i)}$
14: **Output** $\boldsymbol{\phi}^{\star}$, $\boldsymbol{w}_{\mathrm{I}}^{\star}$, $\boldsymbol{w}_{\mathrm{P}}^{\star}$, $\rho^{\star}$
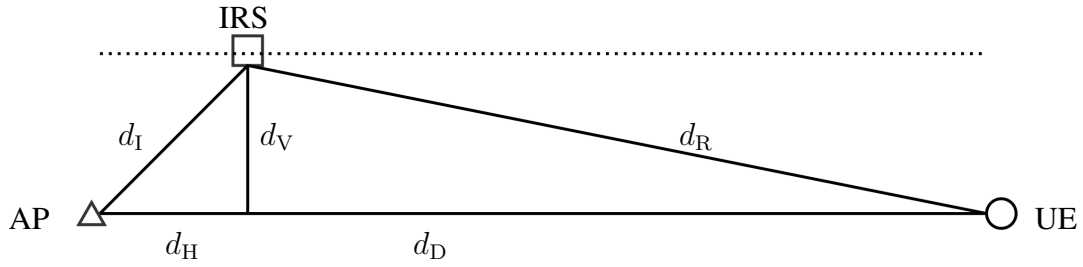
Fig. 3.5 System layout in simulation.

$(0,0)$ to $(1,1)$. The steps are summarized in Algorithm 5. The computational complexity of Algorithm 5 is $\mathcal{O}\left(I_{\mathrm{LC-BCD}} I_{\mathrm{M-SCA}} (L+1)^{4.5} \log(\epsilon_{\mathrm{IPM}}^{-1}) \right)$, where $I_{\mathrm{LC-BCD}}$ denotes the number of LC-BCD iterations [40].

3.4   Performance Evaluations

To evaluate the proposed RIS-aided SWIPT system, we consider the layout in Fig. 3.5 where the RIS moves along a line parallel to the AP-UE path. Let d_{H}, d_{V} be the horizontal and vertical distances from the AP to the RIS, and denote respectively d_{D}, $d_{\mathrm{I}} = \sqrt{d_{\mathrm{H}}^2 + d_{\mathrm{V}}^2}$, $d_{\mathrm{R}} = \sqrt{(d_{\mathrm{D}} - d_{\mathrm{H}})^2 + d_{\mathrm{V}}^2}$ as the distance of direct, incident and reflected links. $d_{\mathrm{D}} = 12\,\mathrm{m}$ and $d_{\mathrm{H}} = d_{\mathrm{V}} = 2\,\mathrm{m}$ are chosen as reference. The path loss of direct, incident and reflected links are denoted by Λ_{D}, Λ_{I} and Λ_{R}, respectively. We consider a large open space Wi-Fi-like environment at center frequency $2.4\,\mathrm{GHz}$ where the channel follows IEEE TGn channel

---

Algorithm 5 LC-BCD: Waveform and Beamforming.

1: **Input** β_2, β_4, $\boldsymbol{h}_{\mathrm{D},n}$, $\boldsymbol{V}_n$, P, σ_n, δ, ρ, ϵ, $\forall n$
2: **Initialize** $i \leftarrow 0$, $\boldsymbol{\phi}^{(0)}$, $\boldsymbol{b}_{\mathrm{I/P},n}^{(0)}$, $\boldsymbol{s}_{\mathrm{I/P}}^{(0)}$, $\forall n$
3: Set $\boldsymbol{w}_{\mathrm{I/P},n}^{(0)}$, $\forall n$ by (3.26)
4: Compute $R^{(0)}$, $z^{(0)}$ by (3.28), (3.29)
5: **Repeat**
6:     $i \leftarrow i + 1$
7:     Get $\boldsymbol{\phi}^{(i)}$ based on $\boldsymbol{w}_{\mathrm{I/P}}^{(i-1)}$ by Algorithm 3
8:     Update $\boldsymbol{h}_n^{(i)}$, $\boldsymbol{b}_n^{(i)}$, $\forall n$ by (3.5), (3.27)
9:     Update $\boldsymbol{s}_{\mathrm{I}}^{(i)}$, $\boldsymbol{s}_{\mathrm{P}}^{(i)}$ by (3.39), (3.40)
10:     Update $\boldsymbol{w}_{\mathrm{I/P},n}^{(i)}$, $\forall n$ by (3.26)
11:     Compute $R^{(i)}$, $z^{(i)}$ by (3.28), (3.29)
12:     **If** $\rho = 0$
13:         $\Delta \leftarrow R^{(i)} - R^{(i-1)}$
14:     **Else**
15:         $\Delta \leftarrow z^{(i)} - z^{(i-1)}$
16:     **End If**
17: **Until** $|\Delta| \leq \epsilon$
18: Set $\boldsymbol{\phi}^{\star} \leftarrow \boldsymbol{\phi}^{(i)}$, $\boldsymbol{w}_{\mathrm{I/P}}^{\star} \leftarrow \boldsymbol{w}_{\mathrm{I/P}}^{(i)}$
19: **Output** $\boldsymbol{\phi}^{\star}$, $\boldsymbol{w}_{\mathrm{I}}^{\star}$, $\boldsymbol{w}_{\mathrm{P}}^{\star}$

---

model D [46]. Specifically, the path loss exponent is 2 (i.e., free-space model) up to $10\,\mathrm{m}$, and 3.5 onwards to further penalize the channels with large distance. All fadings are modeled as Non-Line-of-Sight (NLoS) with tap delays and powers specified in model D, and the tap gains are modeled as i.i.d. CSCG variables. Rectenna parameters are set to $k_2 = 0.0034$, $k_4 = 0.3829$, $R_{\mathrm{A}} = 50\,\Omega$ [10] such that $\beta_2 = 0.17$ and $\beta_4 = 957.25$. We also choose the average Effective Isotropic Radiated Power (EIRP) as $P = 40\,\mathrm{dBm}$, the receive antenna gain as $3\,\mathrm{dBi}$, the scaling ratio as $\alpha = 2$, and the tolerance as $\epsilon = 10^{-8}$. To further reduce the complexity, we assume $\delta = \rho$ for simplicity and perform a one-dimensional search from 0 to 1 to obtain a inner R-E bound for the LC-BCD algorithm. Each R-E point is averaged over 200 channel realizations, and the x-axis is normalized to per-subband rate R/N.

Fig. 3.6 reveals how RIS influences the sorted equivalent subchannel amplitude for one channel realization. Due to the flexible subchannel design enabled by passive beamforming, the optimal amplitude distribution for WIT and WPT are dissimilar. Under the specified configuration, the WPT-optimized RIS aligns the strong subbands to exploit the rectifier nonlinearity. On the other hand, the WIT-optimized RIS provides a fair gain over all subchannels when L is sufficiently large. This is reminiscent of the WF scheme at high SNR, but is realized by channel alignment instead of resource allocation. Nevertheless, the
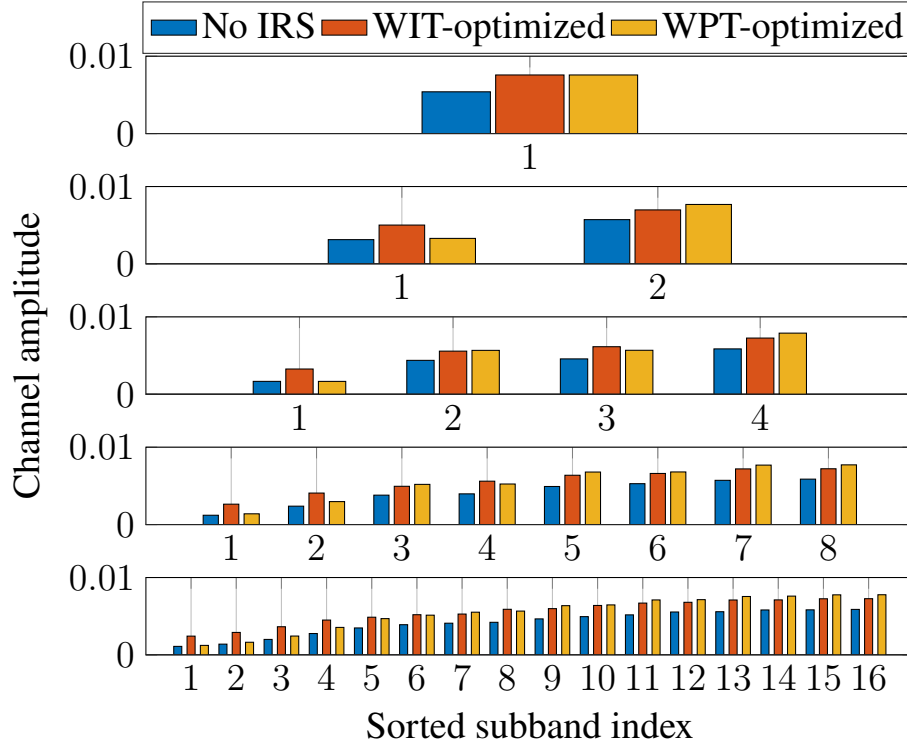
Fig. 3.6 Sorted equivalent subchannel amplitude with and without RIS versus N for $M = 1$, $L = 100$, $\sigma_n^2 = -40\,\mathrm{dBm}$, $B = 10\,\mathrm{MHz}$ and $d_\mathrm{H} = d_\mathrm{V} = 2\,\mathrm{m}$.

amplitude of modulated and multisine waveforms remains approximately unchanged when adding a RIS (the plots are not attached). In other words, RIS has a subtle impact on the waveform design.

Fig. 3.7(a) illustrates the average R-E region versus the number of subband N. First, it is observed that increasing N reduces the per-subband rate but boosts the harvested energy. This is because less power is allocated to each subband but more balanced DC terms are introduced by frequency coupling to boost the harvested energy. On the other hand, Fig. 3.7(b) presents the sorted modulated/multisine amplitude $s_\mathrm{I/P}$ for WPT. It demonstrates that a dedicated multisine waveform is unnecessary for a small N but is required for a large N. This observation origins from the rectifier nonlinearity. Although both waveforms have equivalent second-order DC terms (3.10) and (3.12), for the fourth-order terms (3.11) and (3.13), the modulated waveform has N^2 monomials with a modulation gain of 2, while the multisine has $(2N^3 + N)/3$ monomials as the components of different frequencies compensate and produce DC. Second, the R-E region is convex for $N \in \{2, 4\}$ and concave-convex for $N \in \{8, 16\}$, such that PS outperforms TS for a small N and is outperformed for a large N. When N is in between, the optimal strategy is a combination of both, i.e., a time sharing between the WPT point and the saddle PS SWIPT point (as denoted by the red curve in Fig. 3.7(a)). When

(a) R-E region

(b) WPT waveform amplitude
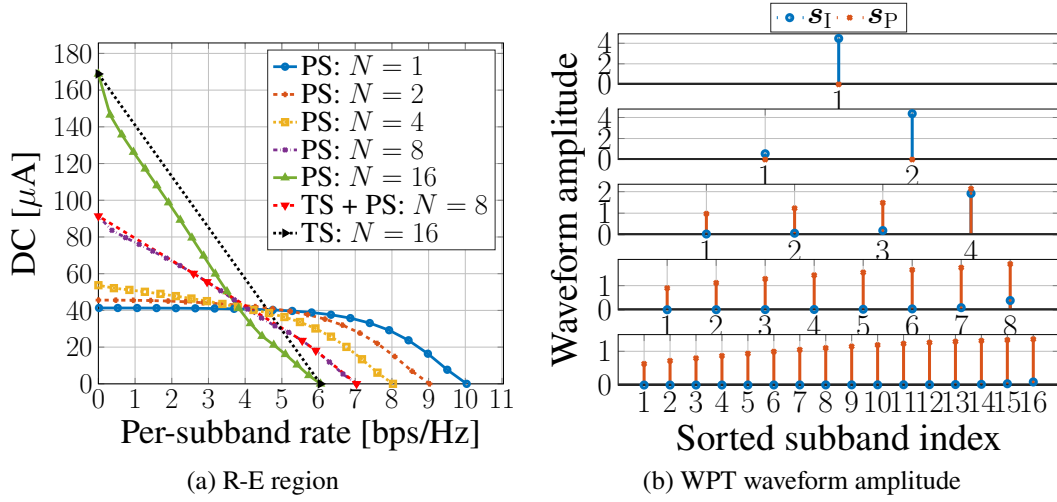
Fig. 3.7 Average R-E region and WPT waveform amplitude versus N for $M = 1$, $L = 20$, $\sigma_n^2 = -40\,\mathrm{dBm}$, $B = 1\,\mathrm{MHz}$ and $d_{\mathrm{H}} = d_{\mathrm{V}} = 2\,\mathrm{m}$.

(a) R-E region
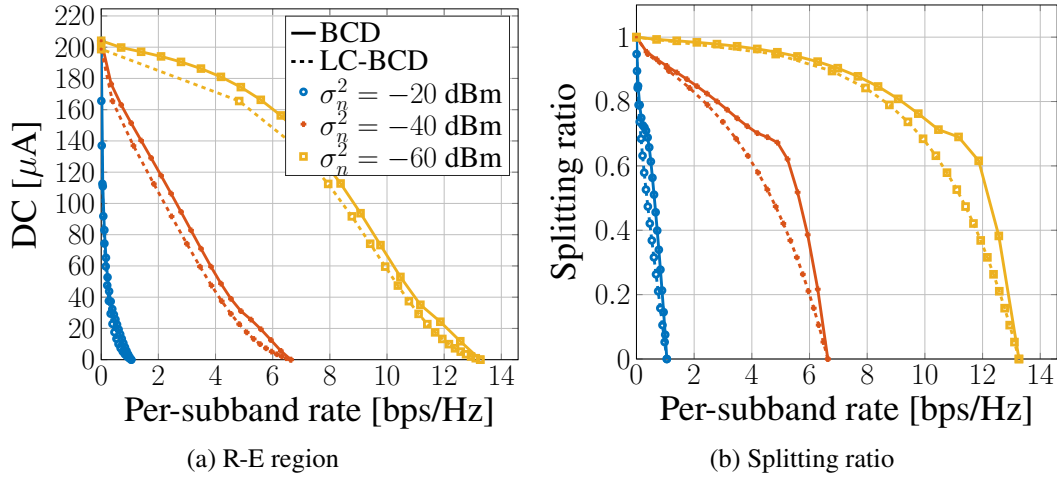
(b) Splitting ratio

Fig. 3.8 Average R-E region and splitting ratio versus σ_n^2 for $M = 1$, $N = 16$, $L = 20$, $B = 1\,\mathrm{MHz}$ and $d_{\mathrm{H}} = d_{\mathrm{V}} = 2\,\mathrm{m}$.

N is relatively small, only modulated waveform is used at both WIT and WPT points, and one can infer that no multisine waveform is needed for the entire R-E region. It aligns with the conclusion based on the conventional linear harvester model, namely the R-E region is convex, PS outperforms TS, and dedicated power waveform is unnecessary. As N becomes sufficiently large, the multisine waveform further boosts WPT and creates some concavity in the high-power region, which accounts for the superiority of TS under the nonlinear harvester model. Therefore, we conclude that the rectifier nonlinearity enlarges the R-E region by favoring a different waveform and receiving mode, both heavily depending on N.

(a) R-E region   (b) Path loss product
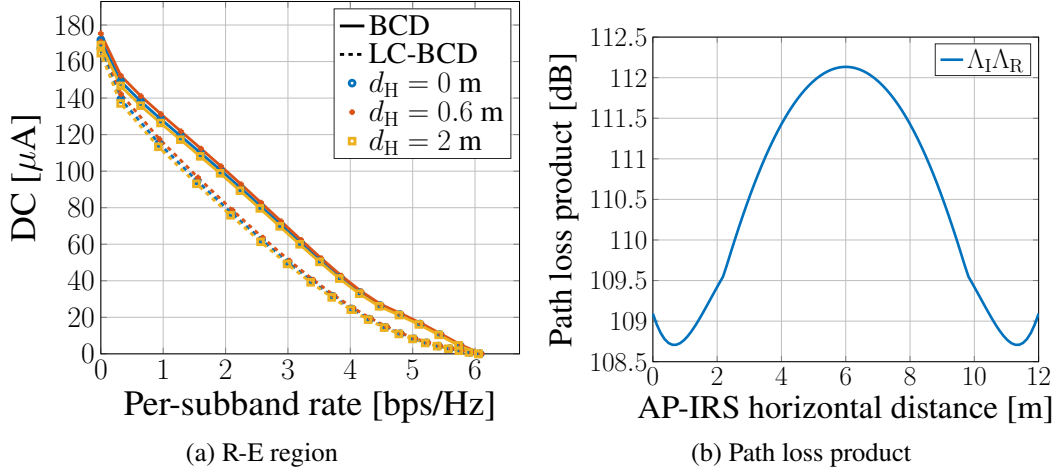
Fig. 3.9 Average R-E region and path loss versus d_H for $M = 1$, $N = 16$, $L = 20$, $\sigma_n^2 = -40\,\mathrm{dBm}$, $B = 1\,\mathrm{MHz}$ and $d_V = 2\,\mathrm{m}$.

The average noise power influences the R-E region as shown in Fig. 3.8(a). First, we note that the R-E region is roughly concave/convex at low/high SNR such that TS/PS are preferred correspondingly. At low SNR, the power is allocated to the modulated waveform on a few strongest subbands to achieve a high rate. As the rate constraint $\bar{R}$ decreases, Algorithm 2 activates more subbands that further boosts the harvested DC power because of frequency coupling and harvester nonlinearity. Second, there exists a turning point in the R-E region, especially for a low noise level ($\sigma_n^2 \leq -40\,\mathrm{dBm}$). The reason is that when $\bar{R}$ departs slightly from the maximum value, the algorithm tends to adjust the splitting ratio ρ rather than allocate more power to the multisine waveform, since a small amplitude multisine could be inefficient for energy purpose. As $\bar{R}$ further decreases, thanks to the advantage of multisine, a superposed waveform with a small ρ can outperform a modulated waveform with a large ρ. The result proves the benefit of superposed waveform and the necessity of joint waveform and splitting ratio optimization. Besides, the LC-BCD algorithm achieves a good balance between performance and complexity even if one-dimensional search is considered for $\delta = \rho$ from 0 to 1.

In Fig. 3.9(a), we compare the average R-E region achieved by different AP-RIS horizontal distance d_H. Different from the active Amplify-and-Forward (AF) relay that favors midpoint development [47], the RIS should be placed close to either the AP or the UE based on the product path loss model that applies to finite-size element reflection [48, 49]. Moreover, there exist two optimal RIS coordinates around $d_H = 0.6$ and $11.4\,\mathrm{m}$ that minimize the path loss product $\Lambda_I\Lambda_R$ and maximize the R-E tradeoff. It suggests that equipping the AP with a RIS can potentially extend the operation range of SWIPT systems.

(a) R-E region
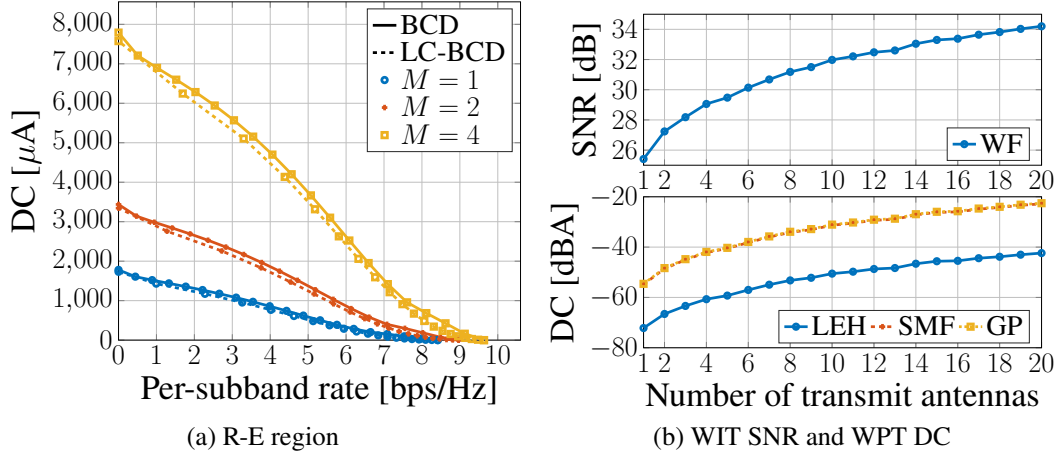
(b) WIT SNR and WPT DC

Fig. 3.10 Average R-E region, WIT SNR and WPT DC versus M for $N = 16$, $L = 20$, $\sigma_n^2 = -40\,\mathrm{dBm}$, $B = 1\,\mathrm{MHz}$, $d_\mathrm{H} = d_\mathrm{V} = 0.2\,\mathrm{m}$.

(a) R-E region
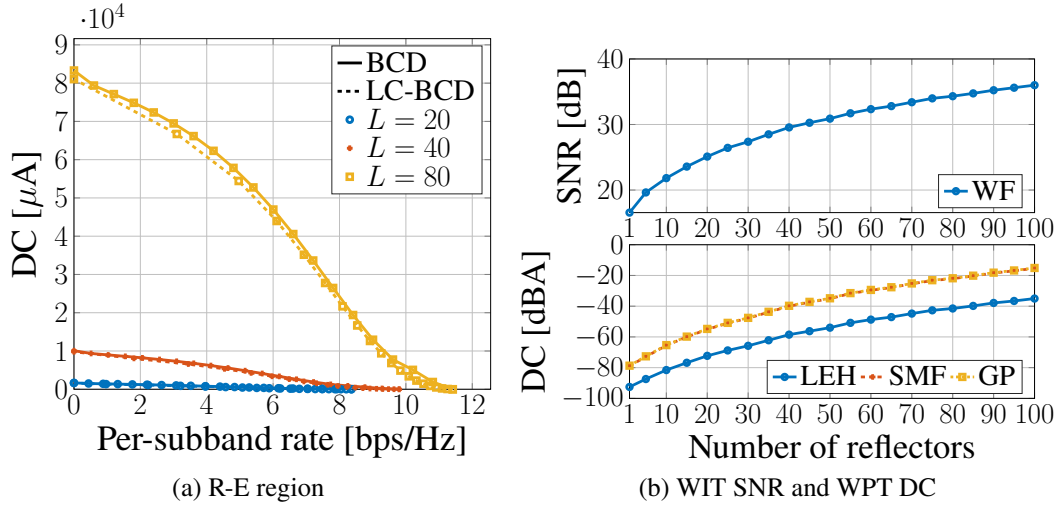
(b) WIT SNR and WPT DC

Fig. 3.11 Average R-E region, WIT SNR and WPT DC versus L for $M = 1$, $N = 16$, $\sigma_n^2 = -40\,\mathrm{dBm}$, $B = 1\,\mathrm{MHz}$ and $d_\mathrm{H} = d_\mathrm{V} = 0.2\,\mathrm{m}$.

The impacts of the number of transmit antennas M and the RIS elements L on the R-E behavior are revealed in Figs. 3.10(a) and 3.11(a). First, it is observed that adding either active or passive elements can improve the equivalent SNR, which produces a nearly concave R-E region and favors the PS receiver. Second, the conventional Linear Energy Harvester (LEH) model leads to a power-inefficient design. To investigate the performance loss, we truncate the DC objective function (3.8) at $n_0 = 2$ such that (i) in the passive beamforming problem, $z(\boldsymbol{\Phi}) = \beta_2 \rho (t_{\mathrm{I},0} + t_{\mathrm{P},0})/2$ and no SCA is required; (ii) in the waveform design problem, the WPT-optimal strategy is the adaptive single sinewave that allocates all power to the multisine at the strongest subband [10]. As shown in Figs. 3.10(b) and 3.11(b), those

conventional designs do not exploit the harvester nonlinearity and end up with a nearly $20\,\mathrm{dBA}$ gap compared to the nonlinear model-based SMF and GP designs. Third, doubling M brings a $3\,\mathrm{dB}$ gain at the output SNR and a $12\,\mathrm{dBA}$ increase at the harvested DC, which verified that active beamforming has an array gain of M [44] with power scaling order M^2 under the truncated nonlinear harvester model [10, 16]. Fourth, when the RIS is very close to the AP or UE, doubling L can bring a $6\,\mathrm{dB}$ gain at the output SNR and a $24\,\mathrm{dBA}$ increase at the harvested DC. From the perspective of WIT, it suggests that passive beamforming can reach an array gain of L^2, as indicated by [25]. An interpretation is that the RIS coherently combines the incoming signal with a receive array gain L, then performs an equal gain reflection with a transmit array gain L. From the perspective of WPT, it suggests that passive beamforming comes with a power scaling order L^4 under the truncated nonlinear harvester model. We then verify this novel observation in a simplified case where the power is uniformly allocated over multisine, all channels are frequency-flat, and L is sufficiently large such that the direct channel becomes negligible. Let X be the cascaded small-scale fading coefficient. The DC in such case reduces to

$$z = \beta_2 \Lambda_\mathrm{R}^2 \Lambda_\mathrm{I}^2 |X|^2 L^2 P + \beta_4 \frac{2N^2 + 1}{2N} \Lambda_\mathrm{R}^4 \Lambda_\mathrm{I}^4 |X|^4 L^4 P^2, \tag{3.41}$$

which scales quartically with L. Compared with active antennas, RIS elements achieve higher array gain and power scaling order, but a very large L is required to compensate the double fading of the auxiliary link. These observations demonstrate the R-E benefit of passive beamforming and emphasize the importance of accounting for the harvester nonlinearity in the waveform and beamforming design.

Figs. 3.12(a) and 3.12(b) explore the R-E region with different RIS strategies for narrowband and broadband SWIPT. The ideal Frequency-Selective (FS) RIS assumes the reflection coefficient of each element is independent and controllable at different frequencies. The adaptive RIS adjusts the passive beamforming for different R-E points by Algorithm 1. The WIT/WPT-optimized RIS is retrieved by Algorithm 3 then fixed for the whole R-E region. The random RIS models the phase shift of all elements as i.i.d. uniform random variables over $[0, 2\pi)$. First, random RIS and no RIS perform worse than other schemes since no passive beamforming is exploited. Their R-E boundaries coincide as the antenna mode reflection of the random RIS is canceled out after averaging. Second, when the bandwidth is small, the performance of ideal, adaptive, and WIT/WPT-optimized RIS are similar; when the bandwidth is large, the adaptive RIS outperforms the WIT/WPT-optimized RIS but is outperformed by the ideal FS RIS. In the former case, the subband responses are close to each other such that the tradeoff in Remark 2 becomes insignificant, and the auxiliary link can be roughly maximized at all subbands. It suggests that for narrowband SWIPT, the

(a) $B = 1\,\mathrm{MHz}$

(b) $B = 10\,\mathrm{MHz}$
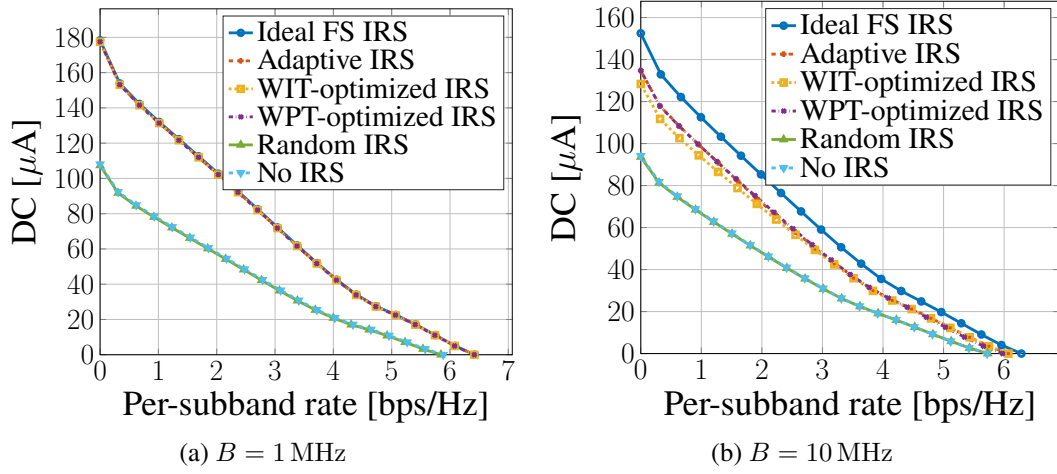
Fig. 3.12 Average R-E region for ideal, adaptive, fixed and no RIS versus B for $M = 1$, $N = 16$, $L = 20$, $\sigma_n^2 = -40\,\mathrm{dBm}$ and $d_{\mathrm{H}} = d_{\mathrm{V}} = 2\,\mathrm{m}$.

optimal passive beamforming for any R-E point is optimal for the whole R-E region, and the corresponding composite channel and active precoder are also optimal for the whole R-E region. Hence, the achievable R-E region is obtained by optimizing the waveform amplitude and splitting ratio. On the other hand, since the channel frequency selectivity affects the performance of the information decoder and energy harvester differently, the optimal RIS reflection coefficient varies at different R-E tradeoffs points for broadband SWIPT. As shown in Fig. 3.6, the subchannel amplification can be either spread evenly to improve the rate at high SNR, or focused on a few strongest subbands to boost the output DC, thanks to adaptive passive beamforming.

We then explore the impacts of imperfect cascaded CSIT and quantized RIS on the R-E performance. Due to the general lack of RF-chains at the RIS, it can be challenging to acquire accurate cascaded CSIT on a short-term basis. We assume the cascaded channel at subband n is

$$\boldsymbol{V}_n = \hat{\boldsymbol{V}}_n + \tilde{\boldsymbol{V}}_n, \tag{3.42}$$

where $\hat{\boldsymbol{V}}_n$ is the estimated cascaded CSIT and $\tilde{\boldsymbol{V}}_n$ is the estimation error with entries following i.i.d. CSCG distribution $\mathcal{CN}(0, \epsilon_n^2)$.[7] Figure 3.13(a) shows that the proposed passive beamforming Algorithm 1 is robust to cascaded CSIT inaccuracy for broadband SWIPT with different L. On the other hand, since the practical reflection coefficient depends on the available element impedances, we consider a discrete RIS codebook $\mathcal{C}_\phi = \{e^{j2\pi i/2^b} \mid i = 1, \ldots, 2^b\}$ and uniformly quantize the continuous reflection coefficients obtained by Algorithm 4 to

---

[7]Note that the subchannel responses are correlated but the estimations can be independent.

(a) Imperfect cascaded CSIT
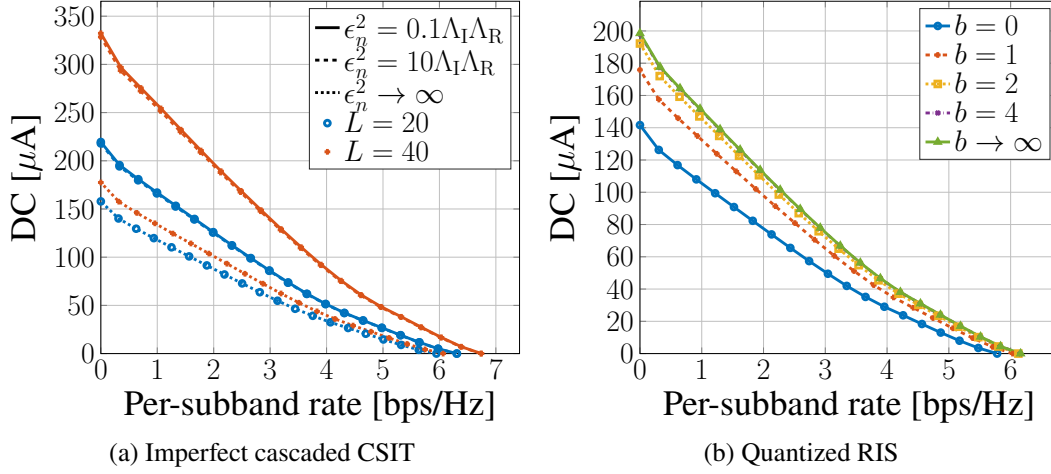
(b) Quantized RIS

Fig. 3.13 Average R-E region with imperfect cascaded CSIT and quantized RIS for $M = 1$, $N = 16$, $L = 20$, $\sigma_n^2 = -40\,\mathrm{dBm}$, $B = 10\,\mathrm{MHz}$ and $d_\mathrm{H} = d_\mathrm{V} = 2\,\mathrm{m}$. $\epsilon_n = 0$ and $\epsilon_n = \infty$ correspond respectively to perfect CSIT and no CSIT (and random RIS); $b = 0$ and $b \to \infty$ correspond respectively to no RIS and continuous RIS.

reduce the circuit complexity and control overhead.[8] Figure 3.13(b) suggests that even $b = 1$ (i.e., two-state reflection) brings considerable R-E gain over the benchmark scheme without RIS, and the performance gap between $b = 4$ and unquantized RIS is negligible. These observations demonstrate the advantage of the proposed joint waveform, active and passive beamforming design in practical RIS-aided SWIPT systems.

3.5   Conclusion and Future Works

This paper investigated the R-E tradeoff of a single user employing practical receiving strategies in a RIS-aided multi-carrier MISO SWIPT system. Uniquely, we considered the joint waveform, active and passive beamforming design under rectifier nonlinearity to maximize the achievable R-E region. A three-stage BCD algorithm was proposed to solve the problem. In the first stage, the RIS phase shift was obtained by the SCA technique and eigen decomposition. In the second and third stages, the active precoder was derived in closed form, and the waveform amplitude and splitting ratio were optimized by the GP method. We also proposed and combined closed-form adaptive waveform schemes with a modified passive beamforming strategy to formulate a low-complexity BCD algorithm that achieves a good balance between performance and complexity. Numerical results revealed

---

[8]This relax-then-quantize approach can bring notable performance loss compared with direct optimization over the discrete phase shift set, especially for a small b (i.e., low-resolution RIS) [50].

significant R-E gains by modeling harvester nonlinearity in the RIS-aided SWIPT design. Unlike active antennas, RIS elements cannot be designed independently across frequencies, but can integrate coherent combining and equal gain transmission to enable constructive reflection and flexible subchannel design. Compared to the conventional no-RIS system, the RIS mainly affects the effective channel instead of the waveform design.

One particular unanswered question of this paper is how to design waveform, active and passive beamforming in a multi-user multi-carrier RIS-aided SWIPT system. Also, harvester saturation effect and practical RIS models with amplitude-phase coupling [26], angle-dependent reflection [49], frequency-dependent reflection, and/or partially/fully-connected architecture [51] could be considered in future works.

Chapter 4

RIScatter: Unifying BackCom and RIS

4.1 Introduction

Future wireless network is envisioned to provide high throughput, uniform coverage, pervasive connectivity, heterogeneous control, and cognitive intelligence for trillions of low-power devices. Backscatter Communication (BackCom) separates a transmitter into a RF carrier emitter with power-hungry elements (e.g., synthesizer and amplifier) and an information-bearing node with power-efficient components (e.g., harvester and modulator) [52]. The receiver (reader) can be either co-located or separated with the carrier emitter, known as Monostatic Backscatter Communication (MBC) and Bistatic Backscatter Communication (BBC) in Fig. 4.1(a) and 4.1(b), respectively. Relevant applications such as Radio-Frequency Identification (RFID) [53, 54] and passive sensor network [55, 56] have been extensively researched, standardized, and commercialized to embrace the Internet of Everything (IoE). However, conventional backscatter nodes only respond when externally inquired by a nearby reader. Ambient Backscatter Communication (AmBC) in Fig. 4.1(c) was proposed a decade ago where battery-free nodes recycle ambient signals (e.g., radio, television and Wi-Fi) to harvest energy and establish connections [57]. It does not require dedicated power source, carrier emitter, or frequency spectrum, but the backscatter decoding is subject to the strong interference from the primary (legacy) link. To tackle this, cooperative AmBC [58] employs a co-located receiver to decode both coexisting links, and the concept was further refined as Symbiotic Radio (SR) in Fig. 4.1(d) [59]. Specifically, the active transmitter generates RF wave carrying primary information, the passive node creates a rich-scattering environment and superimposes its own information, and the co-located receiver cooperatively decodes both links. In those BackCom applications, the scatter node is considered as an *information source* and the reflection pattern depends exclusively on the information symbol. On the other hand, RIS in Fig. 4.1(e) is a smart signal reflector with numerous passive elements

of adjustable phase shifts. It customizes the wireless environment for signal enhancement, interference suppression, scattering enrichment, and/or non-line-of-sight bypassing [60]. Each RIS element is considered as a *channel shaper* and the reflection pattern depends exclusively on the Channel State Information (CSI).

As a special case of Cognitive Radio (CR), active and passive transmissions coexist and interplay in AmBC and SR. Such a coexistence is classified into commensal (overlay), parasitic (underlay), and competitive (interfering) paradigms, and their achievable rate and outage performance were investigated in [61, 62]. The achievable rate and optimal input distribution for binary-input AmBC were investigated in [63], but its impact on the primary link was omitted. In [64], the authors analyzed the energy efficiency and achievable rate region for an AmBC-aided multi-user downlink Non-Orthogonal Multiple Access (NOMA) system. However, they assumed equal symbol duration and perfect synchronization for the coexisting links. Importantly, active-passive coexisting networks have three special and important properties:

1. Primary and backscatter symbols are superimposed by *double modulation* (i.e., multiplication coding);

2. Backscatter signal strength is much weaker than primary due to *double fading*;

3. The spreading factor (i.e., backscatter symbol duration over primary) is usually large[1].

The second property motivated [66, 59, 61, 62, 64, 67–70, 58, 71–73] to view SR as a multiplicative NOMA and perform Successive Interference Cancellation (SIC) from primary to backscatter link. During primary decoding, the backscatter signal can be modelled as channel uncertainty or multiplicative interference, when the spreading factor is large or small. Decoding each backscatter symbol also requires multiple SIC followed by a Maximal Ratio Combining (MRC) over primary blocks, which is operation-intensive and CSI-sensitive. Under those assumptions, the achievable rate region of cell-free SR was characterized in [73]. When the spreading factor is sufficiently large, the primary achievable rate under semi-coherent detection[2] asymptotically approaches its coherent counterpart such that both links are approximately interference-free [66]. However, this assumption severely limits the backscatter throughput.

On the other hand, static RIS that employs fixed reflection pattern per channel block has been extensively studied in wireless communication, sensing, and power literature [23, 74–78].

---

[1]The load-switching interval of low-power backscatter modulators is usually 0.1 to $10\,\mu s$ [65], accounting for a typical spreading factor between 10 and 10^3.

[2]In this paper, semi-coherent detection refers to the primary/backscatter decoding with known CSI and unknown backscatter/primary symbols.
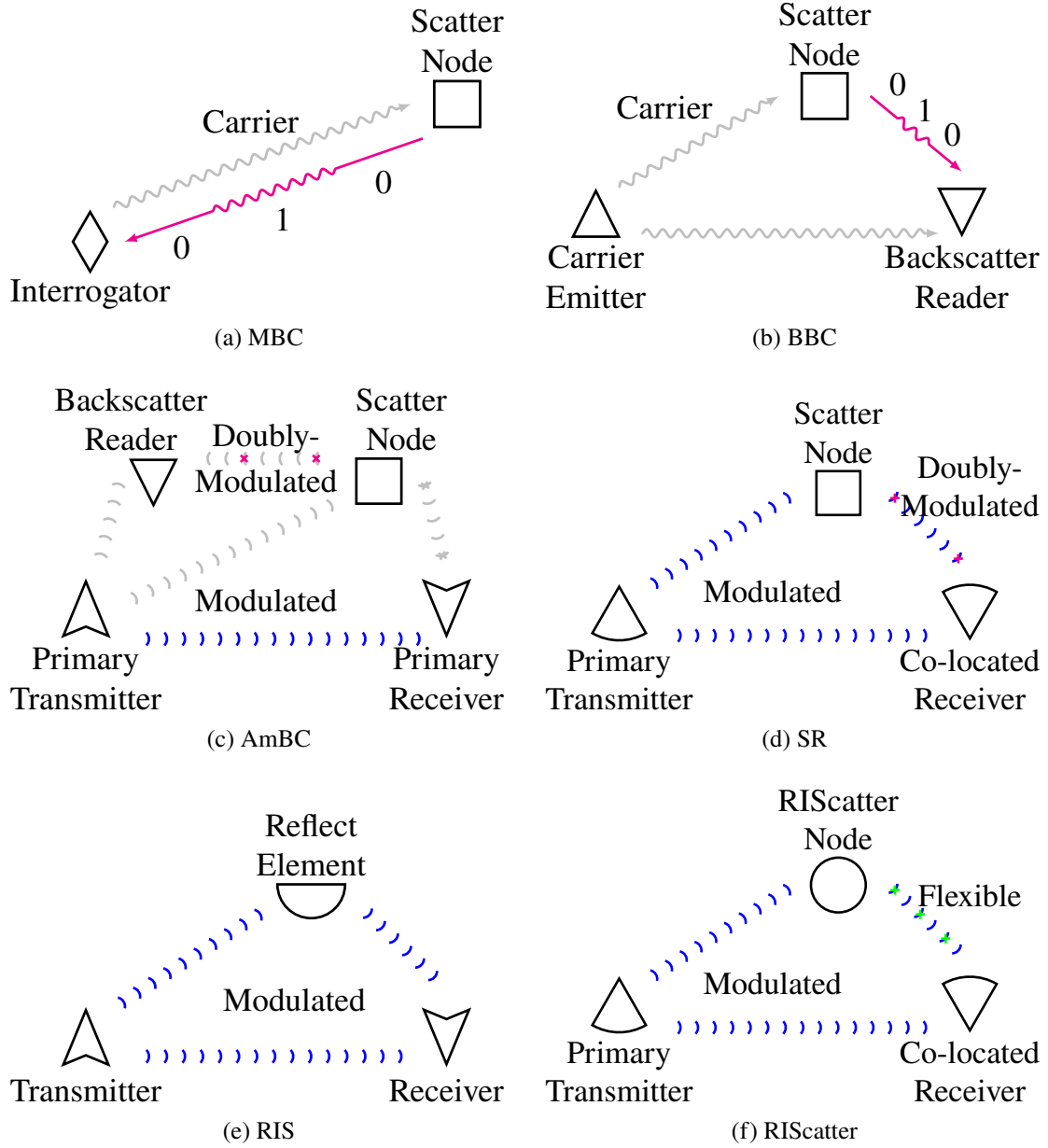
Fig. 4.1 Illustration of scattering applications. The blue flow(s) constitutes the primary link while the magenta/green flow denotes the backscatter link.

Dynamic RIS performs time sharing between different phase shifts and introduces artificial channel diversity within each channel block. The idea was first proposed to fine-tune the Orthogonal Frequency-Division Multiplexing (OFDM) resource blocks [79], then extended to the downlink power and uplink information phases of Wireless Powered Communication Network (WPCN) [80–82]. However, dynamic RIS carries no information because the reflection state at a specific time is known to the receiver. RIS can also be used as an

Table 4.1 Comparison of Scattering Applications

	MBC/BBC	AmBC	SR (large spreading factor)	RIS	RIScatter
Information link(s)	Backscatter	Coexisting	Coexisting	Primary	Coexisting
Primary signal on backscatter decoding	Carrier	Multiplicative interference	Spreading code	—	Energy uncertainty
Backscatter signal on primary decoding	—	Multiplicative interference	CSI uncertainty	Passive beamforming	Dynamic passive beamforming
Cooperative devices	—	No	Primary transmitter and co-located receiver	—	Primary transmitter, scatter nodes, and co-located receiver
Sequential decoding	—	No	Primary-to-backscatter, SIC and MRC	—	Backscatter-to-primary, no SIC/MRC
Reflection pattern depends on	Information source	Information source	Information source	CSI	Information source, CSI, and QoS
Reflection state distribution	Equiprobable	Equiprobable	Equiprobable or Gaussian	Degenerate	Flexible
Load-switching speed	Fast	Slow	Slow	Quasi-static	Arbitrary

information source, and prototypes have been developed for Phase Shift Keying (PSK) [83] and Quadrature Amplitude Modulation (QAM) [84]. From an information-theoretic perspective, the authors of [85] reported that joint transmitter-RIS encoding achieves the

capacity of RIS-aided finite-input channel, and using RIS as a naive passive beamformer to maximize the receive SNR is generally rate-suboptimal. This inspired [86–95] to combine passive beamforming and backscatter modulation in the overall RIS design. In particular, *symbol level precoding* maps the information symbols to the optimized RIS coefficient sets [86, 87], *overlay modulation* superposes the information symbols over a common auxiliary matrix [88–91], *spatial modulation* switches between the reflection coefficient sets that maximize SNR at different receive antennas [92–94], and *index modulation* employs dedicated reflection elements (resp. information elements) for passive beamforming (resp. backscatter modulation) [95]. Those RIS-based backscatter modulation schemes incur advanced hardware architecture and high optimization complexity. In contrast, [96] exploited commodity RFID tags, powered and controlled by a software-defined radio reader at a different frequency, to perform passive beamforming (but no backscatter modulation) towards a legacy user. Most relevant literature considered either Gaussian codebook [61, 62, 66–70, 90] that is impractical for low-power nodes, or finite equiprobable inputs [58, 59, 71, 72, 86–89, 91–95] that does not fully exploit the CSI and properties of active-passive coexisting networks. Those problems are addressed in this paper and the contributions are summarized below.

First, we propose RIScatter as a novel protocol that unifies BackCom and RIS by adaptive reflection state (backscatter input) distribution design. The concept is shown in Fig. 4.1(f), where one or more RIScatter nodes ride over an active transmission to simultaneously modulate their information and engineer the wireless channel. A co-located receiver cooperatively decodes both coexisting links. Each reflection state is simultaneously a passive beamforming codeword and part of information codeword. The reflection pattern over time is semi-random and guided by the input probability assigned to each state. This probability distribution is carefully designed to incorporate the backscatter information, CSI, and Quality of Service (QoS)[3]. Such an adaptive channel coding boils down to the degenerate distribution of RIS when the primary link is prioritized, and outperforms the uniform distribution of BackCom (by accounting the CSI) when the backscatter link is prioritized. Table 4.1 compares RIScatter to BackCom and RIS. However, two major challenges for RIScatter are the receiver design and input distribution design. This is the first paper to unify BackCom and RIS from the perspective of input distribution.

Second, we address the first challenge and propose a low-complexity SIC-free receiver. It semi-coherently decodes the weak backscatter signal using an energy detector, re-encodes for the exact reflection pattern, then coherently decodes the primary link. Thanks to double modulation, backscatter detection can be viewed as part of channel training, and the impact of backscatter modulation can be modelled as dynamic passive beamforming afterwards. The

---

[3]QoS refers to the relative priority of the primary link.

proposed receiver may be built over legacy receivers with minor hardware upgrade, as it only requires one additional energy comparison and re-encoding per backscatter symbol (instead of primary symbol). The energy detector can also be tailored for arbitrary input distribution and spreading factor to increase backscatter throughput. This is the first paper to propose a SIC-free cooperative receiver for active-passive coexisting networks.

Third, we address the second challenge in a single-user multi-node MISO scenario. We characterize the achievable primary-(total-)backscatter rate region by optimizing the input distribution at RIScatter nodes, the active beamforming at the AP, and the energy decision regions at the user under different QoS. A BCD algorithm is proposed where the Karush-Kuhn-Tucker (KKT) input distribution is numerically evaluated by the converging point of a sequence, the active beamforming is optimized by Projected Gradient Ascent (PGA), and the decision regions are refined by state-of-the-art sequential quantizer designs for Discrete Memoryless Thresholding Channel (DMTC). Uniquely, our optimization problem takes into account the CSI, QoS, and backscatter constellation, and the resulting input distribution is applicable to other detection schemes. This is also the first paper to reveal the importance of backscatter input distribution and decision region designs in active-passive coexisting networks.

Fourth, we provide numerical results to demonstrate the benefits of RIScatter and proposed algorithms. The observations include: 1) adaptive reflection state distribution design can flexibly shift between backscatter modulation and passive beamforming; 2) when the primary link is prioritized, input distribution becomes degenerate and RIScatter nodes coincide with discrete RIS; 3) when the backscatter link is prioritized, adaptive RIScatter encoding achieves higher backscatter rate than conventional line-coded BackCom with equiprobable inputs; 4) co-located RIScatter nodes can further leverage total backscatter rate by joint encoding; 5) the proposed receiver maintains the passive beamforming benefit and provides comparable backscatter rate to SIC-based SR, with re-encoding costs reduced to $1/N$ and no re-precoding/cancellation; 6) it also supports scatter nodes with faster load-switching speed for potentially higher throughput; 7) PGA active beamformer effectively increases the primary (resp. backscatter) rate by boosting the receive SNR (resp. widening the energy gap under different reflection states), and can smoothly transition in between under different QoS; 8) distribution-aware backscatter detectors provide higher backscatter rate than the conventional Maximum-Likelihood (ML) detector.

4.2   RIScatter

4.2.1   Principles

RF wave scattering or reflecting are often manipulated by passive antennas or programmable metamaterial [97]. The former receives the impinging signals and reradiates some back to the space, while the latter reflects at the space-cell boundary and mainly applies a phase shift. In the scattered signal, the structural mode component depends on the scatterer geometry and material. Its impact is usually modelled as part of environment multipath [98, 59], or simply a baseband DC offset when the impinging signal is a Continuous Waveform (CW) [52]. On the other hand, the antenna mode component depends on the impedance mismatch and is widely exploited in scattering applications. For an antenna (resp. metamaterial) scatterer with M reflection states, the reflection coefficient at state $m \in \mathcal{M} \triangleq \{1, \dots, M\}$ is [99, 97]

$$\Gamma_m = \frac{Z_m - Z^*}{Z_m + Z},\tag{4.1}$$

where Z_m is the antenna load (resp. metamaterial cell) impedance at state m, and Z is the antenna input (resp. medium characteristic) impedance. Specifically,

- BackCom: The scatterer is an information source with random reflection pattern over time. The reflection coefficient is used merely as part of information codeword [100]

$$\Gamma_m = \alpha_m \frac{c_m}{\max_{m'} |c_{m'}|},\tag{4.2}$$

  where $\alpha_m \in \mathbb{I}$ is the amplitude scattering ratio at state m, and c_m is the corresponding constellation point.

- RIS: The scatterer is a channel shaper with deterministic reflection pattern over time. The reflection coefficient is used merely as a passive beamforming codeword [23]

$$\Gamma_m = \alpha_m \exp(j\theta_m),\tag{4.3}$$

  where θ_m is the phase shift at state m.[4]

RIScatter generalizes BackCom and RIS from a probabilistic perspective. Each reflection coefficient simultaneously acts as a passive beamforming codeword and part of information codeword. As shown in Fig. 4.2, the reflection pattern of each RIScatter node over time is semi-random and guided by the input probability assigned to each state. This probability

---

[4]Most papers assume $\alpha_m = \alpha$, with $\alpha \ll 1$ for BackCom and $\alpha = 1$ for RIS.
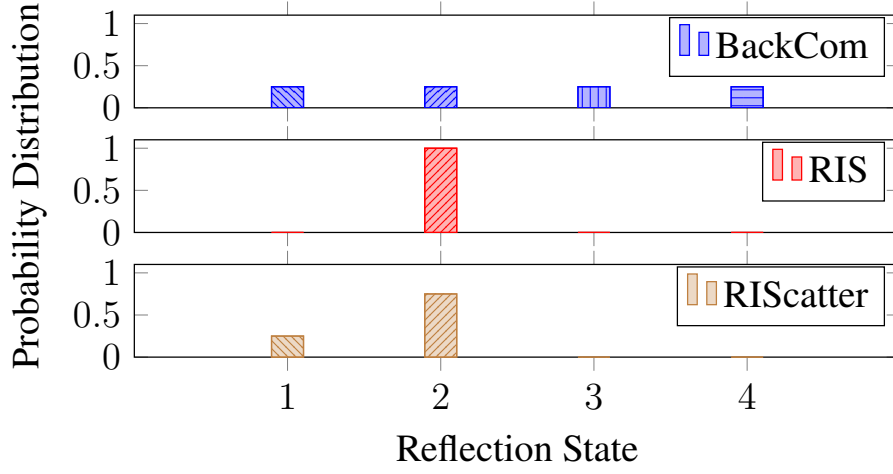
(a) Input Distribution
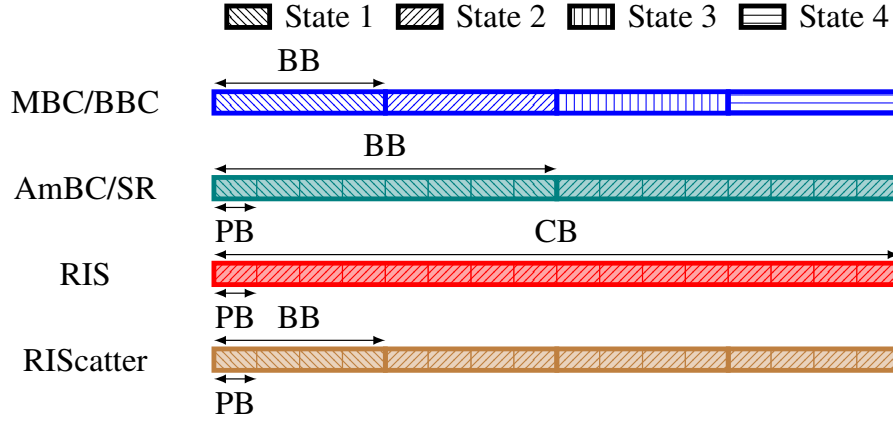
(b) Reflection Pattern

Fig. 4.2 Input distribution and reflection pattern of scattering applications. "PB", "BB", and "CB" refer to primary symbol block, backscatter symbol block, and channel block, respectively. Shadowing means presence of primary link. In this example, the optimal passive beamformer corresponds to state 2. The spreading factor is 4 for RIScatter and 8 for AmBC/SR. BackCom and RIS can be viewed as extreme cases of RIScatter, where the input distribution boils down to uniform and degenerate, respectively.

distribution is carefully designed to incorporate the backscatter information, CSI, and QoS, in order to strike a balance between backscatter modulation and passive beamforming.

Remark 3. *Unlike dynamic RIS that simply performs a time sharing between reflection states, RIScatter conveys additional information by randomizing the reflection pattern over time while still guaranteeing the probability of occurrence of each state. Upon successful backscatter detection, the impact of RIScatter nodes on the primary link can be modelled as dynamic passive beamforming.*

(a) Block Diagram   (b) Equivalent Circuit   (c) Scatter Model
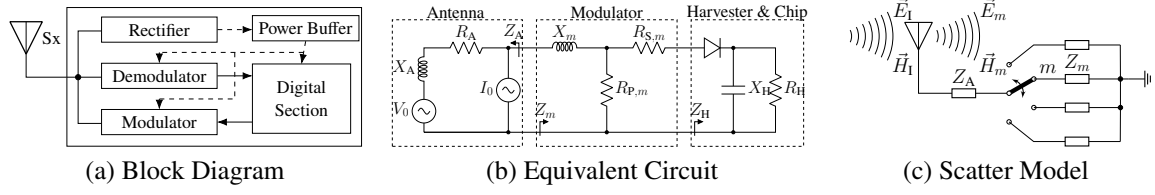
Fig. 4.3 Block diagram, equivalent circuit, and scatter model of a RIScatter node. The solid and dashed vectors represent signal and energy flows. The scatter antenna behaves as a constant power source, where the voltage V_0 and current I_0 are introduced by incident electric field $\vec{E}_\text{I}$ and magnetic field $\vec{H}_\text{I}$ [1].
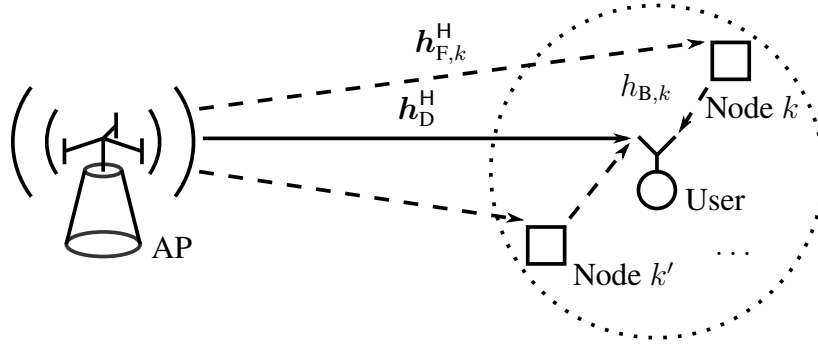
Fig. 4.4 A single-user multi-node RIScatter network.

RIScatter nodes can be implemented, for example, by adding an integrated receiver[5] [101] and adaptive encoder [102] to off-the-shelf passive RFID tags. The block diagram, equivalent circuit, and scatter model are illustrated in Fig. 4.3.

4.2.2 System Model

As shown in Fig. 4.4, we consider a RIScatter network where a Q-antenna AP serves a single-antenna user and K nearby dispersed or co-located RIScatter nodes. Without loss of generality, we assume all nodes have M available reflection states. In the primary point-to-point system, the AP transmits information to the user over a multipath channel[6] enhanced by RIScatter nodes. In the backscatter multiple access system, the AP acts as a carrier emitter, the RIScatter nodes modulate over the scattered signal, and the user jointly decodes all nodes.[7] For simplicity, we consider a quasi-static block fading model and focus

---

[5]The aim is to coordinate the node with the active source and to acquire the optimized input distribution, instead of decoding the primary information dedicated for the user. The node receiver can be implemented using simple circuits or even integrated with the rectifier [101] to reduce cost and complexity.

[6]It is assumed the primary symbol duration is much longer than multipath delay spread (i.e., no inter-symbol interference).

[7]It is assumed the signal going through two or more RIScatter nodes is too weak to be received by the user.

on a specific channel block where the CSI remains constant. Denote the AP-user direct channel as $\boldsymbol{h}_{\mathrm{D}}^{\mathsf{H}} \in \mathbb{C}^{1 \times Q}$, the AP-node $k \in \mathcal{K} \triangleq \{1, \dots, K\}$ forward channel as $\boldsymbol{h}_{\mathrm{F},k}^{\mathsf{H}} \in \mathbb{C}^{1 \times Q}$, the node k-user backward channel as $h_{\mathrm{B},k}$, and the cascaded AP-node k-user channel as $\boldsymbol{h}_{\mathrm{C},k}^{\mathsf{H}} \triangleq h_{\mathrm{B},k} \boldsymbol{h}_{\mathrm{F},k}^{\mathsf{H}} \in \mathbb{C}^{1 \times Q}$. We assume the direct and cascaded CSI are available at the AP and user[8].

Let $\alpha_k \in \mathbb{I}$ be the amplitude scattering ratio of node k, $x_k \in \mathcal{X} \triangleq \{c_1, \dots, c_M\}$ be the (coded) backscatter symbol of node k, and $x_{\mathcal{K}} \triangleq (x_1, \dots, x_K)$ be the backscatter symbol tuple of all nodes. Due to double modulation, the composite channel is a function of backscatter symbol tuple[9]

$$\boldsymbol{h}^{\mathsf{H}}(x_{\mathcal{K}}) \triangleq \boldsymbol{h}_{\mathrm{D}}^{\mathsf{H}} + \sum_k \alpha_k \boldsymbol{h}_{\mathrm{C},k}^{\mathsf{H}} x_k \tag{4.4a}$$

$$= \boldsymbol{h}_{\mathrm{D}}^{\mathsf{H}} + \boldsymbol{x}^{\mathsf{H}} \mathrm{diag}(\boldsymbol{\alpha}) \boldsymbol{H}_{\mathrm{C}}, \tag{4.4b}$$

where $\boldsymbol{\alpha} \triangleq [\alpha_1, \dots, \alpha_K]^{\mathsf{T}} \in \mathbb{I}^K$, $\boldsymbol{x} \triangleq [x_1, \dots, x_K]^{\mathsf{H}} \in \mathcal{X}^K$, and $\boldsymbol{H}_{\mathrm{C}} \triangleq [\boldsymbol{h}_{\mathrm{C},1}, \dots, \boldsymbol{h}_{\mathrm{C},K}]^{\mathsf{H}} \in \mathbb{C}^{K \times Q}$. Without loss of generality, we assume the spreading factor N is a positive integer. Within one backscatter block, the signal received by the user at primary block $n \in \mathcal{N} \triangleq \{1, \dots, N\}$ is

$$y[n] = \boldsymbol{h}^{\mathsf{H}}(x_{\mathcal{K}}) \boldsymbol{w} s[n] + v[n], \tag{4.5}$$

where $\boldsymbol{w} \in \mathbb{C}^Q$ is the active beamformer satisfying $\|\boldsymbol{w}\|^2 \leq P$, P is the maximum average transmit power, $s \sim \mathcal{CN}(0, 1)$ is the primary symbol, and $v \sim \mathcal{CN}(0, \sigma_v^2)$ is the Additive White Gaussian Noise (AWGN) with variance σ_v^2.

Let $m_k \in \mathcal{M} \triangleq \{1, \dots, M\}$ be the reflection state index of node k, and $m_{\mathcal{K}} \triangleq (m_1, \dots, m_K)$ be the state index tuple of all nodes. The backscatter symbol x_k (resp. symbol tuple $x_{\mathcal{K}}$) is a random variable that takes value x_{m_k} (resp. value tuple $x_{m_{\mathcal{K}}}$) with probability $p(x_{m_k})$ (resp. $p(x_{m_{\mathcal{K}}})$).

Remark 4. *Dispersed RIScatter nodes encode independently such that*

$$p(x_{m_{\mathcal{K}}}) = \prod_k p(x_{m_k}). \tag{4.6}$$

When multiple nodes are co-located, they can jointly encode by designing the joint probability $p(x_{m_{\mathcal{K}}})$ directly.

---

[8]The cascaded CSI can be estimated by sequential [103–105] or parallel [106] approaches for dispersed nodes, or group-based [107] or hierarchical [28] approaches for co-located nodes. The impact of channel estimation error will be investigated in Section 4.4.

[9](4.4a) and (4.4b) are often used in BackCom and RIS literature, respectively.

Let $z = \sum_n |y[n]|^2$ be the receive energy per backscatter block. When $x_{m_\mathcal{K}}$ is transmitted, the receive signal y follows CSCG distribution $\mathcal{CN}(0, \sigma^2_{m_\mathcal{K}})$ with variance

$$\sigma^2_{m_\mathcal{K}} = |\boldsymbol{h}^\mathsf{H}(x_{m_\mathcal{K}})\boldsymbol{w}|^2 + \sigma^2_v, \tag{4.7}$$

and z follows Gamma distribution with conditional Probability Density Function (PDF)

$$f(z|x_{m_\mathcal{K}}) = \frac{z^{N-1}\exp(-z/\sigma^2_{m_\mathcal{K}})}{\sigma^{2N}_{m_\mathcal{K}}(N-1)!}. \tag{4.8}$$

Remark 5. *We have assumed Gaussian codebook for the primary source and finite support for the backscatter nodes, since they are relatively practical and widely adopted in relevant literatures [63, 88, 89, 91, 95, 108]. The proposed framework is extendable to non-Gaussian primary source, and the conditional PDF* (4.8) *can be approximated using Central Limit Theorem (CLT) for large N.*

The user first jointly decodes the backscatter message of all nodes using a low-complexity energy detector.[10] The energy detector formulates a DMTC of size $M^K \times M^K$.

Remark 6. *The capacity-achieving decision region design for DMTC with non-binary inputs in arbitrary distribution remains an open issue. It was proved deterministic detectors can be rate-optimal, but non-convex regions (consist of non-adjacent partitions) are generally required and the optimal number of thresholds is unknown [110, 111]. Next, we restrict the energy detector to convex deterministic decision regions and consider sequential threshold design.*

Let $L = M^K$ be the number of decision regions. Sort $\{\sigma^2_{m_\mathcal{K}}\}$ in ascending order and denote the result sequence as $\sigma^2_1, \ldots, \sigma^2_L$. With sequential thresholding, the decision region of backscatter symbol tuple $l \in \mathcal{L} \triangleq \{1, \ldots, L\}$ is[11]

$$\mathcal{R}_l \triangleq [t_{l-1}, t_l), \quad 0 \leq t_{l-1} \leq t_l, \tag{4.9}$$

where t_l is the decision threshold between hypotheses x_l and x_{l+1}. An example is shown in Fig. 4.5.

---

[10]The reliability of the energy detector is improved by the adaptive input distribution and thresholding design. With high-order modulation or large number of scatter nodes, the reliability can be further enhanced by increasing the spreading factor or using error correction codes with low code-rate. In practice, users can decode backscatter nodes ranging from a few to hundreds of meters in the presence of noise and interference, and the backscatter throughput can reach few Kbps to tens of Mbps [109].

[11]$m_\mathcal{K}$ and l are one-to-one mapped. Both notations are used interchangeably in the following context.
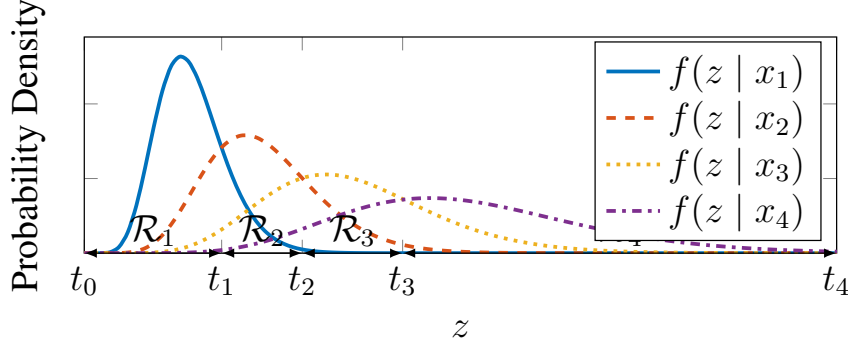
Fig. 4.5 PDF of the receive energy per backscatter block conditioned on different reflection state.

When the threshold vector $\boldsymbol{t} \triangleq [t_0, \dots, t_L]^\mathsf{T} \in \mathbb{R}_+^{L+1}$ is given, we can formulate a Discrete Memoryless Multiple Access Channel (DMMAC) with transition probability from input $x_{m_\mathcal{K}}$ to output $\hat{x}_{m'_\mathcal{K}}$ as

$$q(\hat{x}_{m'_\mathcal{K}}|x_{m_\mathcal{K}}) = \int_{\mathcal{R}_{m'_\mathcal{K}}} f(z|x_{m_\mathcal{K}})\, dz. \tag{4.10}$$

The backscatter mutual information is

$$I_\mathsf{B}(x_\mathcal{K}; \hat{x}_\mathcal{K}) = \sum_{m_\mathcal{K}} p(x_{m_\mathcal{K}}) I_\mathsf{B}(x_{m_\mathcal{K}}; \hat{x}_\mathcal{K}), \tag{4.11}$$

where $I_\mathsf{B}(x_{m_\mathcal{K}}; \hat{x}_\mathcal{K})$ is the backscatter information function

$$I_\mathsf{B}(x_{m_\mathcal{K}}; \hat{x}_\mathcal{K}) \triangleq \sum_{m'_\mathcal{K}} q(\hat{x}_{m'_\mathcal{K}}|x_{m_\mathcal{K}}) \log \frac{q(\hat{x}_{m'_\mathcal{K}}|x_{m_\mathcal{K}})}{p(\hat{x}_{m'_\mathcal{K}})}. \tag{4.12}$$

Once the backscatter information is successfully decoded, the user re-encodes to recover the reflection pattern, constructs the composite channel by (4.4), then coherently decodes the primary link. The primary mutual information is

$$I_\mathsf{P}(s; y|x_\mathcal{K}) = \sum_{m_\mathcal{K}} p(x_{m_\mathcal{K}}) I_\mathsf{P}(s; y|x_{m_\mathcal{K}}), \tag{4.13}$$

where $I_\mathsf{P}(s; y|x_{m_\mathcal{K}})$ is the primary information function

$$I_\mathsf{P}(s; y|x_{m_\mathcal{K}}) \triangleq \log\left(1 + \frac{|\boldsymbol{h}^\mathsf{H}(x_{m_\mathcal{K}})\boldsymbol{w}|^2}{\sigma_v^2}\right). \tag{4.14}$$

4.3 Rate-Region Characterization

With a slight abuse of notation, we define the weighed sum mutual information and information function as

$$I(x_{\mathcal{K}}) \triangleq \rho I_{\mathrm{P}}(s; y|x_{\mathcal{K}}) + (1 - \rho)I_{\mathrm{B}}(x_{\mathcal{K}}; \hat{x}_{\mathcal{K}}), \tag{4.15}$$

$$I(x_{m_{\mathcal{K}}}) \triangleq \rho I_{\mathrm{P}}(s; y|x_{m_{\mathcal{K}}}) + (1 - \rho)I_{\mathrm{B}}(x_{m_{\mathcal{K}}}; \hat{x}_{\mathcal{K}}), \tag{4.16}$$

where $\rho \in \mathbb{I}$ is the QoS. To obtain the achievable primary-(total-)backscatter rate region, we consider the weighted sum mutual information maximization problem with independent encoding at all nodes[12]

$$\max_{\{\boldsymbol{p}_k\}_{k\in\mathcal{K}},\boldsymbol{w},\boldsymbol{t}} \quad I(x_{\mathcal{K}}) \tag{4.17a}$$

$$\text{s.t.} \quad \mathbf{1}^{\mathsf{T}}\boldsymbol{p}_k = 1, \quad \forall k, \tag{4.17b}$$

$$\boldsymbol{p}_k \geq \mathbf{0}, \quad \forall k, \tag{4.17c}$$

$$\|\boldsymbol{w}\|^2 \leq P, \tag{4.17d}$$

$$t_{l-1} \leq t_l, \quad \forall l, \tag{4.17e}$$

$$\boldsymbol{t} \geq \mathbf{0}, \tag{4.17f}$$

where $\boldsymbol{p}_k = [p(x_{1_k}), \dots, p(x_{M_k})]^{\mathsf{T}} \in \mathbb{I}^M$ is the input distribution of node k. Problem (4.17) generalizes BackCom by allowing CSI- and QoS-adaptive input distribution and decision region design. On the other hand, it also relaxes the feasible domain of discrete RIS phase shift selection problems from the vertices of M-dimensional probability simplex to the simplex itself. The original problem is highly non-convex and we propose a BCD algorithm that iteratively updates $\{\boldsymbol{p}_k\}_{k\in\mathcal{K}}$, $\boldsymbol{w}$ and $\boldsymbol{t}$.

4.3.1 Input Distribution

For any given $\boldsymbol{w}$ and $\boldsymbol{t}$, we can formulate a DMMAC by (4.10) and simplify (4.17) to

$$\max_{\{\boldsymbol{p}_k\}_{k\in\mathcal{K}}} \quad I(x_{\mathcal{K}}) \tag{4.18a}$$

$$\text{s.t.} \quad (4.17b), (4.17c), \tag{4.18b}$$

---

[12]Joint encoding over multiple nodes can be viewed as its special case with an augmented backscatter source.

which involves the product term (4.6) and is generally non-convex (unless $K = 1$). Following [112], we first recast the KKT conditions to their equivalent forms, then propose a numerical solution that guarantees those conditions on the converging point of a sequence.

Proposition 5. *The KKT optimality conditions for problem* (4.18) *are equivalent to,* $\forall k, m_k$,

$$I_k^\star(x_{m_k}) = I^\star(x_\mathcal{K}), \quad \text{if } p^\star(x_{m_k}) > 0, \tag{4.19a}$$

$$I_k^\star(x_{m_k}) \leq I^\star(x_\mathcal{K}), \quad \text{if } p^\star(x_{m_k}) = 0, \tag{4.19b}$$

where $I_k(x_{m_k})$ *is the weighted sum marginal information*

$$I_k(x_{m_k}) \triangleq \sum_{m_{\mathcal{K}\setminus\{k\}}} p(x_{m_{\mathcal{K}\setminus\{k\}}}) I(x_{m_\mathcal{K}}). \tag{4.20}$$

Proof. Please refer to Appendix 6.2.1. □

For each RIScatter node, (4.19a) suggests each probable state should produce the same marginal information (averaged over all states of other nodes), while (4.19b) suggests any state with potentially less marginal information should not be used.

Proposition 6. *For any strictly positive initializer* $\{\boldsymbol{p}_k^{(0)}\}_{k\in\mathcal{K}}$, *the KKT input probability of node* k *at state* m_k *is given by the converging point of the sequence*

$$p^{(r+1)}(x_{m_k}) = \frac{p^{(r)}(x_{m_k}) \exp\left(\frac{\rho}{1-\rho} I_k^{(r)}(x_{m_k})\right)}{\sum_{m'_k} p^{(r)}(x_{m'_k}) \exp\left(\frac{\rho}{1-\rho} I_k^{(r)}(x_{m'_k})\right)}, \tag{4.21}$$

where r *is the iteration index.*

Proof. Please refer to Appendix 6.2.2. □

At iteration $r+1$, the input distribution of node k is updated over $\left\{ \{\boldsymbol{p}_q^{(r+1)}\}_{q=1}^{k-1}, \{\boldsymbol{p}_q^{(r)}\}_{q=k}^{K} \right\}$. The KKT input distribution design is summarized in Algorithm 6.

Remark 7. *The insufficiency of the KKT conditions for problem* (4.18) *implies that the proposed method may not converge to the global-optimal solution. However, simulation results in Section 4.4 will show that the average performance gap is indistinguishable at a moderate* K.

Algorithm 6 Input Distribution Evaluation by a Sequence

Input: K, N, $\boldsymbol{h}_{\mathrm{D}}^{\mathsf{H}}$, $\boldsymbol{H}_{\mathrm{C}}$, $\boldsymbol{\alpha}$, $\mathcal{X}$, σ_v^2, ρ, $\boldsymbol{w}$, $\boldsymbol{t}$, ϵ

Output: $\{\boldsymbol{p}_k^\star\}_{k \in \mathcal{K}}$

1: Set $\boldsymbol{h}^{\mathsf{H}}(x_{m_{\mathcal{K}}})$, $\forall m_{\mathcal{K}}$ by (4.4)
2: $\quad\ \sigma_{m_{\mathcal{K}}}^2$, $\forall m_{\mathcal{K}}$ by (4.7)
3: $\quad\ f(z|x_{m_{\mathcal{K}}})$, $\forall m_{\mathcal{K}}$ by (4.8)
4: $\quad\ q(\hat{x}_{m'_{\mathcal{K}}}|x_{m_{\mathcal{K}}})$, $\forall m_{\mathcal{K}}, m'_{\mathcal{K}}$ by (4.10)
5: Initialize $r \leftarrow 0$
6: $\quad\quad\ \boldsymbol{p}_k^{(0)} > \boldsymbol{0}$, $\forall k$
7: Get $p^{(r)}(x_{m_{\mathcal{K}}})$, $\forall m_{\mathcal{K}}$ by (4.6)
8: $\quad\ I^{(r)}(x_{m_{\mathcal{K}}})$, $\forall m_{\mathcal{K}}$ by (4.12), (4.14), (4.16)
9: $\quad\ I_k^{(r)}(x_{m_k})$, $\forall k, m_k$ by (4.20)
10: $\quad\ I^{(r)}(x_{\mathcal{K}})$ by (4.11), (4.13), (4.15)
11: **Repeat**
12: $\quad$ Update $r \leftarrow r + 1$
13: $\quad\quad\quad\ \boldsymbol{p}_k^{(r)}$, $\forall k$ by (4.21)
14: $\quad$ Redo step 7–10
15: **Until** $I^{(r)}(x_{\mathcal{K}}) - I^{(r-1)}(x_{\mathcal{K}}) \leq \epsilon$

4.3.2 Active Beamforming

For any given $\{\boldsymbol{p}_k\}_{k \in \mathcal{K}}$ and $\boldsymbol{t}$, problem (4.17) reduces to

$$\max_{\boldsymbol{w}} \quad I(x_{\mathcal{K}}) \tag{4.22a}$$

$$\text{s.t.} \quad (4.17\mathrm{d}), \tag{4.22b}$$

which is still non-convex due to the integration and entropy terms. Note the DMMAC $q(x_l|x_{m_{\mathcal{K}}})$ depends on the variance of accumulated receive energy $\sigma_{m_{\mathcal{K}}}^2$, which is a function of $\boldsymbol{w}$. Plugging (4.8) into (4.10), we have

$$q(x_l|x_{m_{\mathcal{K}}}) = \frac{\int_{t_{l-1}/\sigma_{m_{\mathcal{K}}}^2}^{t_l/\sigma_{m_{\mathcal{K}}}^2} z^{N-1} \exp(-z)\, dz}{(N-1)!} \tag{4.23}$$

$$= Q\left(N, \frac{t_{l-1}}{\sigma_{m_{\mathcal{K}}}^2}, \frac{t_l}{\sigma_{m_{\mathcal{K}}}^2}\right), \tag{4.24}$$

where $Q(N, b_1, b_2) \triangleq \int_{b_1}^{b_2} z^{N-1} \exp(-z)/(N-1)! \, dz$ is the regularized incomplete Gamma function. Its series expansion is given by [113, Theorem 3]

$$Q\left(N, \frac{t_{l-1}}{\sigma_{m_\mathcal{K}}^2}, \frac{t_l}{\sigma_{m_\mathcal{K}}^2}\right) = \exp\left(-\frac{t_{l-1}}{\sigma_{m_\mathcal{K}}^2}\right) \sum_{n=0}^{N-1} \frac{\left(\frac{t_{l-1}}{\sigma_{m_\mathcal{K}}^2}\right)^n}{n!}$$
$$- \exp\left(-\frac{t_l}{\sigma_{m_\mathcal{K}}^2}\right) \sum_{n=0}^{N-1} \frac{\left(\frac{t_l}{\sigma_{m_\mathcal{K}}^2}\right)^n}{n!}, \tag{4.25}$$

whose gradient with respect to $\boldsymbol{w}^*$ is

$$\nabla_{\boldsymbol{w}^*} Q\left(N, \frac{t_{l-1}}{\sigma_{m_\mathcal{K}}^2}, \frac{t_l}{\sigma_{m_\mathcal{K}}^2}\right) = \frac{\boldsymbol{h}(x_{m_\mathcal{K}})\boldsymbol{h}^\mathsf{H}(x_{m_\mathcal{K}})\boldsymbol{w}}{(\sigma_{m_\mathcal{K}}^2)^2}$$
$$\times \left(g_{m_\mathcal{K}}(t_l) - g_{m_\mathcal{K}}(t_{l-1})\right), \tag{4.26}$$

where

$$g_{m_\mathcal{K}}(t_l) = t_l \exp\left(-\frac{t_l}{\sigma_{m_\mathcal{K}}^2}\right)\left(-1 + \sum_{n=1}^{N-1} \frac{\left(n - \frac{t_l}{\sigma_{m_\mathcal{K}}^2}\right)\left(\frac{t_l}{\sigma_{m_\mathcal{K}}^2}\right)^{n-1}}{n!}\right). \tag{4.27}$$

On top of (4.25) and (4.26), we rewrite $I(x_\mathcal{K})$ and $\nabla_{\boldsymbol{w}^*} I(x_\mathcal{K})$ as (4.28) and (4.29) at the end of page 50, respectively. Problem (4.22) can thus be solved by the PGA method. At iteration $r + 1$, the unregulated active beamformer is updated by

$$\bar{\boldsymbol{w}}^{(r+1)} = \boldsymbol{w}^{(r)} + \gamma \nabla_{\boldsymbol{w}^*} I^{(r)}(x_\mathcal{K}), \tag{4.30}$$

$$I(x_\mathcal{K}) = \sum_{m_\mathcal{K}} p(x_{m_\mathcal{K}})\left(\rho \log\left(1 + \frac{|\boldsymbol{h}^\mathsf{H}(x_{m_\mathcal{K}})\boldsymbol{w}|^2}{\sigma_v^2}\right) + (1-\rho) \sum_l Q\left(N, \frac{t_{l-1}}{\sigma_{m_\mathcal{K}}^2}, \frac{t_l}{\sigma_{m_\mathcal{K}}^2}\right) \log \frac{Q\left(N, \frac{t_{l-1}}{\sigma_{m_\mathcal{K}}^2}, \frac{t_l}{\sigma_{m_\mathcal{K}}^2}\right)}{\sum_{m_\mathcal{K}'} p(x_{m_\mathcal{K}'}) Q\left(N, \frac{t_{l-1}}{\sigma_{m_\mathcal{K}'}^2},}\right.$$
$$\tag{4.28}$$

$$\nabla_{\boldsymbol{w}^*} I(x_\mathcal{K}) = \sum_{m_\mathcal{K}} p(x_{m_\mathcal{K}})\left(\rho \frac{\boldsymbol{h}(x_{m_\mathcal{K}})\boldsymbol{h}^\mathsf{H}(x_{m_\mathcal{K}})\boldsymbol{w}}{\sigma_{m_\mathcal{K}}^2} + (1-\rho) \sum_l \left(\log \frac{Q\left(N, \frac{t_{l-1}}{\sigma_{m_\mathcal{K}}^2}, \frac{t_l}{\sigma_{m_\mathcal{K}}^2}\right)}{\sum_{m_\mathcal{K}'} p(x_{m_\mathcal{K}'}) Q\left(N, \frac{t_{l-1}}{\sigma_{m_\mathcal{K}'}^2}, \frac{t_l}{\sigma_{m_\mathcal{K}'}^2}\right)} + 1\right)\right.$$
$$\left. \times \nabla_{\boldsymbol{w}^*} Q\left(N, \frac{t_{l-1}}{\sigma_{m_\mathcal{K}}^2}, \frac{t_l}{\sigma_{m_\mathcal{K}}^2}\right) - \frac{Q\left(N, \frac{t_{l-1}}{\sigma_{m_\mathcal{K}}^2}, \frac{t_l}{\sigma_{m_\mathcal{K}}^2}\right) \sum_{m_\mathcal{K}'} p(x_{m_\mathcal{K}'}) \nabla_{\boldsymbol{w}^*} Q\left(N, \frac{t_{l-1}}{\sigma_{m_\mathcal{K}'}^2}, \frac{t_l}{\sigma_{m_\mathcal{K}'}^2}\right)}{\sum_{m_\mathcal{K}'} p(x_{m_\mathcal{K}'}) Q\left(N, \frac{t_{l-1}}{\sigma_{m_\mathcal{K}'}^2}, \frac{t_l}{\sigma_{m_\mathcal{K}'}^2}\right)}\right)$$
$$\tag{4.29}$$

Algorithm 7 Active Beamforming Optimization by PGA

Input: Q, N, $\boldsymbol{h}_{\mathrm{D}}^{\mathsf{H}}$, $\boldsymbol{H}_{\mathrm{C}}$, $\boldsymbol{\alpha}$, $\mathcal{X}$, P, σ_v^2, ρ, $\{\boldsymbol{p}_k\}_{k\in\mathcal{K}}$, $\boldsymbol{t}$, α, β, γ, ϵ

Output: $\boldsymbol{w}^\star$

 1: Set $\boldsymbol{h}^{\mathsf{H}}(x_{m_\mathcal{K}})$, $\forall m_\mathcal{K}$ by (4.4)

 2:     $p(x_{m_\mathcal{K}})$, $\forall m_\mathcal{K}$ by (4.6)

 3: Initialize $r \leftarrow 0$

 4:            $\boldsymbol{w}^{(0)}$, $\|\boldsymbol{w}^{(0)}\|^2 \leq P$

 5: Get $(\sigma_{m_\mathcal{K}}^{(r)})^2$, $\forall m_\mathcal{K}$ by (4.7)

 6:     $Q^{(r)}\big(N, \frac{t_{l-1}}{\sigma_{m_\mathcal{K}}^2}, \frac{t_l}{\sigma_{m_\mathcal{K}}^2}\big)$, $\forall m_\mathcal{K}, l$ by (4.25)

 7:     $I^{(r)}(x_\mathcal{K})$ by (4.28)

 8:     $\nabla_{\boldsymbol{w}^*} Q^{(r)}\big(N, \frac{t_{l-1}}{\sigma_{m_\mathcal{K}}^2}, \frac{t_l}{\sigma_{m_\mathcal{K}}^2}\big)$, $\forall m_\mathcal{K}, l$ by (4.26)

 9:     $\nabla_{\boldsymbol{w}^*} I^{(r)}(x_\mathcal{K})$ by (4.29)

10: **Repeat**

11:     Update $r \leftarrow r + 1$

12:            $\gamma^{(r)} \leftarrow \gamma$

13:            $\bar{\boldsymbol{w}}^{(r)}$ by (4.30)

14:            $\boldsymbol{w}^{(r)}$ by (4.31)

15:     Redo step 5–7

16:     **While** $I^{(r)}(x_\mathcal{K}) < I^{(r-1)}(x_\mathcal{K}) + \alpha\gamma \|\nabla_{\boldsymbol{w}^*} I^{(r-1)}(x_\mathcal{K})\|^2$

17:         Set $\gamma^{(r)} \leftarrow \beta\gamma^{(r)}$

18:         Redo step 13–15

19:     **End While**

20:     Redo step 8, 9

21: **Until** $\|\boldsymbol{w}^{(r)} - \boldsymbol{w}^{(r-1)}\| \leq \epsilon$

---

where γ is the step size (refinable by backtracking line search [114, Section 9.2]). Then, $\bar{\boldsymbol{w}}$ is projected onto the feasible domain (4.17d) to retrieve the active beamformer

$$\boldsymbol{w} = \frac{\sqrt{P}\bar{\boldsymbol{w}}}{\max\big(\sqrt{P}, \|\bar{\boldsymbol{w}}\|\big)}. \tag{4.31}$$

The PGA active beamforming design is summarized in Algorithm 7.

4.3.3 Decision Threshold

For any given $\{\boldsymbol{p}_k\}_{k\in\mathcal{K}}$ and $\boldsymbol{w}$, problem (4.17) reduces to

$$\max_{\boldsymbol{t}} \quad I(x_\mathcal{K}) \tag{4.32a}$$

$$\text{s.t.} \quad (4.17e), (4.17f), \tag{4.32b}$$
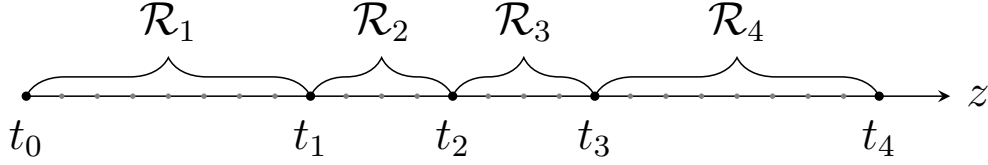
Fig. 4.6 The thresholds are chosen from fine-grained candidates instead of the continuous space. Each decision region consists of at least one bin.

which is still non-convex since t appears on the limits of integration (4.10). Instead of solving it directly, we constrain the feasible domain from continuous space $\mathbb{R}_+^{L+1}$ to discrete candidates (i.e., fine-grained energy levels) $\mathcal{T}^{L+1}$. As shown in Fig. 4.6, the decision regions are formulated by grouping adjacent energy bins.

Remark 8. *The design of the energy detector does not affect the primary achievable rate, since the composite channel* (4.4) *can always be determined after backscatter decoding and re-encoding. This implies that any thresholding maximizing the total backscatter rate is optimal for problem* (4.32).

Remark 9. *In terms of total backscatter rate, the nodes can be viewed as an augmented source, and problem* (4.32) *becomes the rate-optimal quantizer design for DMTC.*

Thanks to Remark 8 and 9, problem (4.32) can be recast as

$$\max_{t \in \mathcal{T}^{L+1}} \quad I_{\mathrm{B}}\big(x_{\mathcal{K}}; \hat{x}_{\mathcal{K}}\big) \tag{4.33a}$$

$$\text{s.t.} \quad (4.17e), \tag{4.33b}$$

whose global optimal solution has been obtained in recent works. [115] started from the quadrangle inequality and proposed a Dynamic Programming (DP) method accelerated by the Shor-Moran-Aggarwal-Wilber-Klawe (SMAWK) algorithm with computational complexity $\mathcal{O}\big(L^2(\mathrm{card}(\mathcal{T}) - L)\big)$. On the other hand, [116] started from the optimality condition for three neighbor thresholds and presented a traverse-then-bisect algorithm with complexity $\mathcal{O}\big(\mathrm{card}(\mathcal{T})L\log(\mathrm{card}(\mathcal{T})L)\big)$. In Section 4.4, both schemes will be compared with the ML scheme [108]

$$t_l^{\mathrm{ML}} = N\frac{\sigma_{l-1}^2\sigma_l^2}{\sigma_{l-1}^2 - \sigma_l^2} \log \frac{\sigma_{l-1}^2}{\sigma_l^2}, \quad l \in \mathcal{L} \setminus \{L\}, \tag{4.34}$$

which is suboptimal for problem (4.32) unless all nodes are with equiprobable inputs.

4.4   Simulation Results

In this section, we provide numerical results to evaluate the proposed algorithms. We assume the AP-user distance is $10\,\mathrm{m}$ and at least one RIScatter nodes are randomly dropped in a disk centered at the user with radius r. The AP is with maximum average transmit power $P = 36\,\mathrm{dBm}$ and all nodes employs M-QAM with $\alpha = 0.5$. For all channels involved, we consider a distance-dependent path loss model

$$L(d) = L_0 \left(\frac{d_0}{d} \right)^{\gamma}, \tag{4.35}$$

together with a Rician fading model

$$\boldsymbol{H} = \sqrt{\frac{\kappa}{1+\kappa}} \bar{\boldsymbol{H}} + \sqrt{\frac{1}{1+\kappa}} \tilde{\boldsymbol{H}}, \tag{4.36}$$

where d is the transmission distance, $L_0 = -30\,\mathrm{dB}$ is the reference path loss at $d_0 = 1\,\mathrm{m}$, κ is the Rician K-factor, $\bar{\boldsymbol{H}}$ is the deterministic line-of-sight component with unit-magnitude entries, and $\tilde{\boldsymbol{H}}$ is the Rayleigh fading component with standard independent and identically distributed (i.i.d.) CSCG entries. We choose $\gamma_\mathrm{D} = 2.6$, $\gamma_\mathrm{F} = 2.4$, $\gamma_\mathrm{B} = 2$, and $\kappa_\mathrm{D} = \kappa_\mathrm{F} = \kappa_\mathrm{B} = 5$ for direct, forward and backward links. The finite decision threshold domain $\mathcal{T}$ is obtained by b-bit uniform discretization over the critical interval defined by the $1 - \varepsilon$ confidence bounds of edge hypotheses (i.e., lower bound of x_1 and upper bound of x_L). We set $b = 9$ and $\varepsilon = 10^{-3}$. All achievable rate regions are averaged over 10^3 channel realizations.[13]

4.4.1   Evaluation of Proposed Algorithms

Initialization

To characterize the achievable rate region, we progressively obtain all boundary points by successively increasing ρ and solving problem (4.17). For $\rho = 0$ where the backscatter link is prioritized, we initialize Algorithm 6 and 7 by uniform input distribution and MRT towards the sum cascaded channel $\sum_k \boldsymbol{h}_{\mathrm{C},k}^{\mathsf{H}}$, respectively. At the following points, both algorithms are initialized by the solutions at the previous point.
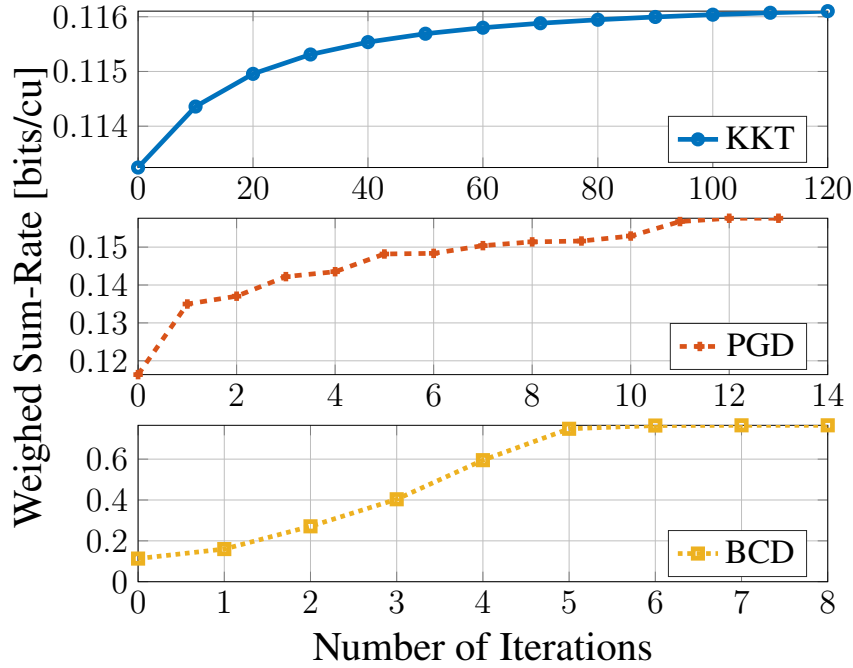
Fig. 4.7 Typical convergence curves at $\rho = 0$ for $Q = 4$, $K = 8$, $M = 2$, $N = 20$, $\sigma_v^2 = -40\,\mathrm{dBm}$ and $r = 2\,\mathrm{m}$.

Convergence

The BCD algorithm is convergent for problem (4.17) since the input distribution and active beamforming subproblems converge and the thresholding subproblem attains global optimality. In company with BCD, we also plotted the convergence results of KKT and PGA algorithms in Fig. 4.7 to show how much performance is gained by solving each subproblem. It is observed that Algorithm 6 and 7 take around 100 and 10 iterations to converge, respectively. Overall, the BCD algorithm requires at most 5 iterations to converge. As ρ increases (not presented here), the convergence of all three algorithms are much faster thanks to the progressive initialization.

4.4.2   Comparison of Scattering Applications

On top of the setup in Fig. 4.4, we consider RIScatter and the following benchmark applications:

- *Legacy:* Legacy transmission without scatter nodes.

---

[13]The code is publicly available at https://github.com/snowztail/riscatter/.

- *BBC:* The primary signal is CW and the receive signal is

$$y^{\text{BBC}}[n] = \left(\boldsymbol{h}_{\text{D}}^{\text{H}} + \sum_k \alpha_k \boldsymbol{h}_{\text{C},k}^{\text{H}} x_k\right)\boldsymbol{w} + v[n].$$ (4.37)

The total backscatter rate approaches $K \log M$ when N is sufficiently large.

- *AmBC:* The user decodes each link independently and semi-coherently while treating the other as interference. The primary achievable rate is approximately[14]

$$I_{\text{P}}^{\text{AmBC}}(s;y) \approx \log\left(1 + \frac{|\boldsymbol{h}_{\text{D}}^{\text{H}}\boldsymbol{w}|^2}{\sum_k |\alpha_k \boldsymbol{h}_{\text{C},k}^{\text{H}}\boldsymbol{w}|^2 + \sigma_v^2}\right),$$ (4.38)

while the total backscatter rate follows (4.11) with uniform input distribution.

- *SR:* For a sufficiently large N, the average primary rate under semi-coherent detection asymptotically approaches (4.13) with uniform input distribution [66]. When $s[n]$ is successfully decoded and the direct interference $\boldsymbol{h}_{\text{D}}^{\text{H}}\boldsymbol{w}s[n]$ is perfectly cancelled, the intermediate signal is

$$\hat{y}^{\text{SR}}[n] = \sum_k \alpha_k \boldsymbol{h}_{\text{C},k}^{\text{H}} x_k \boldsymbol{w}s[n] + v[n].$$ (4.39)

The total backscatter rate approaches $K \log M$.

- *RIS:* The reflection pattern is deterministic and the total backscatter rate is zero. The primary achievable rate is a special case of (4.13)

$$I_{\text{P}}^{\text{RIS}}(s;y|x_{\mathcal{K}}) = I_{\text{P}}(s;y|x_{m_{\mathcal{K}}^{\star}}) = \log\left(1 + \frac{|\boldsymbol{h}^{\text{H}}(x_{m_{\mathcal{K}}^{\star}})\boldsymbol{w}|^2}{\sigma_v^2}\right),$$ (4.40)

where $m_{\mathcal{K}}^{\star} = \arg\max_{m_{\mathcal{K}}} I_{\text{P}}^{\text{RIS}}(s;y|x_{m_{\mathcal{K}}})$.

Fig. 4.8 compares the typical achievable rate region/points of RIScatter and those strategies. *First,* we observe BBC and SR achieve the best backscatter performance thanks to the coherent decoding. For SR, this comes with the cost of N re-encoding, precoding, subtraction together with a time-domain MRC per backscatter symbol. Since SR requires a very large N to guarantee the primary rate, the signal processing cost at the receiver can be prohibitive, and the backscatter *throughput* can be severely constrained. *Second,* the average primary

---

[14]The scattered component is treated as interference with average power $\mathbb{E}\{\sum_k \alpha_k \boldsymbol{h}_{\text{C},k}^{\text{H}} x_k \boldsymbol{w}s[n]\} = \sum_k |\alpha_k \boldsymbol{h}_{\text{C},k}^{\text{H}} \boldsymbol{w}|^2$ [66].
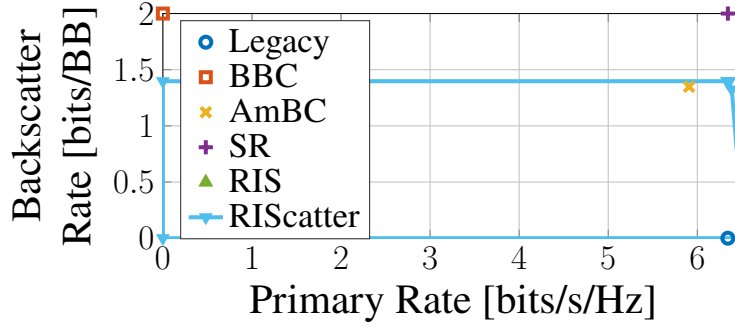
Fig. 4.8 Typical achievable rate region/points of scattering applications for $Q = 1$, $K = 1$, $M = 4$, $N = 10^3$, $\sigma_v^2 = -40\,\mathrm{dBm}$ and $r = 2\,\mathrm{m}$.

rate slightly decreases/increases in the presence of a AmBC/RIS node, and the benefit of SR is not obvious. This is because the cascaded channel is around $25\,\mathrm{dB}$ weaker than the direct channel. Here, RIS ensures a constructive superposition of the direct and scattered components, while SR only creates a quasi-static rich-scattering environment that marginally enhances the average primary rate. When N is moderate, the randomly scattered signals should be modelled as interference rather than stable multipath, and the SR point should move vertically towards the AmBC point. *Third,* RIScatter enables a flexible primary-backscatter tradeoff with adaptive input distribution design. In terms of maximum primary achievable rate, RIScatter coincides with RIS and outperforms the others by using the static reflection pattern that maximizes the primary SNR all the time. On the other hand, its maximum backscatter achievable rate is higher than that of AmBC. This is because the adaptive channel coding of RIScatter outperforms the equiprobable inputs of AmBC, especially at the low backscatter SNR caused by double fading. When multiple antenna is available at the AP, active beamforming can be optimized for RIScatter nodes and the advantage over AmBC should be more prominent.

4.4.3 Input Distribution under Different QoS

The objective is to demonstrate RIScatter nodes can leverage CSI- and QoS-adaptive input distribution design to balance backscatter modulation and passive beamforming. For one RIScatter node with $M = 4$, we evaluate the KKT input distribution at different QoS and present the result in Fig. 4.9. At $\rho = 0$ where the backscatter performance is prioritized, the optimal input distribution is 0 on two states and nearly uniform on the other two. This is inline with Shannon's observation that binary antipodal inputs is good enough for channel capacity at low SNR [2]. When the scattered signal is relatively weak, the conditional energy PDF under different hypotheses can be closely spaced as in Fig. 4.5. The extreme states
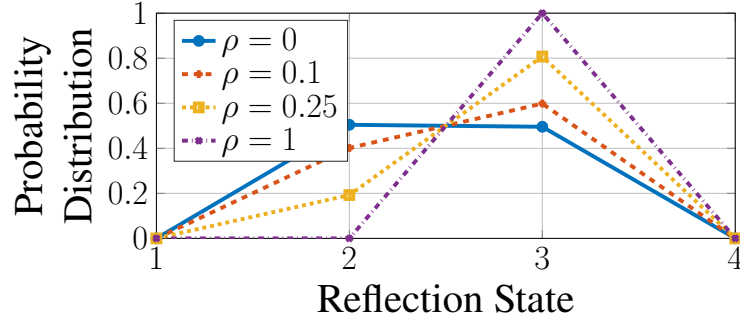
Fig. 4.9 Typical RIScatter reflection state distribution at different ρ for $Q = 1$, $K = 1$, $M = 4$, $N = 20$, $\sigma_v^2 = -40\,\mathrm{dBm}$ and $r = 2\,\mathrm{m}$.

producing the lowest/highest energy are always assigned with non-zero probability, while the middles cannot provide enough energy diversity and end up unused. At $\rho = 1$ where the primary link is prioritized, the optimal input distribution is $[0, 0, 1, 0]^{\mathsf{T}}$ since state 3 provides higher primary SNR than other states. That is, the reflection pattern becomes deterministic and the RIScatter node boils down to a static discrete RIS element. Increasing ρ from 0 to 1 creates a smooth transition from backscatter modulation to passive beamforming, suggesting RIScatter unifies BackCom and RIS from a probabilistic perspective.

4.4.4 Rate Region by Different Schemes

Input Distribution

We compare these input distribution designs for problem (4.18):

- *Cooperation:* Joint encoding using a joint probability array $p(x_{m_\mathcal{K}})$ with M^K entries by Algorithm 6;

- *Exhaustion:* Exhaustive search over the M-dimensional probability simplex with resolution $\Delta p = 10^{-2}$;

- *KKT:* Solution by Algorithm 6;

- *Equiprobable:* Uniform input distribution.

We also consider these independent distribution recovery methods from the joint probability array:

- *Marginalization:* Marginal probability distributions;

- *Decomposition:* Normalized rank-1 Canonical Polyadic (CP) decomposed tensors by `Tensor Toolbox` [117];

(a) Input Distribution, $Q = 1$

(b) Active Beamforming, $Q = 4$

(c) Decision Threshold, $Q = 4$
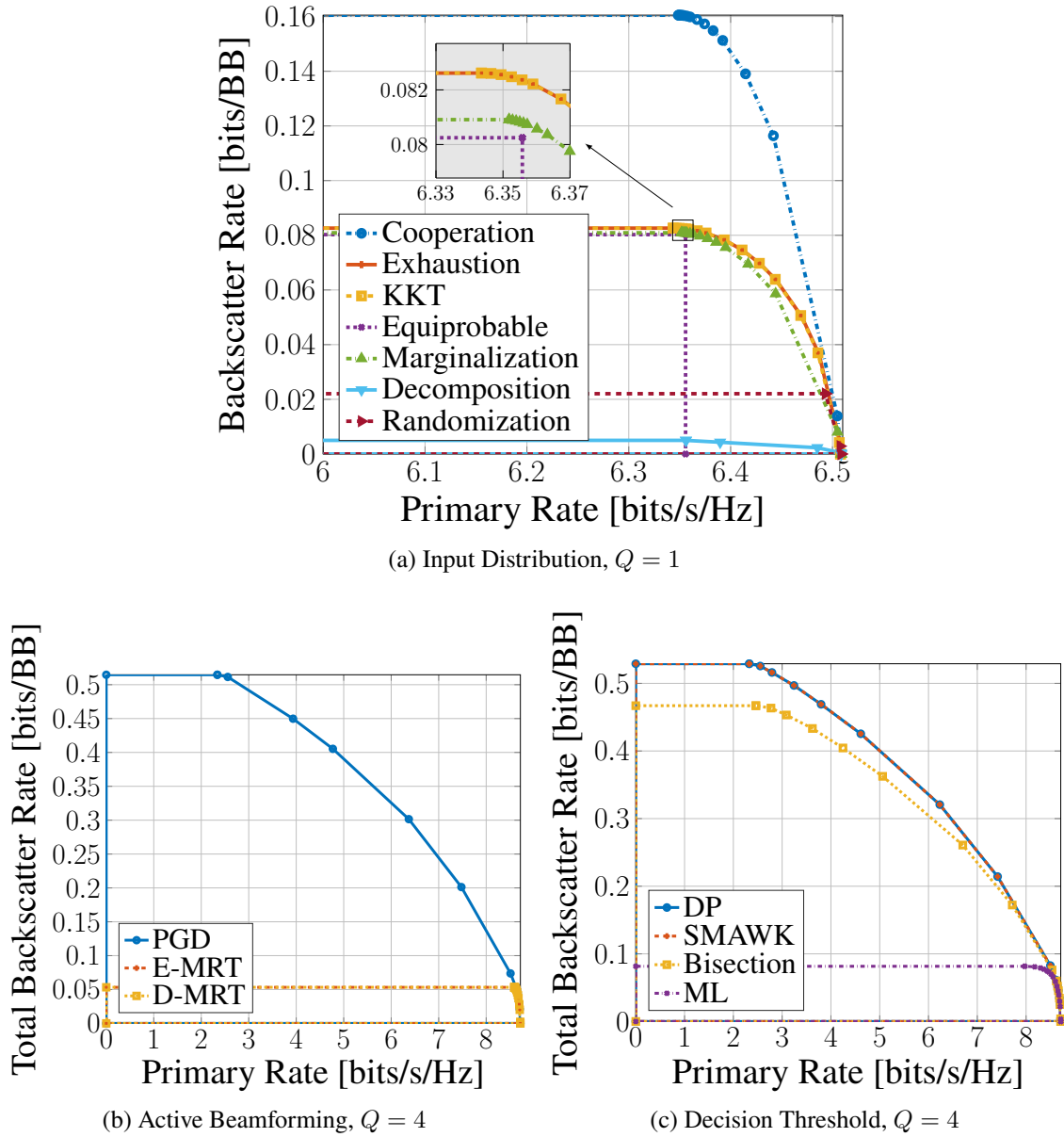
Fig. 4.10 Average primary-total-backscatter rate regions by different input distribution, active beamforming, and decision threshold schemes for $K = 2$, $M = 4$, $N = 20$, $\sigma_v^2 = -40\,\mathrm{dBm}$ and $r = 2\,\mathrm{m}$.

- *Randomization:* Gaussian randomization with the guidance of correlation matrix [118].

Fig. 4.10(a) shows their average achievable rate regions. Cooperation achieves the outer bound of all schemes, but joint encoding over passive devices may incur additional hardware cost. Besides, the average rate performance of Exhaustion and KKT completely coincide with each other when $K = 2$. This confirms Remark 7 that the KKT input distribution can be good enough when K is moderate. Equiprobable experiences minor backscatter and major

primary rate losses without exploiting CSI and QoS, and those gaps should be larger when M or K increases. Marginalization provides a close performance to KKT, but Randomization and Decomposition fail our expectations for most channel realizations. Those observations emphasize the importance of adaptive RIScatter encoding and demonstrate the advantage of the proposed KKT input distribution design.

Active Beamforming

We consider three typical active beamforming schemes for problem (4.22):

- *PGA:* Solution by Algorithm 7;

- *E-MRT:* MRT towards the ergodic composite channel $\sum_{m_{\mathcal{K}}} p(x_{m_{\mathcal{K}}}) \boldsymbol{h}^{\mathsf{H}}(x_{m_{\mathcal{K}}})$;

- *D-MRT:* MRT towards the direct channel $\boldsymbol{h}_{\mathrm{D}}^{\mathsf{H}}$.

Fig. 4.10(b) presents the average achievable rate regions for those schemes. In the low-ρ regime, the proposed PGA beamformer significantly outperforms both MRT schemes in terms of total backscatter rate. This is because the semi-coherent backscatter decoding relies on the relative energy difference under different backscatter symbol tuples. Such an energy diversity is enhanced by PGA that effectively exploits backscatter constellation and input distribution knowledge rather than simply maximizes the channel strength. As ρ increases, the primary SNR outweighs the backscatter energy difference in (4.28), and PGA beamformer approaches E-MRT. At $\rho = 1$, both PGA and E-MRT boil down to MRT towards the strongest composite channel. The difference between E-MRT and D-MRT is insignificant when RIScatter nodes are dispersed. Those observations confirm that the proposed PGA active beamforming design can exploit the CSI, QoS, and backscatter constellation to enlarge the achievable rate region.

Decision Threshold

We evaluate the following decision threshold strategies for problem (4.33):

- *DP:* Benchmark DP method for sequential quantizer [115];

- *SMAWK:* DP accelerated by the SMAWK algorithm [115];

- *Bisection:* The traverse-then-bisect algorithm [116];

- *ML:* Maximum likelihood detector (4.34) [108].

Fig. 4.10(c) reveals the average achievable rate region for those strategies. The distribution-aware schemes DP, SMAWK and Bisection ensure higher total backscatter rate than ML. This is because the total backscatter rate (4.11) is a function of both input distribution and decision regions, and the rate-optimal thresholding depends heavily on the input distribution. For example, the backscatter symbol tuples with zero input probability should be assigned with empty decision regions, in order to increase the success detection rates of other hypotheses. It highlights the importance of joint input distribution and decision threshold design in rate maximization problems.

4.4.5   Rate Region under Different Configurations

In this study, we choose $Q = 4$, $K = 8$, $M = 2$, $N = 20$, $\sigma_v^2 = -40\,\mathrm{dBm}$ and $r = 2\,\mathrm{m}$ as a reference, unless otherwise specified.

Number of Nodes

Fig. 4.11(a) reveals how the number RIScatter nodes K influences the primary-backscatter tradeoff. Interestingly, we observe that increasing K has a larger benefit on the total backscatter rate than primary. This is because each RIScatter node not only affects the primary SNR but also influences the relative energy difference that other nodes can make. To maximize the total backscatter rate, some nodes closer to the user may need to sacrifice their own rate and use the state that *minimizes* the composite channel strength, in order to increase the backscatter rate of other nodes. This accounts for the significant primary rate decrease in the low-ρ regime. On the other hand, when the primary link is prioritized, the RIScatter nodes boil down to RIS elements and enjoy a passive array gain of K^2.

Number of States

Fig. 4.11(b) shows the relationship between the available reflection states (i.e., QAM order) M and the achievable rate region when $K = 1$. We notice that increasing the reflection states has a marginal effect on the primary rate but significantly improves the backscatter rate. This is because the maximum amplitude normalized-QAM (4.2) involves more weak reflection points as M increases. It enhances the receive energy diversity but cannot provide enough phase shift resolution with maximum reflection.

Number of Transmit Antennas

Fig. 4.11(c) illustrates the impact of transmit antennas Q on the average performance. As Q increases, more scattered paths become available and the channel diversity can be better exploited to improve the primary-backscatter tradeoff. It emphasizes the importance of multi-antenna RIScatter systems and demonstrate the effectiveness of the proposed PGA design.

Spreading factor

Fig. 4.11(d) shows how the spreading factor N affects the achievable rate region.[15] Using a very large N (as in the case of SR) can severely constrain the backscatter throughput, since the gain in energy certainty (by the law of large numbers) cannot withstand the loss in the gross rate. As $N \to \infty$, RIScatter nodes boil down to static RIS elements and the total backscatter rate approaches 0. On the other hand, when N is too small, the DMMAC (4.10) becomes unreliable and energy detection is error-prone. It explains the observation that $N = 10$ provides lower backscatter throughput than $N = 20$. Therefore, we conclude the spreading factor N should be carefully designed over multiple factors (e.g., primary and backscatter SNR, data rate requirements, load switching speed at the nodes, and signal processing capability at the user).

Average Noise Power

Fig. 4.11(e) depicts the impact of average noise power σ_v^2 on average rate regions. Note that the noise influences both primary and backscatter SNR. When σ_v^2 relatively high, one can choose a larger N to improve the SNR of energy detection.

Imperfect CSI

Due to the lack of RF chains at RIScatter nodes, fast and accurate acquisition of the cascaded CSI can be challenging, especially when the backscatter SNR is weak or the number of nodes is large. We consider an imperfect CSI model, where the cascaded channel of node k is estimated as

$$\hat{\boldsymbol{h}}_{\mathrm{C},k} = \boldsymbol{h}_{\mathrm{C},k} + \tilde{\boldsymbol{h}}_{\mathrm{C},k}, \tag{4.41}$$

$\tilde{\boldsymbol{h}}_{\mathrm{C},k}$ is the estimation error with entries following i.i.d. CSCG distribution $\mathcal{CN}(0, \iota\Lambda_{\mathrm{C}})$, ι is the relative estimation error, and Λ_{C} is the cascaded path loss. In Fig. 4.11(f), it is observed that the channel estimation error mainly affects the backscatter rate. When ι increases from 0

---

[15]Here, the unit of total backscatter rate is bits per primary block to show backscatter throughput.

to 0.2, the maximum total backscatter rate decreases by 20%. This is because the energy detector is sensitive to the DMMAC (4.10) and thus the estimation of the cascaded channel. On the other hand, a small estimation error may be insufficient to change the optimal passive beamforming state and the primary rate is almost unchanged.

Primary SNR

The backscatter SNR is fixed to $0\,\mathrm{dB}$ with $Q = 1$ in this study. Interestingly, Fig. 4.11(g) shows that increasing the primary SNR can improve the primary rate but degrade the backscatter rate. The reason is that the relative strength of the scattered signal compared to the direct signal is weakened, such that the nodes cannot make enough difference to the energy detector. This, together with Fig. 4.10(b) and 4.11(a), emphasizes the importance of balancing the primary and backscatter SNR in the design of active-passive coexisting networks.

Backscatter SNR

The primary SNR is fixed to $20\,\mathrm{dB}$ with $Q = 1$ in this study. Fig. 4.11(h) shows that the primary and backscatter rates are both improved when the backscatter SNR increases. This motivates one to use high-efficiency or semi-passive RIScatter nodes to improve the overall performance. In a multi-user RIScatter network, each node may be assigned to the nearest user to guarantee uniformly good performance for both links.

4.5   Conclusion

This paper introduced RIScatter as a novel scatter protocol that bridges backscatter modulation and passive beamforming. Starting from scattering principles, we showed how RIScatter nodes generalize information nodes of BackCom and reflect elements of RIS, how they can be built over existing passive scatter devices, and how they simultaneously encode self information and assist legacy transmission. We also proposed a practical SIC-free receiver that exploits the properties of active-passive coexisting networks to benefit both subsystems. The achievable primary-total-backscatter rate region was then studied for a single-user multi-node RIScatter network, where the input distribution, active beamforming, and decision thresholds are iteratively updated. Numerical results validated the proposed algorithms and emphasized the importance of adaptive input distribution and cooperative receiver design.

To support massive RIScatter networks with large number of nodes and states, one possible future direction is to consider backscatter detection over the received signal domain rather than energy domain, where multi-antenna [119] and learning-based approaches can be promising. Another interesting question is how to design RIScatter nodes and receivers in a multi-user system to fully exploit the dynamic passive beamforming that naturally origins from backscatter modulation.
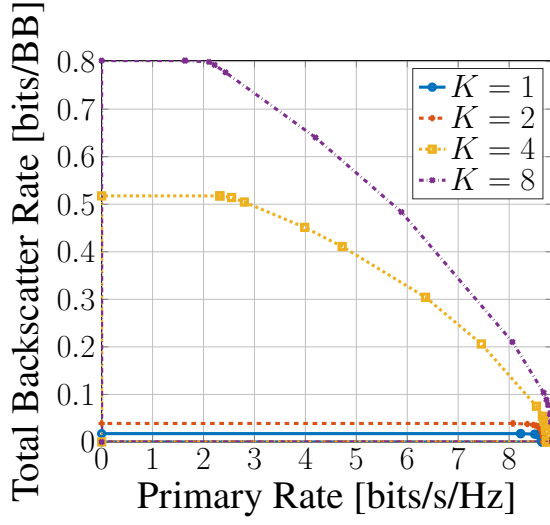
(a) RIScatter Nodes
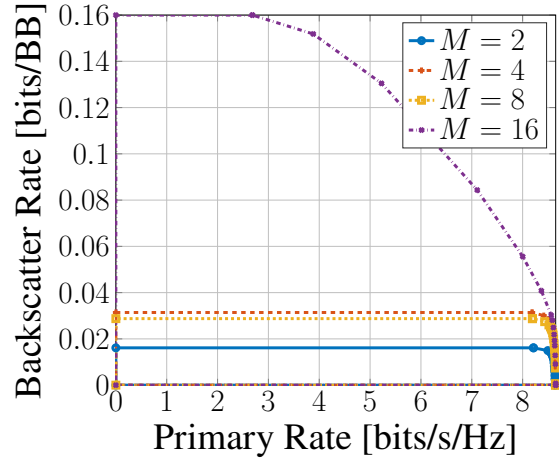
(b) Reflection States
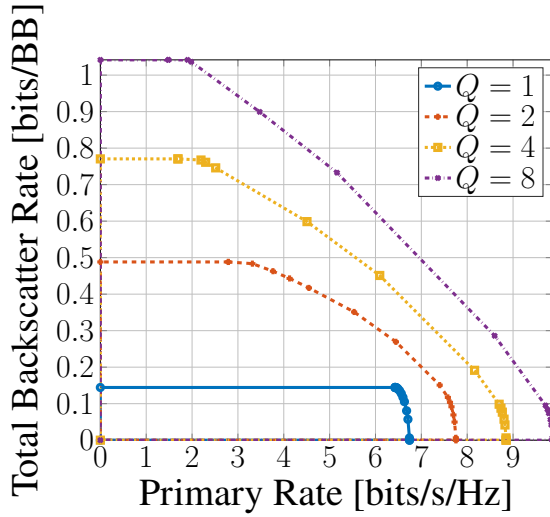
(c) Transmit Antennas
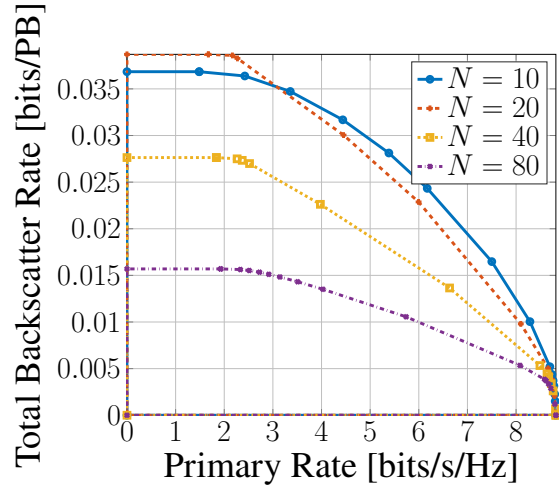
(d) Spreading Factor
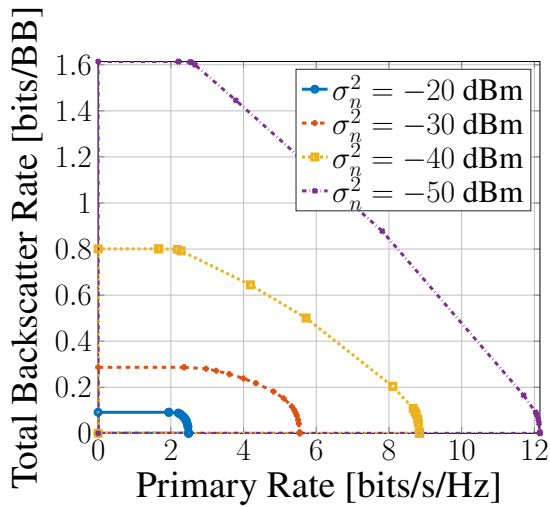
(e) Average Noise Power
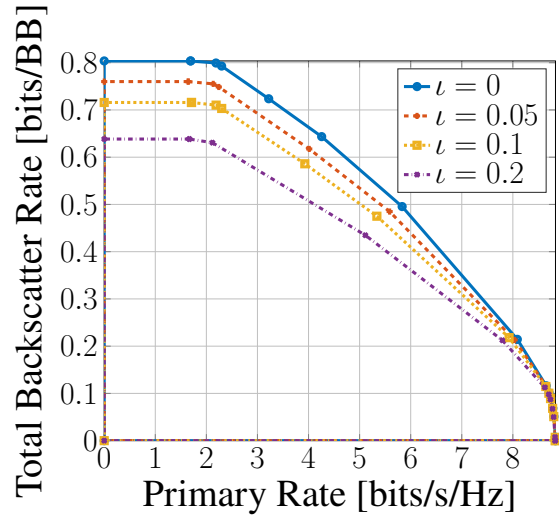
(f) Imperfect CSI
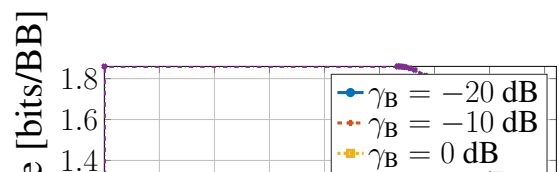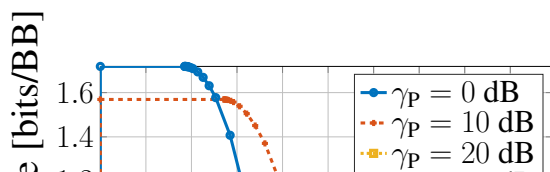
Chapter 5

Channel Shaping and Interference Alignment using RIS: From Diagonal to Beyond

5.1 Introduction

Today we are witnessing a paradigm shift from connectivity to intelligence, where the wireless environment is no longer a chaotic medium but a conscious agent that serves on demand. This is empowered by the recent advances in RIS, a real-time programmable metasurface of numerous non-resonant sub-wavelength scattering elements. It can manipulate the amplitude, phase, frequency, and polarization of the scattered waves [120] with a higher energy efficiency, lower cost, lighter footprint, and greater scalability than relays. Using RIS for passive beamforming has attracted significant interest in wireless communication [25, 50, 79, 121], backscatter [122, 97], sensing [123, 124], and power transfer literature [81, 77, 78], reporting a second-order array gain and fourth-order power scaling law (with proper waveform). On the other hand, RIS also enables backscatter modulation by dynamically switching between different patterns, as already investigated [85, 92, 125] and prototyped [83, 84]. Despite fruitful outcomes, one critical unanswered question is the channel shaping capability: *To what extent can a passive RIS reshape the wireless channel?*

The answer indeed depends on the hardware architecture and scattering model. In conventional (a.k.a. diagonal) RIS, each scattering element is tuned by a dedicated impedance and acts as an *individual* phase shifter [31]. The concept is generalized to Beyond-Diagonal (BD)-RIS [51, 126] which groups adjacent elements using passive components. This allows *cooperative* scattering — wave impinging on one element can propagate within the circuit

and depart partially from any element in the same group. BD-RIS can thus control both amplitude and phase of the reflected wave, generalizing the scattering matrix from diagonal with unit-magnitude entries to block diagonal with unitary blocks. Its benefit has been recently shown in receive power maximization [127–130], transmit power minimization [131], and rate maximization [131, 130, 132–134]. Practical issues such as channel estimation [135] and mutual coupling [136] have also been investigated. Therefore, BD-RIS is envisioned as the next generation channel shaper with stronger signal processing flexibility [137].

Channel shaping is different from passive beamforming as it seeks to modify the inherent properties of the channel itself. This allows one to decouple the RIS-transceiver design and explore the fundamental limits of channel manipulation. For example, diagonal RIS has been proved useful for improving channel power [138], degree of freedom [139, 140], condition number [141, 142], and effective rank [143, 144] in Multiple-Input Multiple-Output (MIMO). In contrast, BD-RIS can provide a higher channel power but existing results are limited to Single-Input Single-Output (SISO)[1]. [127] and MISO [128]. While these studies offer promising glimpses into the channel shaping potential, a comprehensive understanding of the capabilities and limitations is desired, and a universal design framework is missing. This paper aims to answer the channel shaping question through theoretical analysis and numerical optimization. The contributions are summarized below.

First, we quantify the capability of a BD-RIS to reshape the MIMO point-to-point channel in terms of singular values. The *Pareto frontiers* are characterized by optimizing the weighted sum of singular values, where the weights can be positive, zero, or negative. The resulting singular value region generalizes most relevant metrics and provides an intuitive channel shaping benchmark. We then discuss some analytical singular value bounds in rank-deficient and fully-connected scenarios, which help to demystify the gain from off-diagonal entries. This is the first paper to answer the channel shaping question and highlight the BD-RIS gain from a Pareto perspective.

Second, we propose a Riemannian Conjugate Gradient (RCG) algorithm adapted from [145, 146] for smooth optimization problems of asymmetric BD-RIS with arbitrary group size. Specifically, block-wise update is performed along the geodesics[2] of the Stiefel manifold, which are expressed compactly by the exponential map [147]. It features lower complexity and faster convergence than general manifold optimization [148, 149], and solves the Pareto singular value problem. This is the first paper to tailor an efficient optimization framework for asymmetric BD-RIS.

---

[1]In terms of channel shaping, single-stream MIMO with given precoder and combiner [127] is equivalent to SISO.

[2]A geodesic refers to the shortest path between two points in a Riemannian manifold.

Third, we tackle BD-RIS MIMO rate maximization with two solutions: a local-optimal approach through Alternating Optimization (AO) and a low-complexity approach over channel shaping. The former updates active and passive beamformers by eigenmode transmission and RCG algorithm, respectively. The latter suboptimally decouples both blocks, recasts the shaping problem as channel power maximization, and solves it iteratively in closed form. Interestingly, the gap in between vanishes as BD-RIS evolves from diagonal (single-connected) to unitary (fully-connected). It suggests channel shaping offers a promising low-complexity solution for joint RIS-transceiver designs.

Fourth, extensive simulations reveal that the performance gain from BD-RIS increases with group size and MIMO dimensions. In terms of channel power, fully-connected BD-RIS boosts up to 62% and 270% over diagonal RIS in 1×1 and 4×4 MIMO under independent Rayleigh fading, respectively. The superiority stems from stronger *subchannel rearrangement* and *subspace alignment* capabilities empowered by in-group cooperation. It emphasizes the importance of using BD-RIS in large-scale MIMO systems.

5.2 Beyond-Diagonal-Reconfigurable Intelligent Surface Model

Consider a BD-RIS aided point-to-point MIMO system with N_T, N_S, N_R transmit, scatter, and receive antennas, respectively. This configuration is denoted as $N_\mathrm{T} \times N_\mathrm{S} \times N_\mathrm{R}$ in the following context. The BD-RIS can be modeled as an N_S-port network [150] that divides into G individual groups, each containing $L \triangleq N_\mathrm{S}/G$ elements interconnected by real-time reconfigurable components [51]. To simplify the analysis, we assume a lossless asymmetric network[3] without mutual coupling between scatter elements, as previously considered in [126, 134, 133]. The overall scattering matrix of the BD-RIS is

$$\boldsymbol{\Theta} = \mathrm{diag}(\boldsymbol{\Theta}_1, \ldots, \boldsymbol{\Theta}_G), \tag{5.1}$$

where $\boldsymbol{\Theta}_g \in \mathbb{U}^{L \times L}$ is a unitary matrix that describes the response of group $g \in \mathcal{G} \triangleq \{1, \ldots, G\}$. That is, $\boldsymbol{\Theta}_g = \boldsymbol{\Theta}_g^\mathsf{H}$ and $\boldsymbol{\Theta}_g^\mathsf{H} \boldsymbol{\Theta}_g = \mathbf{I}$. Note that diagonal (single-connected) and unitary (fully-connected) RIS can be regarded as its extreme cases with group size $L = 1$ and $L = N_\mathrm{S}$, respectively. Some potential physical architectures of BD-RIS are illustrated in [51,

---

[3]While symmetric BD-RIS (involving capacitors and inductors) is often considered in the literature [51, 127–133], asymmetric BD-RIS can be built over reconfigurable asymmetric passive components (e.g., ring hybrids and branch-line hybrids) [151].

Fig. 3], [134, Fig. 5], and [130, Fig. 2], where the radiation pattern and circuit topology have impacts on the scattering matrix.

Let $\mathbf{H}_\mathrm{D} \in \mathbb{C}^{N_\mathrm{R} \times N_\mathrm{T}}$, $\mathbf{H}_\mathrm{B} \in \mathbb{C}^{N_\mathrm{R} \times N_\mathrm{S}}$, $\mathbf{H}_\mathrm{F} \in \mathbb{C}^{N_\mathrm{S} \times N_\mathrm{T}}$ denote the direct (transmitter-receiver), backward (RIS-receiver), and forward (transmitter-RIS) channels, respectively. The equivalent channel is a function of the scattering matrix

$$\mathbf{H} = \mathbf{H}_\mathrm{D} + \mathbf{H}_\mathrm{B}\boldsymbol{\Theta}\mathbf{H}_\mathrm{F} = \mathbf{H}_\mathrm{D} + \sum_g \mathbf{H}_{\mathrm{B},g}\boldsymbol{\Theta}_g\mathbf{H}_{\mathrm{F},g}, \qquad (5.2)$$

where $\mathbf{H}_{\mathrm{B},g} \in \mathbb{C}^{N_\mathrm{R} \times L}$ and $\mathbf{H}_{\mathrm{F},g} \in \mathbb{C}^{L \times N_\mathrm{T}}$ are the backward and forward subchannels for RIS group g, corresponding to the $(g-1)L$ to gL columns of $\mathbf{H}_\mathrm{B}$ and rows of $\mathbf{H}_\mathrm{F}$, respectively. Since unitary matrices constitute an algebraic group with respect to multiplication, the scattering matrix of group g can be decomposed as

$$\boldsymbol{\Theta}_g = \mathbf{L}_g\mathbf{R}_g^\mathsf{H}, \qquad (5.3)$$

where $\mathbf{L}_g, \mathbf{R}_g \in \mathbb{U}^{L \times L}$ are two unitary factor matrices. Let $\mathbf{H}_{\mathrm{B},g} = \mathbf{U}_{\mathrm{B},g}\boldsymbol{\Sigma}_{\mathrm{B},g}\mathbf{V}_{\mathrm{B},g}^\mathsf{H}$ and $\mathbf{H}_{\mathrm{F},g} = \mathbf{U}_{\mathrm{F},g}\boldsymbol{\Sigma}_{\mathrm{F},g}\mathbf{V}_{\mathrm{F},g}^\mathsf{H}$ be the compact Singular Value Decomposition (SVD) of the backward and forward channels, respectively. The equivalent channel can thus be rewritten as

$$\mathbf{H} = \overbrace{\mathbf{H}_\mathrm{D} + \sum_g \mathbf{U}_{\mathrm{B},g}\boldsymbol{\Sigma}_{\mathrm{B},g}}^{\text{direct-indirect}} \underbrace{\mathbf{V}_{\mathrm{B},g}^\mathsf{H}\mathbf{L}_g\mathbf{R}_g^\mathsf{H}\mathbf{U}_{\mathrm{F},g}}_{\text{backward-forward}} \boldsymbol{\Sigma}_{\mathrm{F},g}\mathbf{V}_{\mathrm{F},g}^\mathsf{H}. \qquad (5.4)$$

Remark 10. *By analyzing* (5.4)*, we conclude that channel shaping through BD-RIS creates two critical opportunities:*

- *Subspace alignment: each group can align the singular matrices of the backward-forward (intra-group, multiplicative) and the direct-indirect (inter-group, additive) channels. In SISO, subspace alignment boils down to phase matching and the optimal scattering matrix of group g is*

$$\boldsymbol{\Theta}_g^\star = \exp\big(\jmath\arg(h_\mathrm{D})\big)\mathbf{V}_{\mathrm{B},g}\mathbf{U}_{\mathrm{F},g}^\mathsf{H}, \qquad (5.5)$$

where $\mathbf{V}_{\mathrm{B},g} = \big[\mathbf{h}_{\mathrm{B},g}/\|\mathbf{h}_{\mathrm{B},g}\|, \mathbf{N}_{\mathrm{B},g}\big]$, $\mathbf{U}_{\mathrm{F},g} = \big[\mathbf{h}_{\mathrm{F},g}/\|\mathbf{h}_{\mathrm{F},g}\|, \mathbf{N}_{\mathrm{F},g}\big]$, and $\mathbf{N}_{\mathrm{B},g}, \mathbf{N}_{\mathrm{F},g} \in \mathbb{C}^{L \times (L-1)}$ are the orthonormal bases of the null spaces of $\mathbf{h}_{\mathrm{B},g}$ and $\mathbf{h}_{\mathrm{F},g}$, respectively. Diagonal RIS is thus sufficient for perfect SISO phase matching (with empty null spaces), but its disadvantage in subspace alignment scales with MIMO dimensions, since each element can only apply a common phase shift to the "pinhole" indirect channel of

size $N_\mathrm{R} \times N_\mathrm{T}$ passing through itself. Even if the BD-RIS is fully-connected, there still exists a tradeoff between the direct-indirect and backward-forward alignments.

- ***Subchannel rearrangement:*** *this unique property of BD-RIS allows each group to rearrange and combine the backward and forward subchannels by strength. In SISO, diagonal RIS provides a maximum indirect channel amplitude of $\sum_{n=1}^{N_\mathrm{S}} |h_{\mathrm{B},n}||h_{\mathrm{F},n}|$, while BD-RIS can generalize it to $\sum_{g=1}^{G} \sum_{l=1}^{L} |h_{\mathrm{B},\pi_{\mathrm{B},g}(l)}||h_{\mathrm{F},\pi_{\mathrm{F},g}(l)}|$, where $\pi_{\mathrm{B},g}$ and $\pi_{\mathrm{F},g}$ are permutations of $\mathcal{L} \triangleq \{1,\dots,L\}$. By rearrangement inequality, the maximum is attained by pairing the l-th strongest backward and forward subchannels in each group. The advantage of BD-RIS in subchannel rearrangement scales with MIMO dimensions, since the number of subchannels associated with each group grows with $N_\mathrm{R} \times N_\mathrm{T}$.*

5.3 Channel Singular Values Redistribution

5.3.1 A Toy Example

We first illustrate the channel shaping capabilities of different RIS by a toy example. Consider a $2 \times 2 \times 2$ setup where the direct link is blocked. The diagonal RIS is modeled by $\boldsymbol{\Theta}_\mathrm{D} = \mathrm{diag}(e^{\jmath\theta_1}, e^{\jmath\theta_2})$ while the unitary BD-RIS has 4 independent angular parameters

$$\boldsymbol{\Theta}_\mathrm{U} = e^{\jmath\phi} \begin{bmatrix} e^{\jmath\alpha}\cos\psi & e^{\jmath\beta}\sin\psi \\ -e^{-\jmath\beta}\sin\psi & e^{-\jmath\alpha}\cos\psi \end{bmatrix}. \tag{5.6}$$

In particular, ϕ has no impact on the singular value because $\mathrm{sv}(e^{\jmath\phi}\mathbf{A}) = \mathrm{sv}(\mathbf{A})$. We also enforce symmetry by $\beta = \pi/2$ such that both architectures have the same number of angular parameters. Fig. 5.1 shows the channel singular values achieved by an exhaustive grid search over (θ_1, θ_2) for diagonal RIS and (α, ψ) for symmetric unitary RIS. It is observed that both singular values can be manipulated up to 9% using diagonal RIS and 42% using symmetric BD-RIS, despite both architectures have the same number of scattering elements and design parameters. A larger performance gap is expected when asymmetric BD-RIS is available. This example shows BD-RIS can provide a wider dynamic range of channel singular values and motivates further studies on channel shaping.
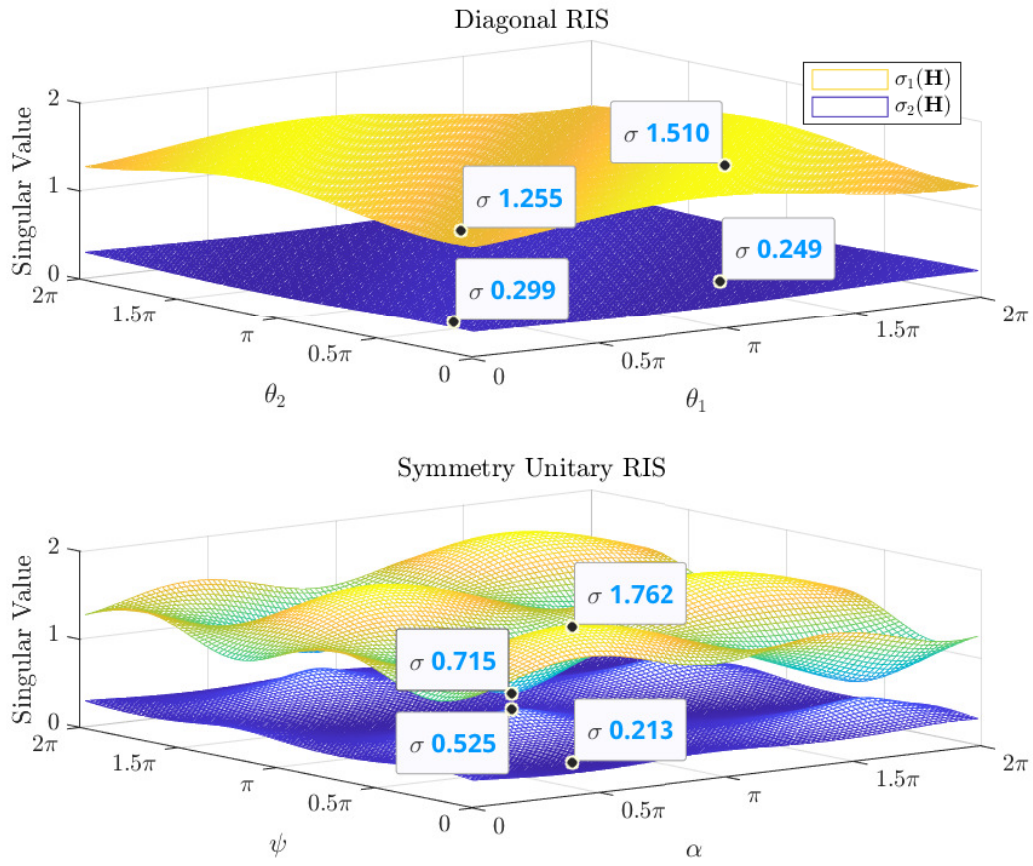
Fig. 5.1 $2 \times 2 \times 2$ (no direct) channel singular value shaping by diagonal and symmetry unitary RIS.

5.3.2   Pareto Frontier Characterization

We then characterize the Pareto frontier of channel singular values by maximizing their weighted sum

$$\max_{\boldsymbol{\Theta}} \quad \sum_n \rho_n \sigma_n(\mathbf{H}) \tag{5.7a}$$

$$\text{s.t.} \quad \boldsymbol{\Theta}_g^{\mathsf{H}} \boldsymbol{\Theta}_g = \mathbf{I}, \quad \forall g, \tag{5.7b}$$

where $n \in \{1, \dots, N \triangleq \min(N_{\mathrm{T}}, N_{\mathrm{R}})\}$ and ρ_n is the weight of the n-th singular value that can be positive, zero, or negative. Varying $\{\rho_n\}$ unveils the entire achievable singular value region. Thus, the Pareto frontier problem (5.7) generalizes most relevant metrics and provides a powerful shaping framework. The objective (5.7a) is smooth in $\boldsymbol{\Theta}$ and the feasible domain (5.7b) for group g corresponds to the Stiefel manifold. Next, we zoom out to general smooth maximization problems of asymmetric BD-RIS.

Inspired by [145, 146], we propose a block-wise RCG algorithm along the geodesics on the Lie group of unitary matrices $\mathbb{U}^{L \times L}$. It leverages the fact that unitary matrices are closed under multiplication. At iteration r, the gradient is computed in the Euclidean space and translated to the Riemannian manifold [148]

$$\nabla_{\mathrm{E},g}^{(r)} = \frac{\partial f(\boldsymbol{\Theta}_g^{(r)})}{\partial \boldsymbol{\Theta}_g^*}, \tag{5.8}$$

$$\nabla_{\mathrm{R},g}^{(r)} = \nabla_{\mathrm{E},g}^{(r)} \boldsymbol{\Theta}_g^{(r)\mathsf{H}} - \boldsymbol{\Theta}_g^{(r)} \nabla_{\mathrm{E},g}^{(r)\,\mathsf{H}}. \tag{5.9}$$

The Polak-Ribierre parameter [152] is approximated as [146]

$$\gamma_g^{(r)} = \frac{\mathrm{tr}\big((\nabla_{\mathrm{R},g}^{(r)} - \nabla_{\mathrm{R},g}^{(r-1)})\nabla_{\mathrm{R},g}^{(r)\,\mathsf{H}}\big)}{\mathrm{tr}\big(\nabla_{\mathrm{R},g}^{(r-1)}\nabla_{\mathrm{R},g}^{(r-1)\,\mathsf{H}}\big)}, \tag{5.10}$$

and the conjugate direction is

$$\mathbf{D}_g^{(r)} = \nabla_{\mathrm{R},g}^{(r)} + \gamma_g^{(r)} \mathbf{D}_g^{(r-1)}. \tag{5.11}$$

In the Stiefel manifold, the geodesic emanating from $\boldsymbol{\Theta}_g^{(r)}$ with velocity $\mathbf{D}_g^{(r)}$ and step size μ is described compactly by the exponential map [147]

$$\mathbf{G}_g^{(r)}(\mu) = \exp(\mu \mathbf{D}_g^{(r)})\boldsymbol{\Theta}_g^{(r)}. \tag{5.12}$$

An appropriate $\mu^\star$ can be obtained by the Armijo rule [153].[4] Finally, the scattering matrix is updated along the geodesic as

$$\boldsymbol{\Theta}_g^{(r+1)} = \mathbf{G}_g^{(r)}(\mu^\star). \tag{5.13}$$

Algorithm 8 summarizes the proposed block-wise geodesic RCG method for smooth maximization problems of asymmetric BD-RIS. Convergence to stationary points is guaranteed.

Remark 11. *Compared with universal manifold optimization [148, 149], Algorithm 8 inherits a trifold benefit from [145, 146]:*

1. *No retraction thanks to rotational update* (5.12), (5.13)*;*

2. *Lower computational complexity per iteration;*

3. *Faster convergence thanks to proper parameter space.*

Lemma 1. *The Euclidean gradient of* (5.7a) *w.r.t. BD-RIS group g is*

$$\frac{\partial \sum_n \rho_n \sigma_n(\mathbf{H})}{\partial \boldsymbol{\Theta}_g^*} = \mathbf{H}_{\mathrm{B},g}^{\mathsf{H}} \mathbf{U} \operatorname{diag}(\rho_1, \dots, \rho_N) \mathbf{V}^{\mathsf{H}} \mathbf{H}_{\mathrm{F},g}^{\mathsf{H}}, \tag{5.14}$$

where $\mathbf{U}$ and $\mathbf{V}$ are the left and right singular matrices of $\mathbf{H}$, respectively.

Proof. Please refer to Appendix 6.3.1. □

Algorithm 8 can thus be invoked for the Pareto singular value problem (5.7) where line 4 uses (5.14) explicitly.

5.3.3   Some Analytical Bounds

We then discuss some analytical bounds related to channel singular values.

Proposition 7 (degree of freedom)**.** *In point-to-point MIMO, BD-RIS cannot achieve a higher Degree of Freedom (DoF) than diagonal RIS.*

Proof. Please refer to Appendix 6.3.2. □

---

[4]To double the step size, one only need to square the rotation matrix instead of recomputing the matrix exponential, i.e., $\exp(2\mu \mathbf{D}_g^{(r)}) = \exp^2(\mu \mathbf{D}_g^{(r)})$.

Algorithm 8 Block-wise geodesic RCG for asymmetric BD-RIS

Input: $f(\Theta)$, G
Output: $\Theta^\star$
1: **Initialize** $r \leftarrow 0$, $\Theta^{(0)}$
2: **Repeat**
3:     **For** $g \leftarrow 1$ to G
4:         $\nabla_{\mathrm{E},g}^{(r)} \leftarrow$ (5.8)
5:         $\nabla_{\mathrm{R},g}^{(r)} \leftarrow$ (5.9)
6:         $\gamma_g^{(r)} \leftarrow$ (5.10)
7:         $\mathbf{D}_g^{(r)} \leftarrow$ (5.11)
8:         **If** $\Re\{\mathrm{tr}(\mathbf{D}_g^{(r)\mathsf{H}} \nabla_{\mathrm{R},g}^{(r)})\} < 0$ ▷ not an ascent direction
9:             $\mathbf{D}_g^{(r)} \leftarrow \nabla_{\mathrm{R},g}^{(r)}$
10:       **End If**
11:       $\mu \leftarrow 1$
12:       $\mathbf{G}_g^{(r)}(\mu) \leftarrow$ (5.12)
13:       **While** $f\big(\mathbf{G}_g^{(r)}(2\mu)\big) - f(\Theta_g^{(r)}) \geq \mu \cdot \mathrm{tr}(\mathbf{D}_g^{(r)}\mathbf{D}_g^{(r)\mathsf{H}})/2$
14:          $\mu \leftarrow 2\mu$
15:       **End While**
16:       **While** $f\big(\mathbf{G}_g^{(r)}(\mu)\big) - f(\Theta_g^{(r)}) < \mu/2 \cdot \mathrm{tr}(\mathbf{D}_g^{(r)}\mathbf{D}_g^{(r)\mathsf{H}})/2$
17:          $\mu \leftarrow \mu/2$
18:       **End While**
19:       $\Theta_g^{(r+1)} \leftarrow$ (5.13)
20:     **End For**
21:     $r \leftarrow r + 1$
22: **Until** $|f(\Theta^{(r)}) - f(\Theta^{(r-1)})|/f(\Theta^{(r-1)}) \leq \epsilon$

Proposition 8 (rank-deficient channel). *If the forward or backward channel is rank-k, then regardless of the RIS size and architecture, the n-th singular value of the equivalent channel is bounded by*

$$\sigma_n(\mathbf{H}) \leq \sigma_{n-k}(\mathbf{T}), \qquad\qquad \textit{if } n > k, \qquad\qquad (5.15)$$

$$\sigma_n(\mathbf{H}) \geq \sigma_n(\mathbf{T}), \qquad\qquad \textit{if } n < N - k + 1, \qquad\qquad (5.16)$$

where

$$\mathbf{T}\mathbf{T}^{\mathsf{H}} = \begin{cases} \mathbf{H}_{\mathrm{D}}(\mathbf{I} - \mathbf{V}_{\mathrm{F}}\mathbf{V}_{\mathrm{F}}^{\mathsf{H}})\mathbf{H}_{\mathrm{D}}^{\mathsf{H}}, & \textit{if } \mathrm{rank}(\mathbf{H}_{\mathrm{F}}) = k, \\ \mathbf{H}_{\mathrm{D}}^{\mathsf{H}}(\mathbf{I} - \mathbf{U}_{\mathrm{B}}\mathbf{U}_{\mathrm{B}}^{\mathsf{H}})\mathbf{H}_{\mathrm{D}}, & \textit{if } \mathrm{rank}(\mathbf{H}_{\mathrm{B}}) = k, \end{cases} \qquad (5.17)$$

and $\mathbf{V}_{\mathrm{F}}$ and $\mathbf{U}_{\mathrm{B}}$ are the right and left compact singular matrices of $\mathbf{H}_{\mathrm{F}}$ and $\mathbf{H}_{\mathrm{B}}$, respectively.

Proof. Please refer to Appendix 6.3.3.   □

Corollary 8.1 (extreme singular values)**.** *With a sufficiently large RIS, the first k channel singular values are unbounded above while the last k channel singular values can be suppressed to zero.*

Corollary 8.2 (LoS channel[5])**.** *If the forward or backward channel is LoS, then a RIS can at most enlarge (resp. suppress) the n-th ($n \geq 2$) channel singular value to the $(n-1)$-th (resp. n-th) singular value of $\mathbf{T}$, that is,*

$$\sigma_1(\mathbf{H}) \geq \sigma_1(\mathbf{T}) \geq \sigma_2(\mathbf{H}) \geq \ldots \geq \sigma_{N-1}(\mathbf{T}) \geq \sigma_N(\mathbf{H}) \geq \sigma_N(\mathbf{T}). \quad (5.18)$$

In Section 5.5, we will show by simulation that a finite-size BD-RIS can approach those bounds better than diagonal RIS.

Proposition 9 (fully-connected RIS without direct link)**.** *If the BD-RIS is fully-connected and the direct link is absent, then the channel singular values can be manipulated up to*

$$\mathrm{sv}(\mathbf{H}) = \mathrm{sv}(\mathbf{BF}), \quad (5.19)$$

where $\mathbf{B}$ and $\mathbf{F}$ are arbitrary matrices with the same singular values as $\mathbf{H}_\mathrm{B}$ and $\mathbf{H}_\mathrm{F}$, respectively,

Proof. Please refer to Appendix 6.3.4. $\qquad \square$

The problem now becomes how the singular values of matrix product are bounded by the singular values of its individual factors. Let $N' = \max(N_\mathrm{T}, N_\mathrm{S}, N_\mathrm{R})$ and $\sigma_n(\mathbf{H}) = \sigma_n(\mathbf{H}_\mathrm{F}) = \sigma_n(\mathbf{H}_\mathrm{B}) = 0$ for $N < n \leq N'$. We have the following corollaries.

Corollary 9.1 (generic singular value bounds [155])**.**

$$\prod_{k \in K} \sigma_k(\mathbf{H}) \leq \prod_{i \in I} \sigma_i(\mathbf{H}_\mathrm{B}) \prod_{j \in J} \sigma_j(\mathbf{H}_\mathrm{F}), \quad (5.20)$$

for all admissible triples $(I, J, K) \in T_r^{N'}$ with $r < N'$, where

$$T_r^{N'} \triangleq \Big\{ (I, J, K) \in U_r^{N'} \mid \forall p < r, (F, G, H) \in T_p^r,$$
$$\sum_{f \in F} i_f + \sum_{g \in G} j_g \leq \sum_{h \in H} k_h + p(p+1)/2 \Big\},$$

$$U_r^{N'} \triangleq \Big\{ (I, J, K) \mid \sum_{i \in I} i + \sum_{j \in J} j = \sum_{k \in K} k + r(r+1)/2 \Big\}.$$

---

[5]A similar result has been derived for diagonal RIS in [154].

Corollary 9.2 (upper bound on the largest singular value)**.**

$$\sigma_1(\mathbf{H}) \leq \sigma_1(\mathbf{H}_B)\sigma_1(\mathbf{H}_F). \tag{5.21}$$

Corollary 9.3 (upper bound on the product of first k singular values)**.**

$$\prod_{n=1}^{k} \sigma_n(\mathbf{H}) \leq \prod_{n=1}^{k} \sigma_n(\mathbf{H}_B) \prod_{n=1}^{k} \sigma_n(\mathbf{H}_F). \tag{5.22}$$

Corollary 9.4 (upper bound on the sum of first k singular values to the power of p)**.**

$$\sum_{n=1}^{k} \sigma_n^p(\mathbf{H}) \leq \sum_{n=1}^{k} \sigma_n^p(\mathbf{H}_B)\sigma_n^p(\mathbf{H}_F), \quad p > 0. \tag{5.23}$$

When $k = N'$ and $p = 2$, (5.23) suggests the channel power is upper bounded by the sum of (sorted) element-wise power product of backward and forward subchannels.

Tight bounds are inapplicable when a MIMO direct link is present, as the RIS needs to balance the direct-indirect (additive) and backward-forward (multiplicative) subspace alignments. Such a balance often involves optimization approaches and another example will be discussed in Section 5.4.2.

5.4 Achievable Rate Maximization

The MIMO achievable rate maximization problem is formulated w.r.t. joint active and passive beamforming

$$\max_{\mathbf{W},\mathbf{\Theta}} \quad R = \log\det\left(\mathbf{I} + \frac{\mathbf{W}^H\mathbf{H}^H\mathbf{H}\mathbf{W}}{\eta}\right) \tag{5.24a}$$

$$\text{s.t.} \quad \|\mathbf{W}\|_F^2 \leq P, \tag{5.24b}$$

$$\mathbf{\Theta}_g^H\mathbf{\Theta}_g = \mathbf{I}, \quad \forall g, \tag{5.24c}$$

where $\mathbf{W}$ is the transmit precoder, R is the achievable rate, η is the noise power, and P is the transmit power budget. Two methods are proposed below to solve problem (5.24).

5.4.1 Alternating Optimization

Consider an AO approach that updates $\boldsymbol{\Theta}$ and $\mathbf{W}$ iteratively. For a given $\mathbf{W}$, the passive beamforming subproblem is

$$\max_{\boldsymbol{\Theta}} \quad \log\det\left(\mathbf{I} + \frac{\mathbf{HQH}^{\mathsf{H}}}{\eta}\right) \tag{5.25a}$$

$$\text{s.t.} \quad \boldsymbol{\Theta}_g^{\mathsf{H}}\boldsymbol{\Theta}_g = \mathbf{I}, \quad \forall g, \tag{5.25b}$$

where $\mathbf{Q} \triangleq \mathbf{WW}^{\mathsf{H}}$ is the transmit covariance matrix.

Lemma 2. *The Euclidean gradient of* (5.25a) *w.r.t. BD-RIS block g is*

$$\frac{\partial R}{\partial \boldsymbol{\Theta}_g^*} = \frac{1}{\eta}\mathbf{H}_{\mathrm{B},g}^{\mathsf{H}}\left(\mathbf{I} + \frac{\mathbf{HQH}^{\mathsf{H}}}{\eta}\right)^{-1}\mathbf{HQH}_{\mathrm{F},g}^{\mathsf{H}}. \tag{5.26}$$

Proof. Please refer to Appendix 6.3.5.   □

Algorithm 8 is then invoked to solve problem (5.24) where line 4 uses (5.26) explicitly. Since (5.25a) is a concave function of $\boldsymbol{\Theta}$, convergence to local-optimal points is guaranteed. On the other hand, the global optimal transmit precoder for a fixed $\boldsymbol{\Theta}$ is given by the eigenmode transmission [156]

$$\mathbf{W}^{\star} = \mathbf{VS}^{\star 1/2}, \tag{5.27}$$

where $\mathbf{V}$ is the right channel singular matrix and $\mathbf{S}^{\star}$ is the optimal water-filling power allocation matrix. The overall AO algorithm converges to local-optimal points of problem (5.24) since each subproblem is solved optimally and the objective is bounded above.

5.4.2 Low-Complexity Solution

We then propose a low-complexity solution to problem (5.24) based on channel shaping. The passive beamforming subproblem (5.25) involves transmit covariance matrix $\mathbf{Q}$ and thus requires iterative RCG update. Instead, we decouple the joint RIS-transceiver design by recasting (5.25) as channel power maximization

$$\max_{\boldsymbol{\Theta}} \quad \|\mathbf{H}_{\mathrm{D}} + \mathbf{H}_{\mathrm{B}}\boldsymbol{\Theta}\mathbf{H}_{\mathrm{F}}\|_{\mathrm{F}}^2 \tag{5.28a}$$

$$\text{s.t.} \quad \boldsymbol{\Theta}_g^{\mathsf{H}}\boldsymbol{\Theta}_g = \mathbf{I}, \quad \forall g. \tag{5.28b}$$

Remark 12. *As mentioned in Section 5.3.3, the key of solving* (5.28) *is to balance the additive and multiplicative subspace alignments. Problem* (5.28) *is very similar (in terms of*

maximizing the inner product of $\mathbf{H}_D$ *and* $\mathbf{H}_B \boldsymbol{\Theta} \mathbf{H}_F$*) to the weighted orthogonal Procrustes problem [157]*

$$\min_{\boldsymbol{\Theta}} \quad \|\mathbf{H}_D - \mathbf{H}_B \boldsymbol{\Theta} \mathbf{H}_F\|_F^2 \tag{5.29a}$$

$$\text{s.t.} \quad \boldsymbol{\Theta}^H \boldsymbol{\Theta} = \mathbf{I}, \tag{5.29b}$$

which has no trivial solution. One lossy transformation, by moving $\boldsymbol{\Theta}$ *to one side [158], formulates standard orthogonal Procrustes problems*

$$\min_{\boldsymbol{\Theta}} \quad \|\mathbf{H}_B^\dagger \mathbf{H}_D - \boldsymbol{\Theta} \mathbf{H}_F\|_F^2 \text{ or } \|\mathbf{H}_D \mathbf{H}_F^\dagger - \mathbf{H}_B \boldsymbol{\Theta}\|_F^2 \tag{5.30a}$$

$$\text{s.t.} \quad \boldsymbol{\Theta}^H \boldsymbol{\Theta} = \mathbf{I}, \tag{5.30b}$$

which has global optimal solutions

$$\boldsymbol{\Theta}^\star = \mathbf{U} \mathbf{V}^H \tag{5.31}$$

where $\mathbf{U}$ *and* $\mathbf{V}$ *are the left and right singular matrices of* $\mathbf{H}_B^\dagger \mathbf{H}_D \mathbf{H}_F^H$ *or* $\mathbf{H}_B^H \mathbf{H}_D \mathbf{H}_F^\dagger$ *[38]. This suboptimal solution only applies to fully-connected BD-RIS.*

Inspired by [159], we propose a general solution to problem (5.28) with arbitrary group size. The idea is to successively approximate the quadratic objective (5.28a) by local Taylor expansions and solve each step in closed form.

Proposition 10. *Starting from any* $\boldsymbol{\Theta}^{(0)} \in \mathbb{U}^{N_S \times N_S}$*, the sequence*

$$\boldsymbol{\Theta}_g^{(r+1)} = \mathbf{U}_g^{(r)} \mathbf{V}_g^{(r)}, \quad \forall g. \tag{5.32}$$

converges to a stationary point of (5.28)*, where* $\mathbf{U}_g^{(r)}$ *and* $\mathbf{V}_g^{(r)}$ *are the left and right compact singular matrix of*

$$\mathbf{M}_g^{(r)} = \mathbf{H}_{B,g}^H \Big(\mathbf{H}_D + \mathbf{H}_B \text{diag}\big(\boldsymbol{\Theta}_{[1:g-1]}^{(r+1)}, \boldsymbol{\Theta}_{[g:G]}^{(r)}\big) \mathbf{H}_F \Big) \mathbf{H}_{F,g}^H \tag{5.33}$$

Proof. Please refer to Appendix 6.3.6. □

Once the channel shaping problem (5.28) is solved, the transmit precoder can be obtained by (5.27). This two-stage approach decouples both blocks and is computationally efficient.

Table 5.1 Average Performance of BD-RIS Designs

RCG path	$N_S = 16$			$N_S = 256$		
	Objective	Iterations	Time [s]	Objective	Iterations	Time [s]
Geodesic	4.355×10^{-3}	11.61	2.038×10^{-2}	1.164×10^{-2}	25.78	3.216
Non-geodesic	4.168×10^{-3}	169.5	1.420×10^{-1}	8.873×10^{-3}	278.1	27.81

5.5   Simulation Results

In this section, we provide numerical results to evaluate the proposed BD-RIS designs. Consider a distance-dependent path loss model $\Lambda(d) = \Lambda_0 d^{-\gamma}$ where Λ_0 is the reference path loss at distance $1\,\mathrm{m}$, d is the propagation distance, and γ is the path loss exponent. The small-scale fading model is $\mathbf{H} = \sqrt{\kappa/(1+\kappa)}\mathbf{H}_{\mathrm{LoS}} + \sqrt{1/(1+\kappa)}\mathbf{H}_{\mathrm{NLoS}}$, where κ is the Rician K-factor, $\mathbf{H}_{\mathrm{LoS}}$ is the deterministic LoS component, and $\mathbf{H}_{\mathrm{NLoS}} \sim \mathcal{CN}(\mathbf{0}, \mathbf{I})$ is the Rayleigh component. We set $\Lambda_0 = -30\,\mathrm{dB}$, $d_{\mathrm{D}} = 14.7\,\mathrm{m}$, $d_{\mathrm{F}} = 10\,\mathrm{m}$, $d_{\mathrm{B}} = 6.3\,\mathrm{m}$, $\gamma_{\mathrm{D}} = 3$, $\gamma_{\mathrm{F}} = 2.4$ and $\gamma_{\mathrm{B}} = 2$ for reference, which corresponds to a typical indoor environment with $\Lambda_{\mathrm{D}} = -65\,\mathrm{dB}$, $\Lambda_{\mathrm{F}} = -54\,\mathrm{dB}$, $\Lambda_{\mathrm{B}} = -46\,\mathrm{dB}$. The indirect path via RIS is thus $35\,\mathrm{dB}$ weaker than the direct path. $\kappa \to \infty$ is assumed for all channels unless otherwise specified.

5.5.1   Channel Singular Values Redistribution

Pareto Frontier

Fig. 5.2 shows the Pareto singular values of a 2T2R MIMO reshaped by a RIS. When the direct link is absent, the achievable regions in Fig. 5.2(a) are shaped like pizza slices. This is because $\sigma_1(\mathbf{H}) \geq \sigma_2(\mathbf{H}) \geq 0$ and there exists a tradeoff between aligning the two subspaces. We observe that the smallest singular value is enhanced up to 2×10^{-4} by diagonal RIS and 3×10^{-4} by fully-connected BD-RIS, corresponding to a $50\,\%$ gain. When the direct link is present, the shape of the singular value region depends heavily on the relative strength of the indirect link. In Fig. 5.2(b), a 32-element RIS is insufficient to compensate the $35\,\mathrm{dB}$ path loss imbalance and results in a limited singular value region that is symmetric around the direct point. As the group size L increases, the shape of the region evolves from elliptical to square. This transformation not only provides a better tradeoff in subchannel manipulation but also improves the dynamic range of $\sigma_1(\mathbf{H})$ and $\sigma_2(\mathbf{H})$ by $22\,\%$ and $38\,\%$, respectively. The achievable singular value region also enlarges as the number of scattering elements N_{S} increases. In particular, Fig. 5.2(d) shows that the equivalent channel can be completely nulled by a 128-element BD-RIS but not by a diagonal one. Those results demonstrate the

(a) $2 \times 32 \times 2$ (no direct)   (b) $2 \times 32 \times 2$

(c) $2 \times 64 \times 2$ (d) $2 \times 128 \times 2$
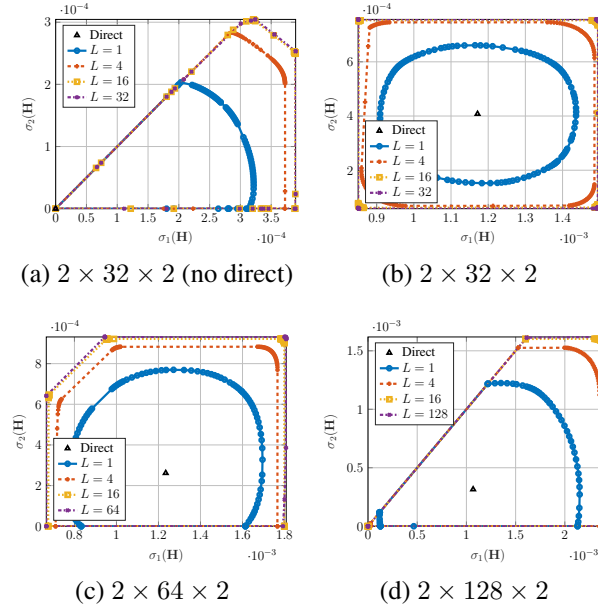
Fig. 5.2 Pareto frontiers of singular values of a 2T2R channel reshaped by a RIS.

superior channel shaping capability of BD-RIS for better signal enhancement and interference suppression.

Analytical Bounds and Numerical Results

Fig. 5.3 illustrates the analytical singular value bounds in Proposition 8 and the numerical results obtained by solving problem (5.7) with $\rho_n = \pm 1$ and $\rho_{n'} = 0$, $\forall n' \neq n$. Here we assme a rank-k forward channel without loss of generality. When the RIS is in the vicinity of the transmitter, Figs. 5.3(a) and 5.3(b) show that the achievable channel singular values indeed satisfy Corollary 8.2, namely $\sigma_1(\mathbf{H}) \geq \sigma_1(\mathbf{T})$, $\sigma_2(\mathbf{T}) \leq \sigma_2(\mathbf{H}) \leq \sigma_1(\mathbf{T})$, etc. It is obvious that BD-RIS can approach those bounds better than diagonal RIS especially for a small N_S. Another example is given in Fig. 5.3(c) with rank-2 forward channel. The first two channel singular values are unbounded above and bounded below by the first two singular values of $\mathbf{T}$, while the last two singular values can be suppressed to zero and bounded above by the first two singular values of $\mathbf{T}$. Those observations align with Proposition 8 and Corollary 8.1. Finally, Fig. 5.3(d) confirms there are no extra singular value bounds when both forward and backward channels are full-rank. This can be predicted from (5.17) where the compact singular matrix $\mathbf{V}_F$ becomes unitary and $\mathbf{T} = \mathbf{0}$. The numerical results are consistent with the analytical bounds, and we conclude that the channel shaping advantage of BD-RIS over diagonal RIS scales with forward and backward channel ranks.

(a) $4 \times 32 \times 4$ (rank-1)   (b) $4 \times 64 \times 4$ (rank-1)

(c) $4 \times 128 \times 4$ (rank-2)   (d) $4 \times 256 \times 4$ (rank-4)
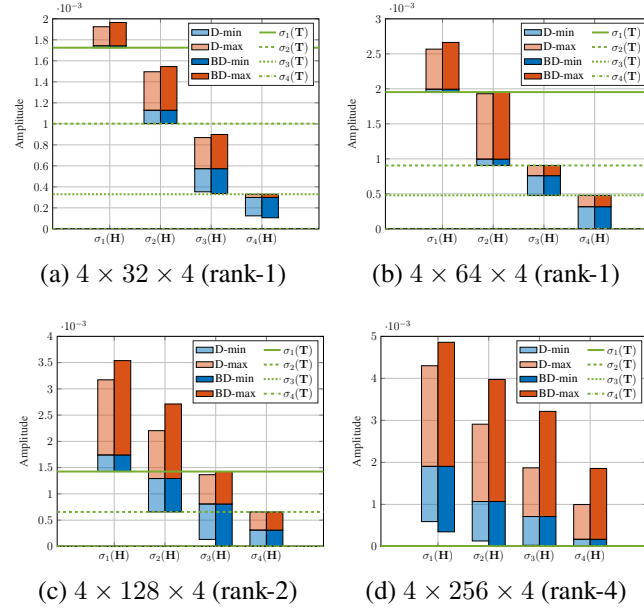
Fig. 5.3 Achievable channel singular values: analytical bounds (green lines) and numerical optimization results (blue and red bars). 'D' means diagonal RIS and 'BD' means fully-connected BD-RIS. 'rank-k' refers to the forward channel.

(a) $1 \times 256 \times 1$ (no direct)   (b) $4 \times 256 \times 4$ (no direct)
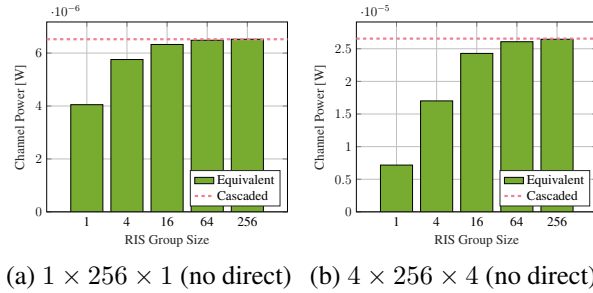
Fig. 5.4 Average maximum channel power versus BD-RIS group size and MIMO dimensions. 'Cascaded' refers to the available power of the cascaded channel, i.e., the sum of (sorted) element-wise power product of backward and forward subchannels.

Fig. 5.4 compares the analytical channel power bound in Corollary 9.4 with $k = N'$, $p = 2$ and the numerical results obtained by solving problem (5.28) when the direct link is absent. Here, a fully-connected BD-RIS can attain the upper bound either in closed form or via optimization approach (5.32). For the SISO case in Fig. 5.4(a), the maximum channel power is approximately 4×10^{-6} by diagonal RIS and 6.5×10^{-6} by fully-connected BD-RIS, corresponding to a $62.5\,\%$ gain. This aligns with the asymptotic BD-RIS scaling law derived for SISO in [51]. Interestingly, the gain surges to $270\,\%$ in 4T4R MIMO as shown in Fig. 5.4(b). This is because subspace alignment boils down to phase matching in SISO such that

(a) $16 \times N_{\mathrm{S}} \times 16$ (no direct)   (b) $16 \times N_{\mathrm{S}} \times 16$
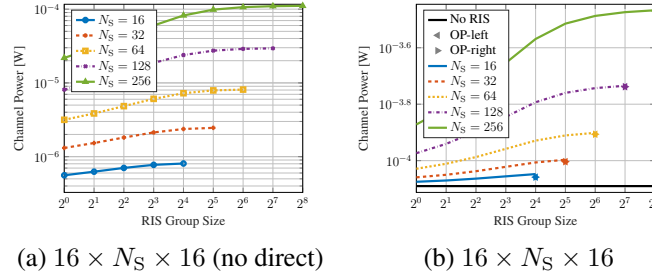
Fig. 5.5 Average maximum channel power versus RIS configuration. 'OP-left' and 'OP-right' refer to the suboptimal solutions to problem (5.28) by lossy transformation (5.30) where Θ is to the left and right of the product, respectively.

both triangular and Cauchy-Schwarz inequalities in [51, (50)] can be simultaneously tight regardless of the group size. That is, diagonal RIS is sufficient for subspace alignment in SISO while the $62.5\,\%$ gain from BD-RIS comes purely from subchannel rearrangement (i.e., pairing the forward and backward channels from strongest to weakest). Now consider a diagonal RIS in MIMO. Each element can only apply a common phase shift to the associated rank-1 $N_{\mathrm{R}} \times N_{\mathrm{T}}$ indirect channel. Therefore, perfect subspace alignment of indirect channels through different elements is generally impossible. It means the disadvantage of diagonal RIS in subspace alignment and subchannel rearrangement scales with MIMO dimensions. We thus conclude that the power gain of BD-RIS scales with group size and MIMO dimensions.

5.5.2   Achievable Rate Maximization

We first focus on channel shaping subproblem (6.29). Fig. 5.5 shows the achievable channel power under different RIS configurations. An interesting observation is that the relative power gain of BD-RIS over diagonal RIS is even larger with direct link. For example, a 64-element fully BD-RIS can almost provide the same channel power as a 256-element diagonal RIS in Fig. 5.5b, but not in Fig. 5.5a. This is because the RIS needs to balance the multiplicative forward-backward combining and the additive direct-indirect combining, such that the subspace alignment advantage of BD-RIS becomes more pronounced. We also notice that the suboptimal solutions (5.31) for fully-connected BD-RIS by lossy transformation (5.30) are very close to optimal especially for a large N_{S}.

Fig. 5.6 presents the achievable rate under different MIMO and RIS configurations. At a transmit power of $10\,\mathrm{dB}$, Fig. 5.6(a) shows that introducing a 128-element diagonal RIS to 4T4R MIMO can improve the achievable rate from $22.2\,\mathrm{bps/Hz}$ to $29.2\,\mathrm{bps/Hz}$ ($+31.5\,\%$). In contrast, a BD-RIS of group size 4 and 128 can further improve the rate to $32.1\,\mathrm{bps/Hz}$ ($+44.6\,\%$) and $34\,\mathrm{bps/Hz}$ ($+53.2\,\%$), respectively. Interestingly, the gap between the optimal

(a) $4 \times 128 \times 4$

(b) $N_{\mathrm{T}} \times 128 \times N_{\mathrm{R}}$

(c) $4 \times N_{\mathrm{S}} \times 4$

(d) $4 \times 128 \times 4$
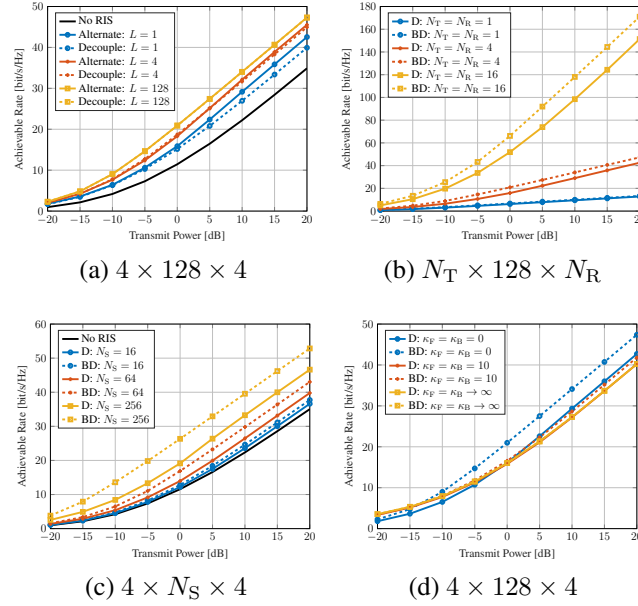
Fig. 5.6 Average achievable rate versus MIMO and RIS configurations. The noise power is $\eta = -75\,\mathrm{dB}$, corresponding to a direct SNR of -10 to $30\,\mathrm{dB}$. 'Alternate' refers to the alternating optimization and 'Decouple' refers to the low-complexity design. 'D' means diagonal RIS and 'BD' means fully-connected BD-RIS.

AO approach (5.25)–(5.27) and the low-complexity solution (5.32) and (5.27) narrows as the group size increases, and completely vanishes for a fully-connected BD-RIS. This implies that the RIS-transceiver design can be completely decoupled via channel shaping with marginal performance loss. Figs. 5.6(b) and 5.6(c) also confirm the advantage of BD-RIS grows with the number of transmit, scatter, and receive antennas. In the low power regime (-20 to $-10\,\mathrm{dB}$), the slope of the achievable rate is significantly larger with BD-RIS, suggesting that multiple streams can be activated at a much lower SNR. This is because BD-RIS not only spreads the channel singular values to a wider range, but also provides a better tradeoff between subchannels (c.f. Fig. 5.2). Finally, Fig. 5.6(d) shows that the gap between diagonal and BD-RIS narrows as the Rician K-factor increases and becomes indistinguishable in LoS environment. The observation is expected from previous studies [51, 126, 127] and aligns with Corollary 8.2, which suggests that the BD-RIS should be deployed in rich-scattering environments to exploit its channel shaping potential.

5.6   Conclusion

This paper analyzes the channel shaping capability of RIS in terms of singular values redistribution. We consider a general BD architecture that allows elements within the same group to interact, enabling more sophisticated manipulation than diagonal RIS. This translates to a wider dynamic range (with better tradeoff) of singular values and significant power and rate gains, especially in large-scale MIMO systems. We characterize the Pareto frontiers of channel singular values via optimization approach and provide analytical bounds in rank-deficient and fully-connected scenarios. An efficient RCG algorithm is proposed for smooth BD-RIS optimization problems, which offers lower computation complexity and faster convergence than existing methods. We also present two beamforming designs for rate maximization problem, one based on alternating optimization for optimal performance and the other decouples the RIS-transceiver design for lower complexity. Extensive simulations show that the advantage of BD-RIS stems from its superior subspace alignment and subchannel rearrangement capability, which scales with the number of elements, group size, MIMO dimensions, and channel diversity.

One future direction is introducing BD-RIS to MIMO interference channel for interference alignment or cancellation. Another open issue is to exploit different groups of BD-RIS to enhance the channel response (and possibly ride extra information) at different frequencies. Incorporating a RIS at both transmitter and receiver sides provides even stronger manipulation that potentially align both direct-indirect and forward-backward subspaces simultaneously.

Chapter 6

Appendix

6.1 Proofs for Chapter 1

6.1.1 Proof of Proposition 1

For any feasible $\mathbf{\Phi}$ to problem (3.25), $\mathrm{tr}(\mathbf{\Phi}) = L + 1$ always holds because of the modulus constraint (3.25c). Therefore, we add a constant term $-\mathrm{tr}(\mathbf{\Phi})$ to (3.25a) and recast problem (3.25) as

$$\max_{\mathbf{\Phi}} \quad -\mathrm{tr}(\mathbf{\Phi}) + \tilde{z}(\mathbf{\Phi}) \tag{6.1a}$$

$$\mathrm{s.t.} \quad R(\mathbf{\Phi}) \geq \bar{R}, \tag{6.1b}$$

$$\mathrm{diag}^{-1}(\mathbf{\Phi}) = \mathbf{1}, \tag{6.1c}$$

$$\mathbf{\Phi} \succeq \mathbf{0}, \tag{6.1d}$$

$$\mathrm{rank}(\mathbf{\Phi}) = 1. \tag{6.1e}$$

By applying SDR, problem (6.1a)–(6.1d) is convex w.r.t. $\mathbf{\Phi}$ and satisfies the Slater's condition [114], and strong duality holds. The corresponding Lagrangian function at iteration i is given by (6.2), where μ, $\boldsymbol{\nu}$, $\mathbf{\Upsilon}$ denote respectively the scalar, vector and matrix Lagrange multiplier associated with constraint (6.1b), (6.1c) and (6.1d), and ζ collects all terms irrelevant to $\mathbf{\Phi}^{(i)}$. The Karush–Kuhn–Tucker (KKT) conditions on the primal and dual solutions are

$$\mu^{\star} \geq 0, \mathbf{\Upsilon}^{\star} \succeq \mathbf{0}, \tag{6.3a}$$

$$\boldsymbol{\nu}^{\star} \odot \mathrm{diag}^{-1}(\mathbf{\Phi}^{\star}) = \mathbf{0}, \mathbf{\Upsilon}^{\star}\mathbf{\Phi}^{\star} = \mathbf{0}, \tag{6.3b}$$

$$\nabla_{\mathbf{\Phi}^{\star}}\mathcal{L} = 0. \tag{6.3c}$$

We then derive the gradient explicitly and rewrite (6.3c) as

$$\mathbf{\Upsilon}^{\star} = \mathbf{I} - \mathbf{\Delta}^{\star}, \tag{6.4}$$

where $\mathbf{\Delta}^{\star}$ is given by (6.5). Note that (6.3b) suggests $\mathrm{rank}(\mathbf{\Upsilon}^{\star}) + \mathrm{rank}(\mathbf{\Phi}^{\star}) \leq L + 1$. By reusing the proof in [160, Appendix A], we conclude $\mathrm{rank}(\mathbf{\Upsilon}^{\star}) \geq L$. On the other hand, $\mathbf{\Phi}^{\star}$ cannot be zero matrix and $\mathrm{rank}(\mathbf{\Phi}^{\star}) \geq 1$. Therefore, any optimal solution $\mathbf{\Phi}^{\star}$ to the relaxed problem (6.1) is rank-1. Due to the equivalence between (3.25a) and (6.1a), $\mathbf{\Phi}^{\star}$ is also optimal to the relaxed problem (3.25) and Proposition 1 holds.

6.1.2 Proof of Proposition 2

The objective function (3.25a) is non-decreasing over iterations because the solution to (3.25a)–(3.25d) at iteration $i - 1$ is still feasible at iteration i. Also, the sequence $\{\tilde{z}(\mathbf{\Phi}^{(i)})\}_{i=1}^{\infty}$ is bounded above because of the unit-modulus constraint (3.25c). Thus, Algorithm 1 is guaranteed to converge. Besides, we notice that Algorithm 1 is an inner approximation algorithm [161], because $\tilde{z}(\mathbf{\Phi}) \leq z(\mathbf{\Phi})$, $\partial\tilde{z}(\mathbf{\Phi}^{(i)})/\partial\mathbf{\Phi} = \partial z(\mathbf{\Phi}^{(i)})/\partial\mathbf{\Phi}$ and the approximation (3.20)–(3.22) are asymptotically tight as $i \to \infty$ [162]. Therefore, it is guaranteed to provide a local optimal $\mathbf{\Phi}^{\star}$ to the relaxed passive beamforming problem. According to Proposition 1,

$$\mathcal{L} = \mathrm{tr}\left(\mathbf{\Phi}^{(i)}\right) - \frac{1}{2}\beta_2\rho\,\mathrm{tr}\left((\mathbf{C}_{\mathrm{I},0} + \mathbf{C}_{\mathrm{P},0})\mathbf{\Phi}^{(i)}\right) - \frac{3}{4}\beta_4\rho^2\left(2t_{\mathrm{I},0}^{(i-1)}\mathrm{tr}\left(\mathbf{C}_{\mathrm{I},0}\mathbf{\Phi}^{(i)}\right) + \sum_{k=-N+1}^{N-1}(t_{\mathrm{P},k}^{(i-1)})^*\mathrm{tr}\left(\mathbf{C}_{\mathrm{P},k}\mathbf{\Phi}^{(i)}\right)\right.$$

$$\left. + 2t_{\mathrm{P},0}^{(i-1)}\mathrm{tr}\left(\mathbf{C}_{\mathrm{I},0}\mathbf{\Phi}^{(i)}\right) + 2t_{\mathrm{I},0}^{(i-1)}\mathrm{tr}\left(\mathbf{C}_{\mathrm{P},0}\mathbf{\Phi}^{(i)}\right)\right) + \mu\left(2^{\bar{R}} - \prod_{n=1}^{N}\left(1 + \frac{(1-\rho)\mathrm{tr}\left(\mathbf{C}_n\mathbf{\Phi}^{(i)}\right)}{\sigma_n^2}\right)\right)$$

$$+ \mathrm{tr}\left(\mathrm{diag}(\boldsymbol{\nu}) \odot \left(\mathbf{\Phi}^{(i)} \odot \mathbf{I} - \mathbf{I}\right)\right) - \mathrm{tr}\left(\mathbf{\Upsilon}\mathbf{\Phi}^{(i)}\right) + \zeta. \tag{6.2}$$

$$\mathbf{\Delta}^{\star} = \frac{1}{2}\beta_2\rho(\mathbf{C}_{\mathrm{I},0} + \mathbf{C}_{\mathrm{P},0}) + \frac{3}{4}\beta_4\rho^2\left(2t_{\mathrm{I},0}^{(i-1)}\mathbf{C}_{\mathrm{I},0} + \sum_{k=-N+1}^{N-1}(t_{\mathrm{P},k}^{(i-1)})^*\mathbf{C}_{\mathrm{P},k} + 2t_{\mathrm{P},0}^{(i-1)}\mathbf{C}_{\mathrm{I},0} + 2t_{\mathrm{I},0}^{(i-1)}\mathbf{C}_{\mathrm{P},0}\right)$$

$$+ \mu^{\star}\sum_{n=1}^{N}\frac{(1-\rho)\mathbf{C}_n}{\sigma_n^2}\prod_{n'=1,n'\neq n}^{N}\left(1 + \frac{(1-\rho)\mathrm{tr}\left(\mathbf{C}_{n'}\mathbf{\Phi}^{\star}\right)}{\sigma_{n'}^2}\right) - \mathrm{diag}(\boldsymbol{\nu}^{\star}). \tag{6.5}$$

$\Phi^\star$ is rank-1 such that $\phi^\star$ can be extracted without performance loss and the local optimality inherits to the original problem (3.15).

6.1.3   Proof of Proposition 3

From the perspective of WIT, the MRT precoder maximizes $|\boldsymbol{h}_n^H \boldsymbol{w}_{\mathrm{I},n}| = \|\boldsymbol{h}_n\| s_{\mathrm{I},n}$ and maximizes the rate (3.7). From the perspective of WPT, the MRT precoder maximizes $(\boldsymbol{h}_n^H \boldsymbol{w}_{\mathrm{I/P},n})(\boldsymbol{h}_n^H \boldsymbol{w}_{\mathrm{I/P},n})^* = \|\boldsymbol{h}_n\|^2 s_{\mathrm{I/P},n}^2$ and maximizes the second and fourth order DC terms (3.10)–(3.13). Therefore, MRT is the global optimal information and power precoder.

6.2   Proofs for Chapter 2

6.2.1   Proof of Proposition 5

Denote the Lagrange multipliers associated with (4.17b) and (4.17c) as $\{\nu_k\}_{k\in\mathcal{K}}$ and $\{\lambda_{m_k}\}_{k\in\mathcal{K}, m_k\in\mathcal{M}}$, respectively. The Lagrangian function of problem (4.18) is

$$L(p, \nu, \lambda) = I(x_\mathcal{K}) + \sum_k \nu_k \left(\sum_{m_k} p(x_{m_k}) - 1 \right) + \sum_{k,m_k} \lambda_{m_k} p(x_{m_k}), \tag{6.6}$$

and the KKT conditions are, $\forall k, m_k,$

$$I_k^\star(x_{m_k}) - (1 - \rho) + \nu_k^\star + \lambda_{m_k}^\star = 0, \tag{6.7a}$$

$$\lambda_{m_k}^\star = 0, \quad \text{if } p^\star(x_{m_k}) > 0, \tag{6.7b}$$

$$\lambda_{m_k}^\star \geq 0, \quad \text{if } p^\star(x_{m_k}) = 0. \tag{6.7c}$$

Plugging (6.7b) and (6.7c) into (6.7a) yields

$$I_k^\star(x_{m_k}) = 1 - \rho - \nu_k^\star, \quad \text{if } p^\star(x_{m_k}) > 0, \tag{6.8a}$$

$$I_k^\star(x_{m_k}) \leq 1 - \rho - \nu_k^\star, \quad \text{if } p^\star(x_{m_k}) = 0, \tag{6.8b}$$

such that

$$\sum_{m_k} p^\star(x_{m_k}) I_k^\star(x_{m_k}) = 1 - \rho - \nu_k^\star. \tag{6.9}$$

On the other hand, by definition (4.20) we have

$$\sum_{m_k} p^\star(x_{m_k}) I_k^\star(x_{m_k}) = I^\star(x_\mathcal{K}), \tag{6.10}$$

where the right-hand side is irrelevant to k. (6.8), (6.9), and (6.10) together complete the proof.

6.2.2 Proof of Proposition 6

We first prove sequence (4.21) is non-decreasing in weighted sum mutual information. Let $p(x_{m_\mathcal{K}}) = \prod_{q\in\mathcal{K}} p(x_{m_q})$ and $p'(x_{m_\mathcal{K}}) = p'(x_{m_k})\prod_{q\in\mathcal{K}\setminus\{k\}} p(x_{m_q})$ be two distributions potentially different at x_{m_k}, and $J\big(p(x_{m_\mathcal{K}}), p'(x_{m_\mathcal{K}})\big)$ be a joint function defined in (6.11) at the end of page 88. It is straightforward to verify $J\big(p(x_{m_\mathcal{K}}), p(x_{m_\mathcal{K}})\big) = I(x_\mathcal{K})$ and $J\big(p(x_{m_\mathcal{K}}), p'(x_{m_\mathcal{K}})\big)$ is a concave function for a given $p'(x_{m_\mathcal{K}})$. Setting $\nabla_{p(x_{m_k})} J\big(p(x_{m_\mathcal{K}}), p'(x_{m_\mathcal{K}})\big) = 0$ yields

$$S'_k(x_{m_k}) - S'_k(x_{i_k}) + (1-\rho)\log\frac{p(x_{i_k})}{p^\star(x_{m_k})} = 0, \tag{6.12}$$

where $i_k \neq m_k$ is the reference state and

$$S'_k(x_{m_k}) \triangleq I'_k(x_{m_k}) + (1-\rho)\sum_{m_{\mathcal{K}\setminus\{k\}}} p(x_{m_{\mathcal{K}\setminus\{k\}}})$$
$$\times \sum_{m'_\mathcal{K}} q(\hat{x}_{m'_\mathcal{K}}|x_{m_\mathcal{K}})\log p'(x_{m_\mathcal{K}}). \tag{6.13}$$

Evidently, $\forall m_k \neq i_k$, (6.12) boils down to

$$p^\star(x_{m_k}) = \frac{p'(x_{m_k})\exp\left(\frac{\rho}{1-\rho}I'_k(x_{m_k})\right)}{\sum_{m'_k} p'(x_{m'_k})\exp\left(\frac{\rho}{1-\rho}I'_k(x_{m'_k})\right)}. \tag{6.14}$$

Since $p(x_{i_k}) = 1 - \sum_{m_k\neq i_k} p^\star(x_{m_k})$ has exactly the same form as (6.14), the choice of reference does not matter and (6.14) is optimal $\forall m_k \in \mathcal{M}$. That is, for a fixed $p'(x_{m_\mathcal{K}})$, (6.14) ensures

$$J\big(p(x_{m_\mathcal{K}}), p'(x_{m_\mathcal{K}})\big) \geq I'(x_\mathcal{K}). \tag{6.15}$$

On the other hand, we notice

$$I(x_\mathcal{K}) - J\big(p(x_{m_\mathcal{K}}), p'(x_{m_\mathcal{K}})\big)$$

$$J\big(p(x_{m_\mathcal{K}}), p'(x_{m_\mathcal{K}})\big) \triangleq \sum_{m_\mathcal{K}} p(x_{m_\mathcal{K}})\left(\rho\log\left(1+\frac{|\boldsymbol{h}^\mathsf{H}(x_{m_\mathcal{K}})\boldsymbol{w}|^2}{\sigma_v^2}\right) + (1-\rho)\sum_{m'_\mathcal{K}} q(\hat{x}_{m'_\mathcal{K}}|x_{m_\mathcal{K}})\log\frac{q(\hat{x}_{m'_\mathcal{K}}|x_{m_\mathcal{K}})p'(x}{p'(\hat{x}_{m'_\mathcal{K}})p(x_{m_\mathcal{K}}}\right.$$
$$\tag{6.11}$$

$$
\begin{aligned}
&= (1-\rho) \sum_{m_k} \frac{p'(x_{m_k}) f_k'(x_{m_k})}{\sum_{m_k'} p'(x_{m_k'}) f_k'(x_{m_k'})} \sum_{m_{\mathcal{K}}''} q(\hat{x}_{m_{\mathcal{K}}''} | x_{m_k}) \\
&\quad \times \log \frac{\sum_{m_k'} p'(x_{m_k'}) q(\hat{x}_{m_{\mathcal{K}}''} | x_{m_k'}) f_k'(x_{m_k})}{\sum_{m_k'} p'(x_{m_k'}) q(\hat{x}_{m_{\mathcal{K}}''} | x_{m_k'}) f_k'(x_{m_k'})}
\end{aligned}
\tag{6.16a}
$$

$$
\begin{aligned}
&\geq (1-\rho) \sum_{m_k} \frac{p'(x_{m_k}) f_k'(x_{m_k})}{\sum_{m_k'} p'(x_{m_k'}) f_k'(x_{m_k'})} \sum_{m_{\mathcal{K}}''} q(\hat{x}_{m_{\mathcal{K}}''} | x_{m_k}) \\
&\quad \times \left(1 - \frac{\sum_{m_k'} p'(x_{m_k'}) q(\hat{x}_{m_{\mathcal{K}}''} | x_{m_k'}) f_k'(x_{m_k'})}{\sum_{m_k'} p'(x_{m_k'}) q(\hat{x}_{m_{\mathcal{K}}''} | x_{m_k'}) f_k'(x_{m_k})} \right)
\end{aligned}
\tag{6.16b}
$$

$$
\begin{aligned}
&= (1-\rho) \left(1 - \sum_{m_k} \frac{p'(x_{m_k}) \cancel{f_k'(x_{m_k})}}{\sum_{m_k'} p'(x_{m_k'}) f_k'(x_{m_k'})} \sum_{m_{\mathcal{K}}''} q(\hat{x}_{m_{\mathcal{K}}''} | x_{m_k}) \right. \\
&\quad \left. \times \frac{\sum_{m_k'} p'(x_{m_k'}) q(\hat{x}_{m_{\mathcal{K}}''} | x_{m_k'}) f_k'(x_{m_k'})}{\sum_{m_k'} p'(x_{m_k'}) q(\hat{x}_{m_{\mathcal{K}}''} | x_{m_k'}) \cancel{f_k'(x_{m_k})}} \right)
\end{aligned}
\tag{6.16c}
$$

$$
\begin{aligned}
&= (1-\rho) \left(1 - \sum_{m_{\mathcal{K}}''} \frac{\cancel{\sum_{m_k} p'(x_{m_k}) q(\hat{x}_{m_{\mathcal{K}}''} | x_{m_k})}}{\sum_{m_k'} p'(x_{m_k'}) f_k'(x_{m_k'})} \right. \\
&\quad \left. \times \frac{\sum_{m_k'} p'(x_{m_k'}) q(\hat{x}_{m_{\mathcal{K}}''} | x_{m_k'}) f_k'(x_{m_k'})}{\cancel{\sum_{m_k'} p'(x_{m_k'}) q(\hat{x}_{m_{\mathcal{K}}''} | x_{m_k'})}} \right)
\end{aligned}
\tag{6.16d}
$$

$$
= (1-\rho) \left(1 - \frac{\sum_{m_k'} p'(x_{m_k'}) f_k'(x_{m_k'}) \sum_{m_{\mathcal{K}}''} q(\hat{x}_{m_{\mathcal{K}}''} | x_{m_k'})}{\sum_{m_k'} p'(x_{m_k'}) f_k'(x_{m_k'})} \right)
$$

$$
= 0,
\tag{6.16e}
$$

where $f_k'(x_{m_k}) \triangleq \exp\!\left(\frac{\rho}{1-\rho} I_k'(x_{m_k}) \right)$ and the equality holds if and only if $p(x_{m_{\mathcal{K}}})$ and $p'(x_{m_{\mathcal{K}}})$ equals (i.e., (6.14) converges). (6.15) and (6.16) together imply $I(x_{\mathcal{K}}) \geq I'(x_{\mathcal{K}})$. Since mutual information is bounded above, we conclude the sequence (4.21) is non-decreasing and convergent.

Next, we prove any converging point of sequence (4.21), denoted as $p^\star(x_{m_k})$, fulfills the KKT conditions (4.19). Let

$$
D^{(r)}(x_{m_k}) \triangleq \frac{p^{(r+1)}(x_{m_k})}{p^{(r)}(x_{m_k})} = \frac{f_k^{(r)}(x_{m_k})}{\sum_{m_k'} p^{(r)}(x_{m_k'}) f_k^{(r)}(x_{m_k'})}.
\tag{6.17}
$$

As sequence (4.21) is convergent, any state with $p^\star(x_{m_k}) > 0$ need to satisfy $D^\star(x_{m_k}) \triangleq \lim_{r \to \infty} D^{(r)}(x_{m_k}) = 1$, namely

$$I_k^\star(x_{m_k}) = \frac{1-\rho}{\rho} \log \sum_{m_k'} p^\star(x_{m_k'}) \exp\left(\frac{\rho}{1-\rho} I_k^\star(x_{m_k'})\right). \tag{6.18}$$

The right-hand side is a constant for node k and implies (6.8a). That is, any converging point with nonzero probability must satisfy (4.19a). On the other hand, we assume $p^\star(x_{m_k}) = 0$ does not satisfy (4.19b), namely

$$I_k^\star(x_{m_k}) > I^\star(x_{\mathcal{K}}) = \sum_{m_k'} p^\star(x_{m_k'}) I_k^\star(x_{m_k'}), \tag{6.19}$$

Since the exponential function is monotonically increasing, (6.19) implies $f_k^\star(x_{m_k}) > \sum_{m_k'} p^\star(x_{m_k'}) f_k^\star(x_{m_k'})$ and $D^\star(x_{m_k}) > 1$. It contradicts with

$$p^{(r)}(x_{m_k}) = p^{(0)}(x_{m_k}) \prod_{n=1}^{r} D^{(n)}(x_{m_k}), \tag{6.20}$$

since the left-hand side is zero while all terms on the right-hand side are strictly positive. The proof is completed.

6.3 Proofs for Chapter 3

6.3.1 Proof of Lemma 1

Let $\mathbf{H} = \sum_n \mathbf{u}_n \sigma_n \mathbf{v}_n^\mathsf{H}$ be the compact SVD of the equivalent channel. Since the singular vectors are orthonormal, the n-th singular value can be expressed as

$$\sigma_n = \mathbf{u}_n^\mathsf{H} \mathbf{H} \mathbf{v}_n = \mathbf{u}_n^\mathsf{T} \mathbf{H}^* \mathbf{v}_n^*, \tag{6.21}$$

whose differential w.r.t. $\boldsymbol{\Theta}_g^*$ is

$$\partial\sigma_n = \partial\mathbf{u}_n^\mathsf{T}\underbrace{\mathbf{H}^*\mathbf{v}_n^*}_{\sum_m \mathbf{u}_m^*\sigma_m\mathbf{v}_m^\mathsf{T}\mathbf{v}_n} + \mathbf{u}_n^\mathsf{T}\cdot\partial\mathbf{H}^*\cdot\mathbf{v}_n^* + \underbrace{\mathbf{u}_n^\mathsf{T}\mathbf{H}^*}_{\mathbf{u}_n^\mathsf{T}\sum_m \mathbf{u}_m^*\sigma_m\mathbf{v}_m^\mathsf{T}}\partial\mathbf{v}_n^*$$

$$= \underbrace{\partial\mathbf{u}_n^\mathsf{T}\mathbf{u}_n^*}_{\partial 1 = 0}\cdot\sigma_n + \mathbf{u}_n^\mathsf{T}\cdot\partial\mathbf{H}^*\cdot\mathbf{v}_n^* + \sigma_n\cdot\underbrace{\mathbf{v}_n^\mathsf{T}\partial\mathbf{v}_n^*}_{\partial 1 = 0}$$

$$= \mathbf{u}_n^\mathsf{T}\mathbf{H}_{\mathrm{B},g}^*\cdot\partial\boldsymbol{\Theta}_g^*\cdot\mathbf{H}_{\mathrm{F},g}^*\mathbf{v}_n^*$$

$$= \mathrm{tr}(\mathbf{H}_{\mathrm{F},g}^*\mathbf{v}_n^*\mathbf{u}_n^\mathsf{T}\mathbf{H}_{\mathrm{B},g}^*\cdot\partial\boldsymbol{\Theta}_g^*).$$

According to [163], the corresponding complex derivative is

$$\frac{\partial\sigma_n}{\partial\boldsymbol{\Theta}_g^*} = \mathbf{H}_{\mathrm{B},g}^\mathsf{H}\mathbf{u}_n\mathbf{v}_n^\mathsf{H}\mathbf{H}_{\mathrm{F},g}^\mathsf{H}. \tag{6.22}$$

A linear combination of (6.22) yields (5.14).

6.3.2 Proof of Proposition 7

The scattering matrix of BD-RIS can be decomposed as[1]

$$\boldsymbol{\Theta} = \mathbf{L}\boldsymbol{\Theta}_\mathrm{D}\mathbf{R}^\mathsf{H}, \tag{6.23}$$

where $\boldsymbol{\Theta}_\mathrm{D} \in \mathbb{U}^{N_\mathrm{S}\times N_\mathrm{S}}$ corresponds to diagonal RIS and $\mathbf{L}, \mathbf{R} \in \mathbb{U}^{N_\mathrm{S}\times N_\mathrm{S}}$ are block diagonal matrices of $L \times L$ unitary blocks. Manipulating $\mathbf{L}$ and $\mathbf{R}$ rotates the linear spans of $\bar{\mathbf{H}}_\mathrm{B} \triangleq \mathbf{H}_\mathrm{B}\mathbf{L}$ and $\bar{\mathbf{H}}_\mathrm{F} \triangleq \mathbf{R}^\mathsf{H}\mathbf{H}_\mathrm{F}$ and maintains their rank. On the other hand, there exists a $\boldsymbol{\Theta}_\mathrm{D}$ such that

$$\mathrm{rank}(\mathbf{H}_\mathrm{B}\boldsymbol{\Theta}_\mathrm{D}\mathbf{H}_\mathrm{F}) = \min\big(\mathrm{rank}(\mathbf{H}_\mathrm{B}), \mathrm{rank}(\boldsymbol{\Theta}_\mathrm{D}), \mathrm{rank}(\mathbf{H}_\mathrm{F})\big)$$

$$= \min\big(\mathrm{rank}(\bar{\mathbf{H}}_\mathrm{B}), N_\mathrm{S}, \mathrm{rank}(\bar{\mathbf{H}}_\mathrm{F})\big)$$

$$= \max_{\boldsymbol{\Theta}}\ \mathrm{rank}(\mathbf{H}_\mathrm{B}\boldsymbol{\Theta}\mathbf{H}_\mathrm{F})$$

The same result holds if the direct link is present.

6.3.3 Proof of Proposition 8

We consider rank-k forward channel and the proof follows similarly for rank-k backward channel. Let $\mathbf{H}_\mathrm{F} = \mathbf{U}_\mathrm{F}\boldsymbol{\Sigma}_\mathrm{F}\mathbf{V}_\mathrm{F}^\mathsf{H}$ be the compact SVD of the forward channel. The channel

---

[1]This is because (block) unitary matrices are closed under multiplication.

Gram matrix $\mathbf{G} \triangleq \mathbf{H}\mathbf{H}^{\mathsf{H}}$ can be written as

$$
\begin{aligned}
\mathbf{G} &= \mathbf{H}_{\mathrm{D}}\mathbf{H}_{\mathrm{D}}^{\mathsf{H}} + \mathbf{H}_{\mathrm{B}}\boldsymbol{\Theta}\mathbf{U}_{\mathrm{F}}\boldsymbol{\Sigma}_{\mathrm{F}}\boldsymbol{\Sigma}_{\mathrm{F}}^{\mathsf{H}}\mathbf{U}_{\mathrm{F}}^{\mathsf{H}}\boldsymbol{\Theta}^{\mathsf{H}}\mathbf{H}_{\mathrm{B}}^{\mathsf{H}} \\
&\quad + \mathbf{H}_{\mathrm{B}}\boldsymbol{\Theta}\mathbf{U}_{\mathrm{F}}\boldsymbol{\Sigma}_{\mathrm{F}}\mathbf{V}_{\mathrm{F}}^{\mathsf{H}}\mathbf{H}_{\mathrm{D}}^{\mathsf{H}} + \mathbf{H}_{\mathrm{D}}\mathbf{V}_{\mathrm{F}}\boldsymbol{\Sigma}_{\mathrm{F}}\mathbf{U}_{\mathrm{F}}^{\mathsf{H}}\boldsymbol{\Theta}^{\mathsf{H}}\mathbf{H}_{\mathrm{B}}^{\mathsf{H}} \\
&= \mathbf{H}_{\mathrm{D}}(\mathbf{I} - \mathbf{V}_{\mathrm{F}}\mathbf{V}_{\mathrm{F}}^{\mathsf{H}})\mathbf{H}_{\mathrm{D}}^{\mathsf{H}} \\
&\quad + (\mathbf{H}_{\mathrm{B}}\boldsymbol{\Theta}\mathbf{U}_{\mathrm{F}}\boldsymbol{\Sigma}_{\mathrm{F}} + \mathbf{H}_{\mathrm{D}}\mathbf{V}_{\mathrm{F}})(\boldsymbol{\Sigma}_{\mathrm{F}}\mathbf{U}_{\mathrm{F}}^{\mathsf{H}}\boldsymbol{\Theta}^{\mathsf{H}}\mathbf{H}_{\mathrm{B}}^{\mathsf{H}} + \mathbf{V}_{\mathrm{F}}^{\mathsf{H}}\mathbf{H}_{\mathrm{D}}^{\mathsf{H}}) \\
&= \mathbf{Y} + \mathbf{Z}\mathbf{Z}^{\mathsf{H}},
\end{aligned}
$$

where we define $\mathbf{Y} \triangleq \mathbf{H}_{\mathrm{D}}(\mathbf{I} - \mathbf{V}_{\mathrm{F}}\mathbf{V}_{\mathrm{F}}^{\mathsf{H}})\mathbf{H}_{\mathrm{D}}^{\mathsf{H}} \in \mathbb{H}^{N_{\mathrm{R}} \times N_{\mathrm{R}}}$ and $\mathbf{Z} \triangleq \mathbf{H}_{\mathrm{B}}\boldsymbol{\Theta}\mathbf{U}_{\mathrm{F}}\boldsymbol{\Sigma}_{\mathrm{F}} + \mathbf{H}_{\mathrm{D}}\mathbf{V}_{\mathrm{F}} \in \mathbb{C}^{N_{\mathrm{R}} \times k}$. That is to say, $\mathbf{G}$ can be expressed as a Hermitian matrix plus k rank-1 perturbations. According to the Cauchy interlacing formula [38], the n-th eigenvalue of $\mathbf{G}$ is bounded by

$$
\begin{aligned}
\lambda_n(\mathbf{G}) &\leq \lambda_{n-k}(\mathbf{Y}), && \text{if } n > k, && (6.24) \\
\lambda_n(\mathbf{G}) &\geq \lambda_n(\mathbf{Y}), && \text{if } n < N - k + 1. && (6.25)
\end{aligned}
$$

Since $\mathbf{Y} = \mathbf{T}\mathbf{T}^{\mathsf{H}}$ is positive semi-definite, taking the square roots of (6.24) and (6.25) gives (5.15) and (5.16).

6.3.4 Proof of Proposition 9

Let $\mathbf{H}_{\mathrm{B}} = \mathbf{U}_{\mathrm{B}}\boldsymbol{\Sigma}_{\mathrm{B}}\mathbf{V}_{\mathrm{B}}^{\mathsf{H}}$ and $\mathbf{H}_{\mathrm{F}} = \mathbf{U}_{\mathrm{F}}\boldsymbol{\Sigma}_{\mathrm{F}}\mathbf{V}_{\mathrm{F}}^{\mathsf{H}}$ be the SVD of the backward and forward channels, respectively. The scattering matrix of fully-connected RIS can be decomposed as

$$
\boldsymbol{\Theta} = \mathbf{V}_{\mathrm{B}}\mathbf{X}\mathbf{U}_{\mathrm{F}}^{\mathsf{H}}, \tag{6.26}
$$

where $\mathbf{X} \in \mathbb{U}^{N_{\mathrm{S}} \times N_{\mathrm{S}}}$ is a unitary matrix to be designed. The equivalent channel is thus a function of $\mathbf{X}$

$$
\mathbf{H} = \mathbf{H}_{\mathrm{B}}\boldsymbol{\Theta}\mathbf{H}_{\mathrm{F}} = \mathbf{U}_{\mathrm{B}}\boldsymbol{\Sigma}_{\mathrm{B}}\mathbf{X}\boldsymbol{\Sigma}_{\mathrm{F}}\mathbf{V}_{\mathrm{F}}^{\mathsf{H}}. \tag{6.27}
$$

Since $\mathrm{sv}(\mathbf{U}\mathbf{A}\mathbf{V}^{\mathsf{H}}) = \mathrm{sv}(\mathbf{A})$ for unitary $\mathbf{U}$ and $\mathbf{V}$, we have

$$
\begin{aligned}
\mathrm{sv}(\mathbf{H}) &= \mathrm{sv}(\mathbf{U}_{\mathrm{B}}\boldsymbol{\Sigma}_{\mathrm{B}}\mathbf{X}\boldsymbol{\Sigma}_{\mathrm{F}}\mathbf{V}_{\mathrm{F}}^{\mathsf{H}}) \\
&= \mathrm{sv}(\boldsymbol{\Sigma}_{\mathrm{B}}\mathbf{X}\boldsymbol{\Sigma}_{\mathrm{F}}) \\
&= \mathrm{sv}(\bar{\mathbf{U}}_{\mathrm{B}}\boldsymbol{\Sigma}_{\mathrm{B}}\bar{\mathbf{V}}_{\mathrm{B}}^{\mathsf{H}}\bar{\mathbf{U}}_{\mathrm{F}}\boldsymbol{\Sigma}_{\mathrm{F}}\bar{\mathbf{V}}_{\mathrm{F}}^{\mathsf{H}}) \\
&= \mathrm{sv}(\mathbf{B}\mathbf{F}),
\end{aligned}
$$

where $\bar{\mathbf{U}}_{\mathrm{B/F}}$ and $\bar{\mathbf{V}}_{\mathrm{B/F}}$ are arbitrary unitary matrices.

6.3.5 Proof of Lemma 2

The differential of R w.r.t. $\boldsymbol{\Theta}_g^*$ is [163]

$$
\begin{aligned}
\partial R &= \frac{1}{\eta}\mathrm{tr}\Big\{\partial\mathbf{H}^* \cdot \mathbf{Q}^\mathsf{T}\mathbf{H}^\mathsf{T}\Big(\mathbf{I}+\frac{\mathbf{H}^*\mathbf{Q}^\mathsf{T}\mathbf{H}^\mathsf{T}}{\eta}\Big)^{-1}\Big\} \\
&= \frac{1}{\eta}\mathrm{tr}\Big\{\mathbf{H}_{\mathrm{B},g}^* \cdot \partial\boldsymbol{\Theta}_g^* \cdot \mathbf{H}_{\mathrm{F},g}^*\mathbf{Q}^\mathsf{T}\mathbf{H}^\mathsf{T}\Big(\mathbf{I}+\frac{\mathbf{H}^*\mathbf{Q}^\mathsf{T}\mathbf{H}^\mathsf{T}}{\eta}\Big)^{-1}\Big\} \\
&= \frac{1}{\eta}\mathrm{tr}\Big\{\mathbf{H}_{\mathrm{F},g}^*\mathbf{Q}^\mathsf{T}\mathbf{H}^\mathsf{T}\Big(\mathbf{I}+\frac{\mathbf{H}^*\mathbf{Q}^\mathsf{T}\mathbf{H}^\mathsf{T}}{\eta}\Big)^{-1}\mathbf{H}_{\mathrm{B},g}^* \cdot \partial\boldsymbol{\Theta}_g^*\Big\},
\end{aligned}
$$

and the corresponding complex derivative is (5.26).

6.3.6 Proof of Proposition 10

The differential of (5.28a) w.r.t. $\boldsymbol{\Theta}_g^*$ is

$$
\begin{aligned}
\partial\|\mathbf{H}\|_\mathrm{F}^2 &= \mathrm{tr}\big(\mathbf{H}_{\mathrm{B},g}^* \cdot \partial\boldsymbol{\Theta}_g^* \cdot \mathbf{H}_{\mathrm{F},g}^*(\mathbf{H}_\mathrm{D}^\mathsf{T}+\mathbf{H}_\mathrm{F}^\mathsf{T}\boldsymbol{\Theta}^\mathsf{T}\mathbf{H}_\mathrm{B}^\mathsf{T})\big) \\
&= \mathrm{tr}\big(\mathbf{H}_{\mathrm{F},g}^*(\mathbf{H}_\mathrm{D}^\mathsf{T}+\mathbf{H}_\mathrm{F}^\mathsf{T}\boldsymbol{\Theta}^\mathsf{T}\mathbf{H}_\mathrm{B}^\mathsf{T})\mathbf{H}_{\mathrm{B},g}^* \cdot \partial\boldsymbol{\Theta}_g^*\big)
\end{aligned}
$$

and the corresponding complex derivative is

$$
\frac{\partial\|\mathbf{H}\|_\mathrm{F}^2}{\partial\boldsymbol{\Theta}_g^*} = \mathbf{H}_{\mathrm{B},g}^\mathsf{H}(\mathbf{H}_\mathrm{D}+\mathbf{H}_\mathrm{B}\boldsymbol{\Theta}\mathbf{H}_\mathrm{F})\mathbf{H}_{\mathrm{F},g}^\mathsf{H} = \mathbf{M}_g. \tag{6.28}
$$

First, we approximate the quadratic objective (5.28a) by its local Taylor expansion

$$
\max_{\boldsymbol{\Theta}} \quad \sum_g 2\Re\big\{\mathrm{tr}(\boldsymbol{\Theta}_g^\mathsf{H}\mathbf{M}_g)\big\} \tag{6.29a}
$$

$$
\text{s.t.} \quad \boldsymbol{\Theta}_g^\mathsf{H}\boldsymbol{\Theta}_g = \mathbf{I}, \quad \forall g. \tag{6.29b}
$$

Let $\mathbf{M}_g = \mathbf{U}_g\boldsymbol{\Sigma}_g\mathbf{V}_g^\mathsf{H}$ be the compact SVD of $\mathbf{M}_g$. We have

$$
\Re\big\{\mathrm{tr}(\boldsymbol{\Theta}_g^\mathsf{H}\mathbf{M}_g)\big\} = \Re\big\{\mathrm{tr}(\boldsymbol{\Sigma}_g\mathbf{V}_g^\mathsf{H}\boldsymbol{\Theta}_g^\mathsf{H}\mathbf{U}_g)\big\} \le \mathrm{tr}(\boldsymbol{\Sigma}_g). \tag{6.30}
$$

The upper bound is tight when $\mathbf{V}_g^\mathsf{H}\boldsymbol{\Theta}_g^\mathsf{H}\mathbf{U}_g = \mathbf{I}$, which implies the optimal solution of (6.29) is $\tilde{\boldsymbol{\Theta}}_g = \mathbf{U}_g\mathbf{V}_g^\mathsf{H}, \forall g$.

Next, we prove that solving (6.29) successively does not decrease (5.28a). Since $\tilde{\boldsymbol{\Theta}}$ optimal for problem (6.29), we have $\sum_g 2\Re\big\{\mathrm{tr}(\tilde{\boldsymbol{\Theta}}_g^\mathsf{H}\mathbf{M}_g)\big\} \ge \sum_g 2\Re\big\{\mathrm{tr}(\boldsymbol{\Theta}_g^\mathsf{H}\mathbf{M}_g)\big\}$ which is explicitly expressed by (6.32). On the other hand, expanding $\|\sum_g \mathbf{H}_{\mathrm{B},g}\tilde{\boldsymbol{\Theta}}_g\mathbf{H}_{\mathrm{F},g} - \sum_g \mathbf{H}_{\mathrm{B},g}\boldsymbol{\Theta}_g\mathbf{H}_{\mathrm{F},g}\|_\mathrm{F}^2 \ge$

$$2\Re\Big\{\sum_g \mathrm{tr}(\tilde{\Theta}_g^{\mathsf{H}}\mathbf{H}_{\mathrm{B},g}^{\mathsf{H}}\mathbf{H}_{\mathrm{D}}\mathbf{H}_{\mathrm{F},g}^{\mathsf{H}}) + \sum_{g_1,g_2} \mathrm{tr}(\tilde{\Theta}_{g_1}^{\mathsf{H}}\mathbf{H}_{\mathrm{B},g_1}^{\mathsf{H}}\mathbf{H}_{\mathrm{B},g_2}\Theta_{g_2}\mathbf{H}_{\mathrm{F},g_2}\mathbf{H}_{\mathrm{F},g_1}^{\mathsf{H}})\Big\} \geq 2\Re\Big\{\sum_g \mathrm{tr}(\Theta_g^{\mathsf{H}}\mathbf{H}_{\mathrm{B},g}^{\mathsf{H}}\mathbf{H}_{\mathrm{D}}\mathbf{H}_{\mathrm{F},g}^{\mathsf{H}}) + \sum_{g_1,g_2} \mathrm{tr}(\Theta_{g_1}^{\mathsf{H}}\mathbf{H}_{\mathrm{B},g_1}^{\mathsf{H}}\mathbf{H}_{\mathrm{B},g_2}\Theta_{g_2}\mathbf{H}_{\mathrm{F},g_2}\mathbf{H}_{\mathrm{F},g_1}^{\mathsf{H}})\Big\}$$

(6.32)

$$\sum_{g_1,g_2} \mathrm{tr}(\mathbf{H}_{\mathrm{F},g_1}^{\mathsf{H}}\tilde{\Theta}_{g_1}^{\mathsf{H}}\mathbf{H}_{\mathrm{B},g_1}^{\mathsf{H}}\mathbf{H}_{\mathrm{B},g_2}\tilde{\Theta}_{g_2}\mathbf{H}_{\mathrm{F},g_2}) - 2\Re\Big\{\sum_{g_1,g_2} \mathrm{tr}(\mathbf{H}_{\mathrm{F},g_1}^{\mathsf{H}}\tilde{\Theta}_{g_1}^{\mathsf{H}}\mathbf{H}_{\mathrm{B},g_1}^{\mathsf{H}}\mathbf{H}_{\mathrm{B},g_2}\Theta_{g_2}\mathbf{H}_{\mathrm{F},g_2})\Big\} + \sum_{g_1,g_2} \mathrm{tr}(\mathbf{H}_{\mathrm{F},g_1}^{\mathsf{H}}\Theta_{g_1}^{\mathsf{H}}\mathbf{H}_{\mathrm{B},g_1}^{\mathsf{H}}\mathbf{H}_{\mathrm{B},g_2}\Theta_{g_2}\mathbf{H}_{\mathrm{F},g_2}) \geq 0$$

(6.33)

---

0 gives (6.33). Adding (6.32) and (6.33), we have

$$2\Re\Big\{\mathrm{tr}(\tilde{\Theta}^{\mathsf{H}}\mathbf{H}_{\mathrm{B}}^{\mathsf{H}}\mathbf{H}_{\mathrm{D}}\mathbf{H}_{\mathrm{F}}^{\mathsf{H}})\Big\} + \mathrm{tr}(\mathbf{H}_{\mathrm{F}}^{\mathsf{H}}\tilde{\Theta}^{\mathsf{H}}\mathbf{H}_{\mathrm{B}}^{\mathsf{H}}\mathbf{H}_{\mathrm{B}}\tilde{\Theta}\mathbf{H}_{\mathrm{F}})$$
$$\geq 2\Re\Big\{\mathrm{tr}(\Theta^{\mathsf{H}}\mathbf{H}_{\mathrm{B}}^{\mathsf{H}}\mathbf{H}_{\mathrm{D}}\mathbf{H}_{\mathrm{F}}^{\mathsf{H}})\Big\} + \mathrm{tr}(\mathbf{H}_{\mathrm{F}}^{\mathsf{H}}\Theta^{\mathsf{H}}\mathbf{H}_{\mathrm{B}}^{\mathsf{H}}\mathbf{H}_{\mathrm{B}}\Theta\mathbf{H}_{\mathrm{F}}), \quad (6.31)$$

which suggests that updating $\tilde{\Theta}$ does not decrease (5.28a).

Finally, we prove that the converging point of (6.29), denoted by $\tilde{\Theta}^?$, is a stationary point of (5.28). The KKT conditions of (5.28) and (6.29) are equivalent in terms of primal/dual feasibility and complementary slackness, while the stationary conditions are respectively, $\forall g$,

$$\mathbf{H}_{\mathrm{B},g}^{\mathsf{H}}(\mathbf{H}_{\mathrm{D}} + \mathbf{H}_{\mathrm{B}}\Theta^\star\mathbf{H}_{\mathrm{F}})\mathbf{H}_{\mathrm{F},g}^{\mathsf{H}} - \Theta_g^\star\Lambda_g^{\mathsf{H}} = 0, \quad (6.34)$$

$$\mathbf{M}_g - \Theta_g^\star\Lambda_g^{\mathsf{H}} = 0. \quad (6.35)$$

On convergence, (6.35) becomes $\mathbf{H}_{\mathrm{B},g}^{\mathsf{H}}(\mathbf{H}_{\mathrm{D}} + \mathbf{H}_{\mathrm{B}}\Theta^?\mathbf{H}_{\mathrm{F}})\mathbf{H}_{\mathrm{F},g}^{\mathsf{H}} - \Theta_g^?\Lambda_g^{\mathsf{H}} = 0$ and reduces to (6.34). The proof is thus completed.

References

[1] Y. Huang, A. Alieldin, and C. Song, "Equivalent circuits and analysis of a generalized antenna system," *IEEE Antennas and Propagation Magazine*, vol. 63, pp. 53–62, Apr 2021.

[2] C. E. Shannon, "A mathematical theory of communication," *Bell System Technical Journal*, vol. 27, pp. 379–423, Jul 1948.

[3] B. Clerckx, R. Zhang, R. Schober, D. W. K. Ng, D. I. Kim, and H. V. Poor, "Fundamentals of wireless information and power transfer: From RF energy harvester models to signal and system designs," *IEEE Journal on Selected Areas in Communications*, vol. 37, no. 1, pp. 4–33, Jan. 2019.

[4] L. R. Varshney, "Transporting information and energy simultaneously," in *2008 IEEE International Symposium on Information Theory*. IEEE, Jul. 2008, pp. 1612–1616.

[5] X. Zhou, R. Zhang, and C. K. Ho, "Wireless information and power transfer: Architecture design and rate-energy tradeoff," *IEEE Transactions on Communications*, vol. 61, no. 11, pp. 4754–4767, Nov. 2013.

[6] R. Zhang and C. K. Ho, "MIMO broadcasting for simultaneous wireless information and power transfer," *IEEE Transactions on Wireless Communications*, vol. 12, no. 5, pp. 1989–2001, May 2013.

[7] J. Park and B. Clerckx, "Joint wireless information and energy transfer in a k-user MIMO interference channel," *IEEE Transactions on Wireless Communications*, vol. 13, no. 10, pp. 5781–5796, Oct. 2014.

[8] M. Trotter, J. Griffin, and G. Durgin, "Power-optimized waveforms for improving the range and reliability of RFID systems," in *2009 IEEE International Conference on RFID*. IEEE, Apr. 2009, pp. 80–87.

[9] B. Clerckx and J. Kim, "On the beneficial roles of fading and transmit diversity in wireless power transfer with nonlinear energy harvesting," *IEEE Transactions on Wireless Communications*, vol. 17, no. 11, pp. 7731–7743, Nov. 2018.

[10] B. Clerckx and E. Bayguzina, "Waveform design for wireless power transfer," *IEEE Transactions on Signal Processing*, vol. 64, no. 23, pp. 6313–6328, Dec. 2016.

[11] J. Kim, B. Clerckx, and P. D. Mitcheson, "Experimental analysis of harvested energy and throughput trade-off in a realistic SWIPT system," in *2019 IEEE Wireless Power Transfer Conference (WPTC)*. IEEE, Jun. 2019, pp. 1–5.

[12] ——, "Signal and system design for wireless power transfer: Prototype, experiment and validation," *IEEE Transactions on Wireless Communications*, vol. 19, no. 11, pp. 7453–7469, Nov. 2020.

[13] J. Kim and B. Clerckx, "Range expansion for wireless power transfer using joint beamforming and waveform architecture: An experimental study in indoor environment," *IEEE Wireless Communications Letters*, vol. 10, no. 6, pp. 1237–1241, Jun. 2021.

[14] B. Clerckx and E. Bayguzina, "Low-complexity adaptive multisine waveform design for wireless power transfer," *IEEE Antennas and Wireless Propagation Letters*, vol. 16, no. 1, pp. 2207–2210, 2017.

[15] J. Kim, B. Clerckx, and P. D. Mitcheson, "Prototyping and experimentation of a closed-loop wireless power transmission with channel acquisition and waveform optimization," in *2017 IEEE Wireless Power Transfer Conference (WPTC)*.   IEEE, May 2017, pp. 1–4.

[16] B. Clerckx, "Wireless information and power transfer: Nonlinearity, waveform design, and rate-energy tradeoff," *IEEE Transactions on Signal Processing*, vol. 66, no. 4, pp. 847–862, Feb. 2018.

[17] M. Varasteh, B. Rassouli, and B. Clerckx, "On capacity-achieving distributions for complex AWGN channels under nonlinear power constraints and their applications to SWIPT," *IEEE Transactions on Information Theory*, vol. 66, no. 10, pp. 6488–6508, Oct. 2020.

[18] ——, "SWIPT signaling over frequency-selective channels with a nonlinear energy harvester: Non-zero mean and asymmetric inputs," *IEEE Transactions on Communications*, vol. 67, no. 10, pp. 7195–7210, Oct. 2019.

[19] M. Varasteh, J. Hoydis, and B. Clerckx, "Learning to communicate and energize: Modulation, coding, and multiple access designs for wireless information-power transmission," *IEEE Transactions on Communications*, vol. 68, no. 11, pp. 6822–6839, Nov. 2020.

[20] R. Anwar, L. Mao, and H. Ning, "Frequency selective surfaces: A review," *Applied Sciences*, vol. 8, no. 9, p. 1689, Sep. 2018.

[21] T. J. Cui, M. Q. Qi, X. Wan, J. Zhao, and Q. Cheng, "Coding metamaterials, digital metamaterials and programmable metamaterials," *Light: Science & Applications*, vol. 3, no. 10, pp. e218–e218, Oct. 2014.

[22] C. Liaskos, S. Nie, A. Tsioliaridou, A. Pitsillides, S. Ioannidis, and I. Akyildiz, "Realizing wireless communication through software-defined hypersurface environments," in *2018 IEEE 19th International Symposium on "A World of Wireless, Mobile and Multimedia Networks" (WoWMoM)*.   IEEE, Jun. 2018, pp. 14–15.

[23] Q. Wu and R. Zhang, "Intelligent reflecting surface enhanced wireless network: Joint active and passive beamforming design," vol. 18.   IEEE, Dec 2018, pp. 1–6.

[24] ——, "Beamforming optimization for intelligent reflecting surface with discrete phase shifts," in *ICASSP 2019 - 2019 IEEE International Conference on Acoustics, Speech and Signal Processing (ICASSP)*.   IEEE, May 2019, pp. 7830–7833.

[25] ——, "Intelligent reflecting surface enhanced wireless network via joint active and passive beamforming," *IEEE Transactions on Wireless Communications*, vol. 18, pp. 5394–5409, Nov 2019.

[26] S. Abeywickrama, R. Zhang, and C. Yuen, "Intelligent reflecting surface: Practical phase shift model and beamforming optimization," in *ICC 2020 - 2020 IEEE International Conference on Communications (ICC)*.   IEEE, Jun. 2020, pp. 1–6.

[27] Q.-U.-A. Nadeem, A. Kammoun, A. Chaaban, M. Debbah, and M.-S. Alouini, "Intelligent reflecting surface assisted wireless communication: Modeling and channel estimation," *arXiv:1906.02360*, pp. 1–7, Jun. 2019.

[28] C. You, B. Zheng, and R. Zhang, "Intelligent reflecting surface with discrete phase shifts: Channel estimation and passive beamforming."   IEEE, Jun 2020, pp. 1–6.

[29] J.-M. Kang, "Intelligent reflecting surface: Joint optimal training sequence and refection pattern," *IEEE Communications Letters*, vol. 24, no. 8, pp. 1784–1788, Aug. 2020.

[30] P. Wang, J. Fang, H. Duan, and H. Li, "Compressed channel estimation for intelligent reflecting surface-assisted millimeter wave systems," *IEEE Signal Processing Letters*, vol. 27, pp. 905–909, 2020.

[31] Q. Wu and R. Zhang, "Towards smart and reconfigurable environment: Intelligent reflecting surface aided wireless network," *IEEE Communications Magazine*, vol. 58, pp. 106–112, 1 2020.

[32] L. Dai, B. Wang, M. Wang, X. Yang, J. Tan, S. Bi, S. Xu, F. Yang, Z. Chen, M. D. Renzo, C.-B. Chae, and L. Hanzo, "Reconfigurable intelligent surface-based wireless communications: Antenna design, prototyping, and experimental results," *IEEE Access*, vol. 8, pp. 45 913–45 923, 2020.

[33] Q. Wu and R. Zhang, "Weighted sum power maximization for intelligent reflecting surface aided SWIPT," *IEEE Wireless Communications Letters*, vol. 9, no. 5, pp. 586–590, May 2020.

[34] Y. Tang, G. Ma, H. Xie, J. Xu, and X. Han, "Joint transmit and reflective beamforming design for IRS-assisted multiuser MISO SWIPT systems," in *ICC 2020 - 2020 IEEE International Conference on Communications (ICC)*.   IEEE, Jun. 2020, pp. 1–6.

[35] Q. Wu and R. Zhang, "Joint active and passive beamforming optimization for intelligent reflecting surface assisted SWIPT under QoS constraints," *IEEE Journal on Selected Areas in Communications*, vol. 38, no. 8, pp. 1735–1748, Aug. 2020.

[36] D. Xu, X. Yu, V. Jamali, D. W. K. Ng, and R. Schober, "Resource allocation for large IRS-assisted SWIPT systems with non-linear energy harvesting model," in *2021 IEEE Wireless Communications and Networking Conference (WCNC)*.   IEEE, Mar. 2021, pp. 1–7.

[37] R. Hansen, "Relationships between antennas as scatterers and as radiators," *Proceedings of the IEEE*, vol. 77, pp. 659–662, May 1989.

[38] G. H. Golub and C. F. Van Loan, *Matrix Computations*. Baltimore, MD, USA: Johns Hopkins University Press, 2013.

[39] T. Adali and S. Haykin, Eds., *Adaptive Signal Processing: Next Generation Solutions*. Hoboken, NJ, USA: Wiley, Mar. 2010.

[40] Z.-q. Luo, W.-k. Ma, A. So, Y. Ye, and S. Zhang, "Semidefinite relaxation of quadratic optimization problems," *IEEE Signal Processing Magazine*, vol. 27, no. 3, pp. 20–34, May 2010.

[41] M. Grant, S. Boyd, and Y. Ye, "CVX: MATLAB software for disciplined convex programming," 2016. [Online]. Available: http://cvxr.com/cvx

[42] S. Boyd, S.-J. Kim, L. Vandenberghe, and A. Hassibi, "A tutorial on geometric programming," *Optimization and Engineering*, vol. 8, no. 1, pp. 67–127, May 2007.

[43] M. Chiang, *Geometric Programming for Communication Systems*. Boston, MA: Now, 2005.

[44] D. Tse and P. Viswanath, *Fundamentals of Wireless Communication*. Cambridge University Press, May 2005.

[45] L. Grippo and M. Sciandrone, "On the convergence of the block nonlinear gauss–seidel method under convex constraints," *Operations Research Letters*, vol. 26, no. 3, pp. 127–136, Apr. 2000.

[46] V. Erceg, L. Schumacher, P. Kyritsi, A. Molisch, D. S. Baum, A. Y. Gorokhov, C. Oestges, Q. Li, K. Yu, N. Tal, B. Dijkstra, A. Jagannatham, C. Lanzl, V. J. Rhodes, J. Medbo, D. Michelson, M. Webster, E. Jacobsen, D. Cheung, C. Prettie, M. Ho, S. Howard, B. Bjerke, L. Jengx, H. Sampath, S. Catreux, S. Valle, A. Poloni, A. Forenza, and R. W. Heath, "IEEE P802.11 wireless LANs TGn channel models," *IEEE 802.11-03/940r4*, 2004.

[47] S. Li, K. Yang, M. Zhou, J. Wu, L. Song, Y. Li, and H. Li, "Full-duplex amplify-and-forward relaying: Power and location optimization," *IEEE Transactions on Vehicular Technology*, vol. 66, no. 9, pp. 8458–8468, Sep. 2017.

[48] O. Ozdogan, E. Bjornson, and E. G. Larsson, "Intelligent reflecting surfaces: Physics, propagation, and pathloss modeling," *IEEE Wireless Communications Letters*, vol. 9, no. 5, pp. 581–585, May 2020.

[49] W. Tang, M. Z. Chen, X. Chen, J. Y. Dai, Y. Han, M. Di Renzo, Y. Zeng, S. Jin, Q. Cheng, and T. J. Cui, "Wireless communications with reconfigurable intelligent surface: Path loss modeling and experimental measurement," *IEEE Transactions on Wireless Communications*, vol. 20, no. 1, pp. 421–439, Jan. 2021.

[50] Q. Wu and R. Zhang, "Beamforming optimization for wireless network aided by intelligent reflecting surface with discrete phase shifts," *IEEE Transactions on Communications*, vol. 68, no. 3, pp. 1838–1851, Mar. 2020.

[51] S. Shen, B. Clerckx, and R. Murch, "Modeling and architecture design of reconfigurable intelligent surfaces using scattering parameter network analysis," *IEEE Transactions on Wireless Communications*, pp. 1–1, Nov. 2021.

[52] C. Boyer and S. Roy, "Backscatter communication and RFID: Coding, energy, and MIMO analysis," *IEEE Transactions on Communications*, vol. 62, pp. 770–785, Mar 2014.

[53] D. Dobkin, *The RF in RFID: Passive UHF RFID in Practice*. Newnes, Nov 2012.

[54] J. Landt, "The history of RFID," *IEEE Potentials*, vol. 24, pp. 8–11, Oct 2005.

[55] G. Vannucci, A. Bletsas, and D. Leigh, "A software-defined radio system for backscatter sensor networks," *IEEE Transactions on Wireless Communications*, vol. 7, pp. 2170–2179, Jun 2008.

[56] S. D. Assimonis, S. N. Daskalakis, and A. Bletsas, "Sensitive and efficient RF harvesting supply for batteryless backscatter sensor networks," *IEEE Transactions on Microwave Theory and Techniques*, vol. 64, pp. 1327–1338, Apr 2016.

[57] V. Liu, A. Parks, V. Talla, S. Gollakota, D. Wetherall, and J. R. Smith, "Ambient backscatter: Wireless communication out of thin air," *ACM SIGCOMM Computer Communication Review*, vol. 43, pp. 39–50, Sep 2013.

[58] G. Yang, Q. Zhang, and Y.-C. Liang, "Cooperative ambient backscatter communications for green internet-of-things," *IEEE Internet of Things Journal*, vol. 5, pp. 1116–1130, Apr 2018.

[59] Y.-C. Liang, Q. Zhang, E. G. Larsson, and G. Y. Li, "Symbiotic radio: Cognitive backscattering communications for future wireless networks," *IEEE Transactions on Cognitive Communications and Networking*, vol. 6, pp. 1242–1255, Dec 2020.

[60] Q. Wu, S. Zhang, B. Zheng, C. You, and R. Zhang, "Intelligent reflecting surface-aided wireless communications: A tutorial," *IEEE Transactions on Communications*, vol. 69, pp. 3313–3351, May 2021.

[61] H. Guo, Y.-C. Liang, R. Long, and Q. Zhang, "Cooperative ambient backscatter system: A symbiotic radio paradigm for passive IoT," *IEEE Wireless Communications Letters*, vol. 8, pp. 1191–1194, Aug 2019.

[62] H. Ding, D. B. da Costa, and J. Ge, "Outage analysis for cooperative ambient backscatter systems," *IEEE Wireless Communications Letters*, vol. 9, pp. 601–605, May 2020.

[63] J. Qian, Y. Zhu, C. He, F. Gao, and S. Jin, "Achievable rate and capacity analysis for ambient backscatter communications," *IEEE Transactions on Communications*, vol. 67, pp. 6299–6310, Sep 2019.

[64] H. E. Hassani, A. Savard, E. V. Belmega, and R. C. de Lamare, "Multi-user downlink NOMA systems aided by ambient backscattering: Achievable rate regions and energy-efficiency maximization," *IEEE Transactions on Green Communications and Networking*, pp. 1–1, 2023.

[65] R. Torres, R. Correia, N. Carvalho, S. N. Daskalakis, G. Goussetis, Y. Ding, A. Georgiadis, A. Eid, J. Hester, and M. M. Tentzeris, "Backscatter communications," *IEEE Journal of Microwaves*, vol. 1, pp. 864–878, Oct 2021.

[66] R. Long, Y.-C. Liang, H. Guo, G. Yang, and R. Zhang, "Symbiotic radio: A new communication paradigm for passive internet of things," *IEEE Internet of Things Journal*, vol. 7, pp. 1350–1363, Feb 2020.

[67] S. Zhou, W. Xu, K. Wang, C. Pan, M.-S. Alouini, and A. Nallanathan, "Ergodic rate analysis of cooperative ambient backscatter communication," *IEEE Wireless Communications Letters*, vol. 8, pp. 1679–1682, Dec 2019.

[68] T. Wu, M. Jiang, Q. Zhang, Q. Li, and J. Qin, "Beamforming design in multiple-input-multiple-output symbiotic radio backscatter systems," *IEEE Communications Letters*, vol. 25, pp. 1949–1953, Jun 2021.

[69] J. Xu, Z. Dai, and Y. Zeng, "Enabling full mutualism for symbiotic radio with massive backscatter devices," *arXiv:2106.05789*, Jun 2021.

[70] Z. Yang and Y. Zhang, "Optimal SWIPT in RIS-aided MIMO networks," *IEEE Access*, vol. 9, pp. 112 552–112 560, 2021.

[71] S. Han, Y.-C. Liang, and G. Sun, "The design and optimization of random code assisted multi-BD symbiotic radio system," *IEEE Transactions on Wireless Communications*, vol. 20, pp. 5159–5170, Aug 2021.

[72] Q. Zhang, Y.-C. Liang, H.-C. Yang, and H. V. Poor, "Mutualistic mechanism in symbiotic radios: When can the primary and secondary transmissions be mutually beneficial?" *IEEE Transactions on Wireless Communications*, vol. 1276, pp. 1–1, 2022.

[73] Z. Dai, R. Li, J. Xu, Y. Zeng, and S. Jin, "Rate-region characterization and channel estimation for cell-free symbiotic radio communications," *IEEE Transactions on Communications*, vol. 71, pp. 674–687, Feb 2023.

[74] S. Zhang and R. Zhang, "Capacity characterization for intelligent reflecting surface aided MIMO communication," *IEEE Journal on Selected Areas in Communications*, vol. 38, pp. 1823–1838, Aug 2020.

[75] S. Lin, B. Zheng, F. Chen, and R. Zhang, "Intelligent reflecting surface-aided spectrum sensing for cognitive radio," *IEEE Wireless Communications Letters*, vol. 11, pp. 928–932, May 2022.

[76] Y. Liu, Y. Zhang, X. Zhao, S. Geng, P. Qin, and Z. Zhou, "Dynamic-controlled RIS assisted multi-user MISO downlink system: Joint beamforming design," *IEEE Transactions on Green Communications and Networking*, vol. 6, pp. 1069–1081, Jun 2022.

[77] Z. Feng, B. Clerckx, and Y. Zhao, "Waveform and beamforming design for intelligent reflecting surface aided wireless power transfer: Single-user and multi-user solutions," *IEEE Transactions on Wireless Communications*, 2022.

[78] Y. Zhao, B. Clerckx, and Z. Feng, "IRS-aided SWIPT: Joint waveform, active and passive beamforming design under nonlinear harvester model," *IEEE Transactions on Communications*, vol. 70, pp. 1345–1359, 2022.

[79] Y. Yang, S. Zhang, and R. Zhang, "IRS-enhanced OFDMA: Joint resource allocation and passive beamforming optimization," *IEEE Wireless Communications Letters*, vol. 9, pp. 760–764, Jun 2020.

[80] Q. Wu, X. Zhou, and R. Schober, "IRS-assisted wireless powered NOMA: Do we really need different phase shifts in DL and UL?" *IEEE Wireless Communications Letters*, vol. 10, pp. 1493–1497, Jul 2021.

[81] Q. Wu, X. Zhou, W. Chen, J. Li, and X. Zhang, "IRS-aided WPCNs: A new optimization framework for dynamic IRS beamforming," *IEEE Transactions on Wireless Communications*, pp. 1–1, Dec 2021.

[82] M. Hua and Q. Wu, "Joint dynamic passive beamforming and resource allocation for IRS-aided full-duplex WPCN," *IEEE Transactions on Wireless Communications*, pp. 1–1, Dec 2021.

[83] W. Tang, J. Y. Dai, M. Chen, X. Li, Q. Cheng, S. Jin, K.-K. Wong, and T. J. Cui, "Programmable metasurface-based RF chain-free 8PSK wireless transmitter," *Electronics Letters*, vol. 55, pp. 417–420, Apr 2019.

[84] J. Y. Dai, W. Tang, L. X. Yang, X. Li, M. Z. Chen, J. C. Ke, Q. Cheng, S. Jin, and T. J. Cui, "Realization of multi-modulation schemes for wireless communication by time-domain digital coding metasurface," *IEEE Transactions on Antennas and Propagation*, vol. 68, pp. 1618–1627, Mar 2020.

[85] R. Karasik, O. Simeone, M. D. Renzo, and S. S. Shitz, "Beyond max-SNR: Joint encoding for reconfigurable intelligent surfaces," vol. 2020-June. IEEE, Jun 2020, pp. 2965–2970.

[86] R. Liu, H. Li, M. Li, and Q. Liu, "Symbol-level precoding design for intelligent reflecting surface assisted multi-user MIMO systems." IEEE, Oct 2019, pp. 1–6.

[87] A. Bereyhi, V. Jamali, R. R. Muller, A. M. Tulino, G. Fischer, and R. Schober, "A single-RF architecture for multiuser massive MIMO via reflecting surfaces." IEEE, May 2020, pp. 8688–8692.

[88] X. Xu, Y.-C. Liang, G. Yang, and L. Zhao, "Reconfigurable intelligent surface empowered symbiotic radio over broadcasting signals." IEEE, Dec 2020, pp. 1–6.

[89] Q. Zhang, Y.-C. Liang, and H. V. Poor, "Reconfigurable intelligent surface assisted MIMO symbiotic radio networks," *IEEE Transactions on Communications*, vol. 69, pp. 4832–4846, Jul 2021.

[90] J. Hu, Y. C. Liang, and Y. Pei, "Reconfigurable intelligent surface enhanced multi-user MISO symbiotic radio system," *IEEE Transactions on Communications*, vol. 69, pp. 2359–2371, Apr 2021.

[91] M. Hua, Q. Wu, L. Yang, R. Schober, and H. V. Poor, "A novel wireless communication paradigm for intelligent reflecting surface based symbiotic radio systems," *IEEE Transactions on Signal Processing*, vol. 70, pp. 550–565, Apr 2022.

[92] E. Basar, "Reconfigurable intelligent surface-based index modulation: A new beyond MIMO paradigm for 6G," *IEEE Transactions on Communications*, vol. 68, pp. 3187–3196, May 2020.

[93] T. Ma, Y. Xiao, X. Lei, P. Yang, X. Lei, and O. A. Dobre, "Large intelligent surface assisted wireless communications with spatial modulation and antenna selection," *IEEE Journal on Selected Areas in Communications*, vol. 38, pp. 2562–2574, Nov 2020.

[94] J. Yuan, M. Wen, Q. Li, E. Basar, G. C. Alexandropoulos, and G. Chen, "Receive quadrature reflecting modulation for RIS-empowered wireless communications," *IEEE Transactions on Vehicular Technology*, vol. 70, pp. 5121–5125, May 2021.

[95] S. Hu, C. Liu, Z. Wei, Y. Cai, D. W. K. Ng, and J. Yuan, "Beamforming design for intelligent reflecting surface-enhanced symbiotic radio systems." IEEE, 5 2022, pp. 2651–2657.

[96] I. Vardakis, G. Kotridis, S. Peppas, K. Skyvalakis, G. Vougioukas, and A. Bletsas, "Intelligently wireless batteryless RF-powered reconfigurable surface: Theory, implementation & limitations," *IEEE Transactions on Wireless Communications*, vol. 22, pp. 3942–3954, Jun 2023.

[97] Y. C. Liang, Q. Zhang, J. Wang, R. Long, H. Zhou, and G. Yang, "Backscatter communication assisted by reconfigurable intelligent surfaces," *Proceedings of the IEEE*, 2022.

[98] S. J. Thomas and M. S. Reynolds, "A 96 mbit/sec, 15.5 pj/bit 16-qam modulator for uhf backscatter communication." IEEE, Apr 2012, pp. 185–190.

[99] N. V. Huynh, D. T. Hoang, X. Lu, D. Niyato, P. Wang, and D. I. Kim, "Ambient backscatter communications: A contemporary survey," *IEEE Communications Surveys & Tutorials*, vol. 20, pp. 2889–2922, 2018.

[100] S. J. Thomas, E. Wheeler, J. Teizer, and M. S. Reynolds, "Quadrature amplitude modulated backscatter in passive and semipassive UHF RFID systems," *IEEE Transactions on Microwave Theory and Techniques*, vol. 60, pp. 1175–1182, Apr 2012.

[101] J. Kim and B. Clerckx, "Wireless information and power transfer for IoT: Pulse position modulation, integrated receiver, and experimental validation," *IEEE Internet of Things Journal*, vol. 9, pp. 12 378–12 394, Jul 2022.

[102] X. He, W. Jiang, M. Cheng, X. Zhou, P. Yang, and B. Kurkoski, "GuardRider: Reliable WiFi backscatter using reed-solomon codes with QoS guarantee." IEEE, Jun 2020, pp. 1–10.

[103] D. Bharadia, K. R. Joshi, M. Kotaru, and S. Katti, "BackFi: High throughput WiFi backscatter," vol. 45. ACM, Aug 2015, pp. 283–296.

[104] G. Yang, C. K. Ho, and Y. L. Guan, "Multi-antenna wireless energy transfer for backscatter communication systems," *IEEE Journal on Selected Areas in Communications*, vol. 33, pp. 2974–2987, Dec 2015.

[105] H. Guo, Q. Zhang, S. Xiao, and Y.-C. Liang, "Exploiting multiple antennas for cognitive ambient backscatter communication," *IEEE Internet of Things Journal*, vol. 6, pp. 765–775, Feb 2019.

[106] M. Jin, Y. He, C. Jiang, and Y. Liu, "Parallel backscatter: Channel estimation and beyond," *IEEE/ACM Transactions on Networking*, vol. 29, pp. 1128–1140, Jun 2021.

[107] B. Zheng and R. Zhang, "Intelligent reflecting surface-enhanced OFDM: Channel estimation and reflection optimization," *IEEE Wireless Communications Letters*, vol. 9, pp. 518–522, Apr 2020.

[108] J. Qian, A. N. Parks, J. R. Smith, F. Gao, and S. Jin, "IoT communications with M-PSK modulated ambient backscatter: Algorithm, analysis, and implementation," *IEEE Internet of Things Journal*, vol. 6, pp. 844–855, Feb 2019.

[109] W. Wu, X. Wang, A. Hawbani, L. Yuan, and W. Gong, "A survey on ambient backscatter communications: Principles, systems, applications, and challenges," Oct 2022.

[110] T. Nguyen, Y.-J. Chu, and T. Nguyen, "On the capacities of discrete memoryless thresholding channels," vol. 2018-June. IEEE, Jun 2018, pp. 1–5.

[111] T. Nguyen and T. Nguyen, "Optimal quantizer structure for maximizing mutual information under constraints," *IEEE Transactions on Communications*, vol. 69, pp. 7406–7413, Nov 2021.

[112] M. Rezaeian and A. Grant, "Computation of total capacity for discrete memoryless multiple-access channels," *IEEE Transactions on Information Theory*, vol. 50, pp. 2779–2784, Nov 2004.

[113] G. J. O. Jameson, "The incomplete gamma functions," *The Mathematical Gazette*, vol. 100, pp. 298–306, Jul 2016.

[114] S. Boyd and L. Vandenberghe, *Convex Optimization*. Cambridge University Press, Mar 2004.

[115] X. He, K. Cai, W. Song, and Z. Mei, "Dynamic programming for sequential deterministic quantization of discrete memoryless channels," *IEEE Transactions on Communications*, vol. 69, pp. 3638–3651, Jun 2021.

[116] T. Nguyen and T. Nguyen, "On thresholding quantizer design for mutual information maximization: Optimal structures and algorithms," vol. 2020-May. IEEE, May 2020, pp. 1–5.

[117] B. W. Bader and T. G. Kolda, "Tensor toolbox for MATLAB," https://www.tensortoolbox.org/, Sep 2022.

[118] E. Calvo, D. P. Palomar, J. R. Fonollosa, and J. Vidal, "On the computation of the capacity region of the discrete MAC," *IEEE Transactions on Communications*, vol. 58, pp. 3512–3525, Dec 2010.

[119] W. Liu, S. Shen, D. H. K. Tsang, R. K. Mallik, and R. Murch, "An efficient ratio detector for ambient backscatter communication," *arXiv:2210.09920*, Oct 2022.

[120] E. Basar, M. D. Renzo, J. D. Rosny, M. Debbah, M.-S. Alouini, and R. Zhang, "Wireless communications through reconfigurable intelligent surfaces," *IEEE Access*, vol. 7, pp. 116 753–116 773, 2019. [Online]. Available: https://ieeexplore.ieee.org/document/8796365/

[121] B. Zheng, C. You, and R. Zhang, "Double-irs assisted multi-user mimo: Cooperative passive beamforming design," *IEEE Transactions on Wireless Communications*, vol. 20, pp. 4513–4526, 7 2021. [Online]. Available: https://ieeexplore.ieee.org/document/9362274/

[122] X. Jia, J. Zhao, X. Zhou, and D. Niyato, "Intelligent reflecting surface-aided backscatter communications," vol. 2020-Janua.   IEEE, 12 2020, pp. 1–6. [Online]. Available: https://ieeexplore.ieee.org/document/9348003/

[123] R. Liu, M. Li, Y. Liu, Q. Wu, and Q. Liu, "Joint transmit waveform and passive beamforming design for ris-aided dfrc systems," *IEEE Journal of Selected Topics in Signal Processing*, pp. 1–1, 5 2022.

[124] M. Hua, Q. Wu, C. He, S. Ma, and W. Chen, "Joint active and passive beamforming design for irs-aided radar-communication," *IEEE Transactions on Wireless Communications*, vol. 22, pp. 2278–2294, 4 2023.

[125] Y. Zhao and B. Clerckx, "Riscatter: Unifying backscatter communication and reconfigurable intelligent surface," 12 2022. [Online]. Available: http://arxiv.org/abs/2212.09121

[126] H. Li, S. Shen, and B. Clerckx, "Beyond diagonal reconfigurable intelligent surfaces: From transmitting and reflecting modes to single-, group-, and fully-connected architectures," *IEEE Transactions on Wireless Communications*, vol. 22, pp. 2311–2324, 4 2023.

[127] M. Nerini, S. Shen, and B. Clerckx, "Closed-form global optimization of beyond diagonal reconfigurable intelligent surfaces," *IEEE Transactions on Wireless Communications*, pp. 1–1, 2023. [Online]. Available: https://ieeexplore.ieee.org/document/10155675/

[128] I. Santamaria, M. Soleymani, E. Jorswieck, and J. Gutiérrez, "Snr maximization in beyond diagonal ris-assisted single and multiple antenna links," *IEEE Signal Processing Letters*, vol. 30, pp. 923–926, 2023. [Online]. Available: https://ieeexplore.ieee.org/document/10187688/

[129] T. Fang and Y. Mao, "A low-complexity beamforming design for beyond-diagonal ris aided multi-user networks," *IEEE Communications Letters*, pp. 1–1, 7 2023. [Online]. Available: https://ieeexplore.ieee.org/document/10319662/

[130] M. Nerini, S. Shen, H. Li, and B. Clerckx, "Beyond diagonal reconfigurable intelligent surfaces utilizing graph theory: Modeling, architecture design, and optimization," 5 2023. [Online]. Available: http://arxiv.org/abs/2305.05013

[131] Y. Zhou, Y. Liu, H. Li, Q. Wu, S. Shen, and B. Clerckx, "Optimizing power consumption, energy efficiency and sum-rate using beyond diagonal ris — a unified approach," *IEEE Transactions on Wireless Communications*, pp. 1–1, 2023. [Online]. Available: https://ieeexplore.ieee.org/document/10364738/

[132] H. Li, S. Shen, and B. Clerckx, "A dynamic grouping strategy for beyond diagonal reconfigurable intelligent surfaces with hybrid transmitting and reflecting mode," *IEEE Transactions on Vehicular Technology*, 12 2023.

[133] G. Bartoli, A. Abrardo, N. Decarli, D. Dardari, and M. D. Renzo, "Spatial multiplexing in near field mimo channels with reconfigurable intelligent surfaces," *IET Signal Processing*, vol. 17, 3 2023. [Online]. Available: https://ietresearch.onlinelibrary.wiley.com/doi/10.1049/sil2.12195

[134] H. Li, S. Shen, and B. Clerckx, "Beyond diagonal reconfigurable intelligent surfaces: A multi-sector mode enabling highly directional full-space wireless coverage," *IEEE Journal on Selected Areas in Communications*, vol. 41, pp. 2446–2460, 8 2023.

[135] H. Li, Y. Zhang, and B. Clerckx, "Channel estimation for beyond diagonal reconfigurable intelligent surfaces with group-connected architectures," 7 2023. [Online]. Available: http://arxiv.org/abs/2307.06129

[136] H. Li, S. Shen, M. Nerini, M. D. Renzo, and B. Clerckx, "Beyond diagonal reconfigurable intelligent surfaces with mutual coupling: Modeling and optimization," 10 2023. [Online]. Available: http://arxiv.org/abs/2310.02708

[137] H. Li, S. Shen, M. Nerini, and B. Clerckx, "Reconfigurable intelligent surfaces 2.0: Beyond diagonal phase shift matrices," 1 2023. [Online]. Available: http://arxiv.org/abs/2301.03288

[138] B. Ning, Z. Chen, W. Chen, and J. Fang, "Beamforming optimization for intelligent reflecting surface assisted mimo: A sum-path-gain maximization approach," *IEEE Wireless Communications Letters*, vol. 9, pp. 1105–1109, 7 2020.

[139] O. Ozdogan, E. Bjornson, and E. G. Larsson, "Using intelligent reflecting surfaces for rank improvement in mimo communications." IEEE, 5 2020, pp. 9160–9164. [Online]. Available: https://ieeexplore.ieee.org/document/9052904/

[140] G.-H. Li, D.-W. Yue, and S.-N. Jin, "Spatially correlated rayleigh fading characteristics of ris-aided mmwave mimo communications," *IEEE Communications Letters*, vol. 27, pp. 2222–2226, 8 2023. [Online]. Available: https://ieeexplore.ieee.org/document/10164200/

[141] Y. Zheng, T. Lin, and Y. Zhu, "Passive beamforming for irs-assisted mu-mimo systems with one-bit adcs: An ser minimization design approach," *IEEE Communications Letters*, vol. 26, pp. 1101–1105, 5 2022. [Online]. Available: https://ieeexplore.ieee.org/document/9706177/

[142] W. Huang, B. Lei, S. He, C. Kai, and C. Li, "Condition number improvement of irs-aided near-field mimo channels." IEEE, 5 2023, pp. 1210–1215. [Online]. Available: https://ieeexplore.ieee.org/document/10283534/

[143] M. A. ElMossallamy, H. Zhang, R. Sultan, K. G. Seddik, L. Song, G. Y. Li, and Z. Han, "On spatial multiplexing using reconfigurable intelligent surfaces," *IEEE Wireless Communications Letters*, vol. 10, pp. 226–230, 2 2021. [Online]. Available: https://ieeexplore.ieee.org/document/9200661/

[144] S. Meng, W. Tang, W. Chen, J. Lan, Q. Y. Zhou, Y. Han, X. Li, and S. Jin, "Rank optimization for mimo channel with ris: Simulation and measurement," 7 2023. [Online]. Available: http://arxiv.org/abs/2307.13237

[145] T. E. Abrudan, J. Eriksson, and V. Koivunen, "Steepest descent algorithms for optimization under unitary matrix constraint," *IEEE Transactions on Signal Processing*, vol. 56, pp. 1134–1147, 3 2008. [Online]. Available: http://ieeexplore.ieee.org/document/4436033/

[146] T. Abrudan, J. Eriksson, and V. Koivunen, "Conjugate gradient algorithm for optimization under unitary matrix constraint," *Signal Processing*, vol. 89, pp. 1704–1714, 9 2009. [Online]. Available: https://linkinghub.elsevier.com/retrieve/pii/S0165168409000814

[147] A. Edelman, T. A. Arias, and S. T. Smith, "The geometry of algorithms with orthogonality constraints," *SIAM Journal on Matrix Analysis and Applications*, vol. 20, pp. 303–353, 1 1998. [Online]. Available: http://epubs.siam.org/doi/10.1137/S0895479895290954

[148] P.-A. Absil, R. Mahony, and R. Sepulchre, *Optimization Algorithms on Matrix Manifolds*. Princeton University Press, 2009. [Online]. Available: https://books.google.co.uk/books?id=NSQGQeLN3NcC

[149] C. Pan, G. Zhou, K. Zhi, S. Hong, T. Wu, Y. Pan, H. Ren, M. D. Renzo, A. L. Swindlehurst, R. Zhang, and A. Y. Zhang, "An overview of signal processing techniques for ris/irs-aided wireless systems," *IEEE Journal of Selected Topics in Signal Processing*, vol. 16, pp. 883–917, 8 2022. [Online]. Available: https://ieeexplore.ieee.org/document/9847080/

[150] M. T. Ivrlac and J. A. Nossek, "Toward a circuit theory of communication," *IEEE Transactions on Circuits and Systems I: Regular Papers*, vol. 57, pp. 1663–1683, 7 2010. [Online]. Available: https://ieeexplore.ieee.org/document/5446312/

[151] H.-R. Ahn, *Asymmetric Passive Components in Microwave Integrated Circuits*. Wiley, 2006. [Online]. Available: https://books.google.co.uk/books?id=X6WdLbOuSNQC

[152] E. Polak and G. Ribiere, "Note sur la convergence de méthodes de directions conjuguées," *Revue française d'informatique et de recherche opérationnelle. Série rouge*, vol. 3, pp. 35–43, 1969.

[153] L. Armijo, "Minimization of functions having lipschitz continuous first partial derivatives," *Pacific Journal of Mathematics*, vol. 16, pp. 1–3, 1 1966. [Online]. Available: http://msp.org/pjm/1966/16-1/p01.xhtml

[154] D. Semmler, M. Joham, and W. Utschick, "High snr analysis of ris-aided mimo broadcast channels," in *2023 IEEE 24th International Workshop on Signal Processing Advances in Wireless Communications (SPAWC)*. IEEE, 9 2023, pp. 221–225. [Online]. Available: https://ieeexplore.ieee.org/document/10304487/

[155] W. Fulton, "Eigenvalues, invariant factors, highest weights, and schubert calculus," *Bulletin of the American Mathematical Society*, vol. 37, pp. 209–249, 4 2000. [Online]. Available: https://www.ams.org/bull/2000-37-03/S0273-0979-00-00865-X/

[156] B. Clerckx and C. Oestges, *MIMO Wireless Networks: Channels, Techniques and Standards for Multi-Antenna, Multi-User and Multi-Cell Systems*. Elsevier Science, 2013. [Online]. Available: https://books.google.co.uk/books?id=drEX1J7jHUIC

[157] J. C. Gower and G. B. Dijksterhuis, *Procrustes Problems*. OUP Oxford, 2004. [Online]. Available: https://books.google.co.uk/books?id=kRRREAAAQBAJ

[158] T. Bell, "Global positioning system-based attitude determination and the orthogonal procrustes problem," *Journal of Guidance, Control, and Dynamics*, vol. 26, pp. 820–822, 9 2003. [Online]. Available: https://arc.aiaa.org/doi/10.2514/2.5117

[159] F. Nie, R. Zhang, and X. Li, "A generalized power iteration method for solving quadratic problem on the stiefel manifold," *Science China Information Sciences*, vol. 60, p. 112101, 11 2017. [Online]. Available: http://link.springer.com/10.1007/s11432-016-9021-9

[160] D. Xu, X. Yu, Y. Sun, D. W. K. Ng, and R. Schober, "Resource allocation for IRS-assisted full-duplex cognitive radio systems," *IEEE Transactions on Communications*, vol. 68, no. 12, pp. 7376–7394, Dec. 2020.

[161] B. R. Marks and G. P. Wright, "A general inner approximation algorithm for nonconvex mathematical programs," *Operations Research*, vol. 26, no. 4, pp. 681–683, Aug. 1978.

[162] W.-C. Li, T.-H. Chang, C. Lin, and C.-Y. Chi, "Coordinated beamforming for multiuser MISO interference channel under rate outage constraints," *IEEE Transactions on Signal Processing*, vol. 61, no. 5, pp. 1087–1103, Mar. 2013.

[163] A. Hjorungnes and D. Gesbert, "Complex-valued matrix differentiation: Techniques and key results," *IEEE Transactions on Signal Processing*, vol. 55, pp. 2740–2746, 6 2007. [Online]. Available: http://ieeexplore.ieee.org/document/4203075/